TÉCNICO LISBOA

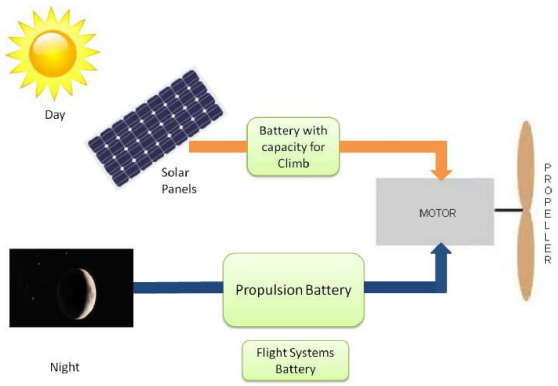

Design, Construction and Test of the Propulsion System of a Solar UAV

Héctor Manuel González Vidales

Thesis to obtain the Master of Science Degree in

Aerospace Engineering

Examination Committee

Chairperson:	Professor Fernando José Parracho Lau
Supervisor:	Doctor André Calado Marta
Members of the Committee:	Professor Pedro da Graça Tavares Alvares Serrão

March 2013

To Baltasar and Evangelina, my parents.

Acknowledgments

This master thesis is the result of the six months I spent as an Erasmus student in the UTL (Universidade Técnica de Lisboa) at IST (Instituto Superior Técnico) which is the largest and most reputed school of Engineering, Science and Technology and Architecture in Portugal. This period was very interesting and rewarding, and it was a pleasure to study in such environment.

I would like to thank my supervisor, Doctor André Calado Marta for his technical guidance and the opportunity to write this thesis. Throughout my work, he supported me and advised me how to approach the contents. Without him, this thesis would not have been possible.

To my parents, for their support and for giving me the opportunity to pursue higher education studies at university.

To my sisters Cristina and Ana, who always made themselves available and were genuinely most helpful since my first year at university.

To Bernardo, for his sayings to motivate me and his interest in learning, I hope you read this work too.

Finally, to Sara for her patience in all this time, her support in every moment and especially for her love.

Resumo

Os problemas de poluição e a necessidade de conseguir uma menor dependência do petróleo conduziram a que as tecnologias solar e eléctrica passassem a ter um papel importante nos sistemas de propulsão, uma tecnologia amplamente já conhecida na indústria automóvel, e mais recentemente usada na indústria aeronáutica. Esta tese contém o desenho conceptual de um sistema de propulsão híbrida de um veículo aéreo não tripulado (UAV). A instalação de propulsão solar é destinada a um UAV pequeno, com uma envergadura de 4,5 metros e um peso aproximado de 5 kg, com uma missão de vigilância civil específica. A sua arquitectura é totalmente diferente dos métodos convencionais de propulsão. As diferentes eficiências dos componentes influenciam na geração de energia, sendo o factor mais importante a irradiação solar e a capacidade de que os painéis solares têm de converter a energia, isto é, a sua eficiência. O projecto e dimensionamento dos diversos componentes do sistema de propulsão depende da energia disponível armazenada na bateria e da potência gerada pelos painéis solares. Devido a diferentes níveis de radiação solar ao longo do ano, são estudadas diferentes combinações de baterias, painéis solares e sistemas híbridos. O sistema de propulsão foi elaborado de acordo com os requisitos de energia disponível e energia requerida, e depois de um projecto apropriado, os diferentes componentes do sistema de propulsão são seleccionados de acordo com os critérios da missão. Finalmente, foi definido um programa de testes para realizar os ensaios necessários para verificar o bom funcionamento do sistema projectado.

Palavras-chave: Aviação verde, Voo eléctrico, Painéis solares , Irradiação solar, Propulsão híbrida.

Abstract

Pollution problems and the need to achieve a lower oil dependency have given solar and electric technologies, an important role in propulsion systems, from automotive to, more recently, aviation industry. This thesis contains the conceptual design of a hybrid propulsion system of an unmanned aerial vehicle (UAV). The solar-powered plant aimed at a small UAV with a wingspan of 4.5 m and an approximate weight of 5 kg, with a specific civil surveillance mission. Its architecture is completely different from the conventional methods of propulsion. From all the different efficiencies of the components that influence the use of energy, the most important factor is the solar irradiance and the ability that the solar panels have to harvest that energy, that is, their efficiency. The design and sizing of the different components of the propulsion system depends on the available energy stored in the battery or the generate power in the solar panels. As solar radiation is different throughout the year, different combinations of batteries, solar panels or hybrid systems are studied. The propulsion system is designed according to the requirements of energy available and energy required, and after appropriate design, the different components of the propulsion system are selected following design criteria. In the end, a road-map to achieve the necessary tests and check the proper functioning of the designed system will be established.

Keywords: Green aviation, Electric flight, Solar panels, Solar irradiance, Hybrid propulsion.

Contents

List of Tables

List of Figures

Nomenclature

Greek symbols

η_B	Battery efficiency.
η_C	Cables efficiency.
η_{ESC}	Electronic speed controller efficiency.
η_E	Electric motor efficiency.
η_{PV}	Photovoltaic cell efficiency.
η_P	Propeller efficiency.
η_T	Total efficiency.
ω	Rotational speed.
ρ	Density.

Roman symbols

b	Wingspan.
b_{PV}	Available wingspan for solar panels.
c	Wing mean chord.
C_{Di}	Induced drag coefficient.
C_{Dp}	Parasite drag coefficient.
C_D	Drag coefficient.
C_{Lmax}	Maximum lift coefficient.
C_L	Lift coefficient.
c_{PV}	Available wing mean chord for solar panels.
CF_W	Wingspan correction factor.
CF_{LE}	Leading edge correction factor .

CF_{TE} Trailing edge correction factor .

D Drag.

d Diameter.

E Energy.

E_p Gravitational potential energy.

E_{req} Required energy.

g Gravitational acceleration constant.

h Altitude.

I Current.

I_{day} Daily irradiance.

I_{mpp} Maximum power current.

I_{SC} Short circuit current.

J Propeller advance ratio.

L Lift.

m Mass.

M_P Propeller resistance moment.

n Number of blades.

P Power.

p Pitch.

P_{req} Required power.

S_{PV} Available wing area for solar panels.

S_{ref} Wing reference area.

T Thrust.

t Time.

T_{day} Daily irradiation time.

V Voltage.

v Flight speed.

V^* Specific volume.

V_{mpp} Maximum power voltage.

V_{OC} Open circuit voltage.

W Weight.

Subscripts

bat Battery.

cli Climb.

cru Cruise.

max Maximum.

PV Available condition (photo-voltaic cells).

ref Reference condition.

req Required condition.

$stage$ Segment of the mission.

$toff$ Take off.

Superscripts

* Reference to specific condition.

Glossary

AM0	Air Mass 0
BET	Blade Element Theory
BLDC	Brushless Direct Current
DC	Direct Current
ESC	Electronic Speed Controller
EVA	Ethyl Vinyl Acetate
HALE	High Altitude Long Endurance
HALSOL	High Altitude Solar
PV	Photo-Voltaic
SCC	Solar Charger Controller
SC	Solar Cell
SMARTS	Simple Model of the Atmospheric Radiative Transfer of Sunshine
STC	Standard Test Conditions
UAS	Unmanned Aircraft System
UAV	Unmanned Aerial Vehicle
UCAV	Unmanned Combat Aerial Vehicles
VTOL	Vertical Take Off and Landing

Chapter 1

Introduction

1.1 About the Project

The title of the thesis ”Design, Construction and Test of The Solar Propulsion System of a UAV”, unmanned aerial vehicle, is fairly representative and the impression created at first glance makes the contents clear. Knowing in detail the technology of a solar propulsion system like this is important but so is knowing other key factors related to the project that greatly justify this development.

The main content of the thesis is about the design of the propulsion system, namely for a solar UAV. Solar energy is very important in many sectors because it is a clean energy obtained from the use of electromagnetic radiation from the sun. In the aviation world, this type of energy is the key in some factors, polluting emissions, noise, and reduction of dependence oil as a source of non renewable energy. Uniting these factors, the search for new technologies and forms of propulsion opens a path to include the study of solar power as a energy source in the aircraft.

The ability for an aircraft to fly during a much extended period of time has become a key issue and a target of research, both in the domain of civilian aviation and unmanned aerial vehicles. The latter domain takes an increasingly important place in our society, for civilian and military applications. The required endurance is in the range of a couple of hours in the case of law enforcement, border surveillance, forest fire fighting or power line inspection. However, other applications at high altitudes, such as communication platform for mobile devices, weather research and forecast, environmental monitoring, would require remaining airborne during days, weeks or even months.

For the moment, it is only possible to reach such ambitious objectives using electric solar powered platforms. Photovoltaic modules may be used to collect the energy of the sun during the day, one part being used directly to power the propulsion unit and onboard instruments, the other part being stored for the night time.

In order to reach the target endurance, the design of the airplane has to be thought carefully and globally, as a system composed of many subsystems that are continuously exchanging energy. Due to these relationships, each part has to be sized accordingly to all the others. A crucial part lies in the combination of all the elements, and not only in their quality. This is especially true for multidisciplinary

projects, the case of a solar airplane being an ideal example as it requires knowledge in the fields of aerodynamics, structures, controls, electronics, energy storage, photovoltaic arrays, etc.

1.2 Unmanned Air Vehicles

Unmanned Aerial Vehicles, UAV in short, are defined as engine powered vehicles that can take off, fly and land with no onboard crew. They can either fly remotely (a ground pilot controls the UAV directly using some kind of remote control) as well as autonomously (a flight path is introduced into the UAV and it just follows it).They are usually called UAS –Unmanned Aircraft System, because the system does not only involve a lonely aircraft but ground systems. UAS can carry multiple payloads: cameras, sensors, communications equipment and others. They were first used in military tasks, such as for terrain reconnaissance or to attack all kinds of targets (these were called UCAVs, Unmanned Combat Aerial Vehicles). For example, the first known proposal of an UCAV, although it had never been widely used, was an aerostatic globe which had a mechanism that dropped an explosive load after a time-delayed fuse was burnt. That was in the late 1800s. From then, UCAVs were enhanced, being used as drones for training World War II pilots. During the Cold War they were extensively used for reconnaissance duties. Many different crafts, including Vertical Take Off and Landing ,VTOL, prototypes, were invented, tested and some of them were put in action.

Nowadays, UCAVs are extensively used by armies. Few countries are developing their own autonomous crafts, being the United States, the United Kingdom, Israel and Pakistan at the forefront.

Even though all these are set within military background, several models for multiple civil purposes have been developed until today, such as reconnaissance, mapping, weather and pollution sensing, environment supervision, search and rescue aiding, firefighting and mail delivering.

Solar UAV

The philosophy of a solar UAV is to propel the aircraft through solar energy autonomously and according to the type of mission. This breaks the traditional mode of propulsion by combustion chemistry and makes these aircraft have a structure and a propulsion system quite different from a conventional UAV.

The propulsion begins in the photovoltaic cells that convert solar energy into electricity, which are connected to the electric motor by different sophisticated systems governing the energy requirements. The last link in the chain is the propeller, typical in solar aircraft, which is responsible for providing the thrust of the aircraft. Batteries are another fundamental component and provide the autonomy of the plane, in this case limited for night flights. The structure and design of the aircraft wings and fuselage will be sufficient to place photovoltaic cells, in addition to supporting the plane loads.

Considering the solar radiation profiles in response to the needs that are required, there are two main advantages of a solar propulsion system: low noise level and extended operation time.

1.3 Objectives of the Project

The objectives of the project are very specific. The starting point is select the type of mission and the energy requirements needed to determine the specifications of a particular aircraft. Once the mission is selected it follows the design propulsion system with all the details to achieve the specifications that the mission requires. So the main goal is to design the propulsion system for an aircraft of a particular mission. The tasks in the design of the propulsion system of a solar powered UAV include:

1. Definition of the architecture of the propulsion system;
2. Sizing photovoltaic cells and solar arrays;
3. Sizing batteries;

   In both cases, the specifications, efficiency and other factors important for maximizing the efficiency of the propulsion system will be determined;
4. Analytic study of propulsion. To check with what propulsion method, batteries, solar panels or a hybrid of both, is possible to achieve the mission and in what conditions;
5. Preliminary selection of the suitable propulsion system components to achieve the required conditions;
6. Detailing a road-map for experimental test of the prototype selected.

1.4 Structure of the Document

This document contains three distinct parts, where the first is the base of the other two. This is a detailed study of a propulsion system for a UAV solar, comprising chapters 1 to 6 with great theoretical content. Chapters 1, 2 and 4 are purely descriptive, with the introduction, history and propulsion system configurations respectively. Chapter 3 is the starting point, is specified the mission of the aircraft and the necessary energy requirements. The analytical part begins in chapter 5 , which contains the phenomena of solar radiation for the optimization of solar arrays and a night flight plan. Chapter 6 is the last of this block and it contains all information about the solar technology and about the architecture of the propulsion system. The architecture section contains all components of the propulsion system from the solar cells to the propeller through all intermediate elements.

Chapter 7 is a comprehensive study of the most appropriate method of propulsion considering solar radiation and energy storage. This chapter will check that only with hybrid propulsion system, consisting of a battery and solar panels, is the mission accomplished.

Chapter 8 contains the preliminary selection of the hybrid propulsion system components.

Chapter 9 contains a small procedure or road-map about the experimental test of the propulsion system and subsystems, where it will be checked the correct operation of the prototype. This chapter lists some examples of experimental test and assembly schemes necessary to carry out the tests.

Finally, the conclusions will be exposed in Chapter 10 as well as some considerations about future work.

Chapter 2

Solar Energy in Aeronautics

Solar energy is a renewable energy that comes from natural resources so it is practically inexhaustible. Solar energy is derived from the Sun through the form of solar radiation which can be transformed into electricity or heat by using two kinds of solar cells: photovoltaic and photothermal, respectively as illustrated in Fig. 2.1(a) and Fig. 2.1(b).

The technological level required for use in an aircraft with a small wing area and moderate speeds are in continuous development because the efficiency of solar energy installations is generally very low, around 20%, and it may increases up to 30% only by high-level technologies. Therefore, wing surface covered by solar cells must be unusually large.

Two distinct usage of solar energy are identified: uptake and storage. Because of Earth motion, the harvesting is only possible during the day. Therefore a set of batteries, which stores part of captured energy, is necessary to let the systems be continuous. Furthermore, the capture of solar energy is not uniform neither in different regions of the Earth nor at different times of the year. Obviously, areas at higher latitude receive less perpendicular radiation so they get less energy. As a consequence, systems must be designed depending on the area of the Earth where they are to be applied. The time of day also influences the capture because the radiation's incidence depends on Sun elevation over the horizon. This problem is solved using solar panels which are capable of tracing the Sun and correct their orientation automatically.

As said before, the element used to obtain electrical energy are called solar photovoltaic cells. These cells are generally made of a semiconductor material, usually silicon, which releases electrons after receiving the radiation from the sun. Electrons can move through the material creating a potential difference in it. As a consequence, cells behave like a small unlimited battery when a load between the terminals is applied.

Energy obtained with a photovoltaic cell is very small, so it is necessary to combine a large number of PV cells to obtain good solar panels. However, the manufacture is complicated and expensive. Moreover, due to their low efficiency, they often need a power output control system and devices which can orient panels to increase the performances.

However, autonomy could be almost unlimited if a correct design of the aircraft, including certain

(a) Photovoltaic cell.

(b) Photothermal cell.

Figure 2.1: Type of solar cells [DR, 2013].

automated systems for flight, are made. Though without taking into account pilot's needs, the aircraft will not fly infinitively because it must descend for safety reasons when its life has completed. This lifetime will be substantially greater than conventional aircraft's operating time under the same conditions, so that we can say that the autonomy of the solar plane is unlimited.

2.1 History of Electric Propulsion

Electric flight is no new technology. Due to the sensitivity of aircraft to its mass, it was not really feasible for many years. Here only one of the many ancestral lines of electric flight shall be mentioned because it shows a remarkably long development path. Already in 1940, Fred Militky toyed with electric motors to propel model aircraft but, due to heavy brushed motors and lead batteries, he was unsuccessful to obtain good results [Hepperle, 2012]. Nevertheless, he followed his idea until he was finally able to introduce a small model airplane into the hobby market in 1960, the Silentius, as shown in Fig.2.2. This free flight model used a highly efficient electric motor and small lead batteries. Later in 1972, when Ni-Cd batteries with higher power densities became available he developed the first radio-controlled model which was commercially produced, the Hi-Fly, also shown in Fig.2.2. Finally, using the same Ni-Cd batteries, he helped to prepare the first electric flight of a manned aircraft. This aircraft was the modified motor-glider MB-E1 shown in Fig.2.2, which was finally flown in October 1973 by pilot H. Brditschka in Austria [Hepperle, 2012]. The technology available in these years allowed only for short flights of up to 15 minutes, but nevertheless, showed the feasibility of electric propulsion for man carrying aircraft. Lack of better battery systems prevented further development. It should be noted that, in contrast to some pioneering ultra-light experimental demonstrator aircraft, the MB-E1 was a variant of the fully certified airframe HB-3 with minor modifications to carry batteries and electric motor [Hepperle, 2012].

Nowadays, the situation is very different. The new technologies in batteries and solar panels are such that it has been getting things unthinkable in the past. Adding a high socio-economic interest for this type of energy in recent years, there have been numerous prototypes of solar aircraft with exceptional

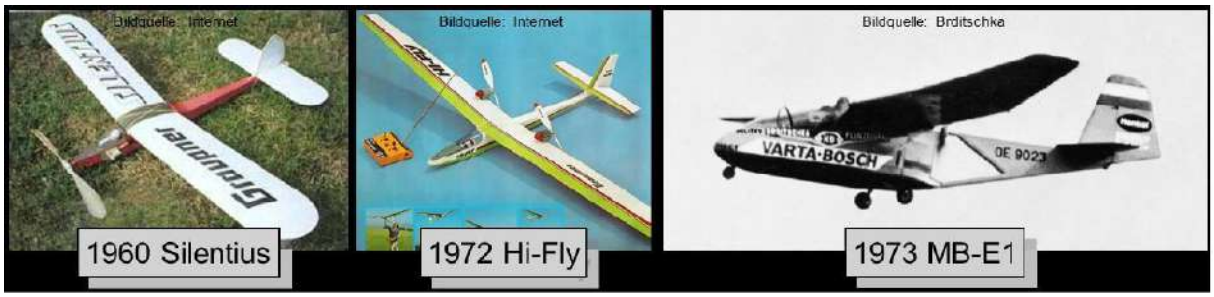

Figure 2.2: Development steps performed by Fred Militky leading to man-carrying electric aircraft [Hepperle, 2012].

results.

2.2 History of Solar Powered Flight

In this section, a brief history of solar powered aircraft will be exposed. The use of electric power for aircrafts is not new, on the 30th of June 1957, Colonel H. J. Taplin of the United Kingdom made the first officially recorded electric powered radio controlled flight with his model ”Radio Queen”, which used a permanent-magnet motor and a silver-zinc battery. Three months later, on October 1957, Fred Militky achieved a successful flight with an uncontrolled model. Subsequent developments in electric aircraft were characterized by improving the performance of electric motors and batteries [Noth, 2008b, Iroquois, 2013].

The key advancement in solar cells technology occurred in 1954 at Bell Telephone Laboratories [EERE, 2013], when Daryl Chapin, Calvin Fuller, and Gerald Pearson created the first silicon photovoltaic cell capable of using the sun’s rays to convert energy into power to run electrical equipment. The efficiency improved rapidly from 4% to 11% allowing greater use of solar energy [Noth, 2008b].

First data from unmanned solar flight

The first prototype was designed by R.J. Boucher from Astro Flight Inc, Sunrise I had a wingspan of 9.76 meters, weighed 12.25 kilograms and 450W power output from 4096 solar cells, as shown Fig. 2.3(a) [Boucher, 1984]. It flew for the first time on the 4th of November 1974, at Camp Irwin, California. This aircraft flew 20 minutes at an altitude of 100 meters during its inaugural flight and was later able to fly for more than three hours, but the aircraft’s career ended after it was damaged in a sandstorm. The company later built Sunrise II, which weighed less and was able to output more power, 600 W, in comparison to the Sunrise I [Noth, 2008b].

In the years following the Sunrise aircrafts, there was a greater passion for solar powered flight and many people began to use solar cells for their aircrafts designs. Some examples are Solar Solitude built by Dave Beck from Wisconsin, who set two records in the model airplane solar category F5 open SOL of the FAI [FAI, 2013], or the Solar Excel (Fig. 2.3(b)) built by Wolfgang Schaeper, from 1990 to 1999 in Germany, who holds now all the official records: duration (11h 34m 18s), distance in a straight line

(a) Sunrise I (1974)

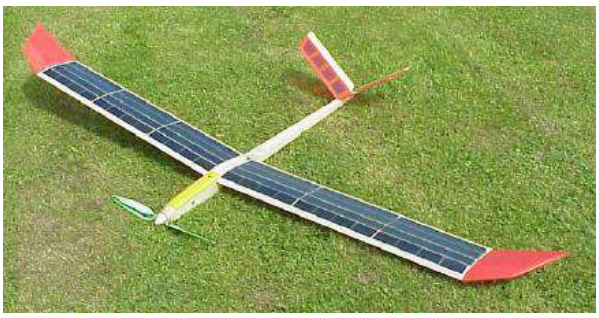

(b) Solar Excel (1990)

Figure 2.3: Sunrise I (1974) and Solar Excel (1990) [Noth, 2008b].

(48.31 km), gain in altitude (2065 m), speed (80.63 km/h), distance in a closed circuit (190 km) and speed in a closed circuit (62.15 km/h) [Noth, 2008b].

The beginnings of manned solar aircraft

After having flown, with some success, solar model airplanes mainly applied for aeromodelling and proved it was feasible with sufficient illumination conditions, the pioneers thought at the end of the 70's in the dream of manned flights powered solely by the solar irradiance. In this seccion, the more representative solar manned aircrafts will be exposed.

On April 29, 1979, occurred the first manned flight with the Solar Riser (Fig. 2.4) at Flabob Airport, California. Solar Riser was designed by Larry Mauro a solar version of his Easy Riser hang glider. The battery was charged by a series of photovoltaic solar panels mounted in the top wing that provided 350 Watts of power. The solar cells was not sufficient to provide power in flight and all flights were made by recharging the battery on the ground from the solar cells and then flying using energy stored in the battery. A charge in bright sunshine for an hour and a half yields a flight of 3-5 minutes. The aircraft reached a maximum height about 12 m and flew 0.8 km [Boucher, 1984].

Figure 2.4: Solar Riser(1979) [Noth, 2008b].

The technology to fly only by solar energy without any storage was reached by Dr. Paul B. McCready and AeroVironment Inc, the company he founded in 1971 in Pasadena, California. The Gossamer

Penguin was a scaled-down version of the Gossamer Albatross, and had been designed as a backup aircraft for that project. When MacCready decided to pursue piloted solar-powered aircraft, his team first turned to the smaller version of the Albatross. With thirteen-year old Marshall MacCready (MacCready's son) was the first pilot of the Gossamer Penguin, and he made the first manned solar-powered flight on 18th of May 1980, as shown Fig. 2.5(a). Then the efforts of MacCready turned to the Solar Challenger. This aircraft, seen in Fig. 2.5(b), had a 14.2 m wingspan high-wing monoplane with 16128 solar cells offering 2500W at sea level. On July 7, 1981, it flew 262.3 km in 5 hours 23 minutes, with solar energy as its sole power source and without energy stored system on board [Noth, 2008b].

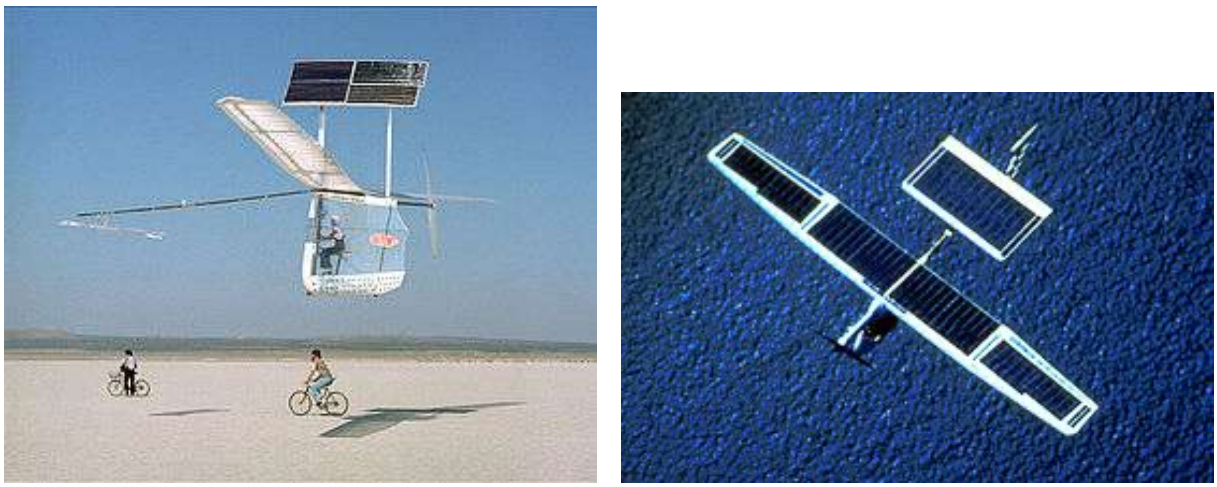

(a) Gossamer Penguin (1980). (b) Solar Challenger (1981).

Figure 2.5: Gossamer Penguin (1980) and its successor, Solar Challenger (1981) [Noth, 2008b].

Meanwhile in Germany, Günter Rochelt designed and built the Solair I, seen in Fig. 2.6(a), an aircraft with 16m wingspan based on the Canard 2FL from AviaFiber that he slightly modified and covered with 2499 solar cells providing 1800 W [Boucher, 1984]. Moreover Solair I had installed a 22.7 kg nickel-cadmium battery because the wing area of solar cells did not provide enough energy. On the 21st of August 1983 Rochelt flew in Solair I during 5 hours 41 minutes.

Figure 2.6(b) shows another important design, the Sunseeker. This aircraft was created by Eric Raymond in USA, that due to the influence of other designs, Solar Riser and Solar Challenger, he built his own manned solar powered aircraft. In August 1990, Sunseeker crossed the USA in 21 flights with 121 hours in the air, the first solar aircraft to achieve it [Noth, 2008b].

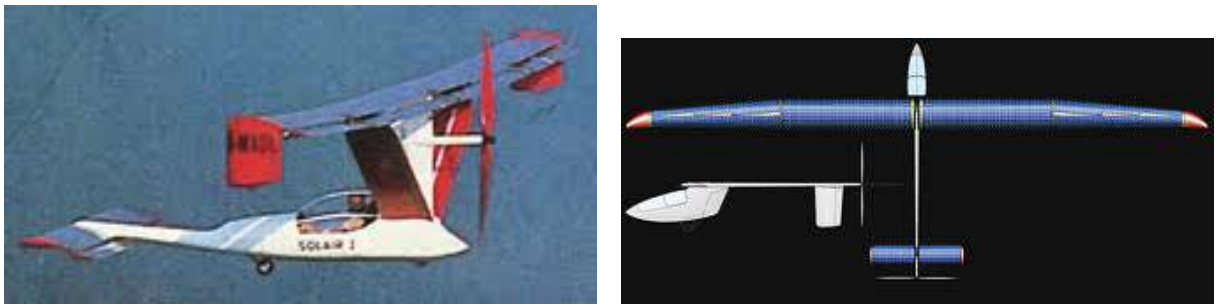

(a) Solair I (1981). (b) Sunseeker (1990).

Figure 2.6: Solair I (1981) and Sunseeker (1990) [AE, 2008].

High Altitude Long Endurance (HALE) Aircrafts

AeroVironment Inc. with the assistance of NASA have been developed some of the most current High Altitude Long Endurance (HALE) UAVs. Figure 2.7 shows some aircraft that have been built and it will now be mentioned [Noll et al., 2004].

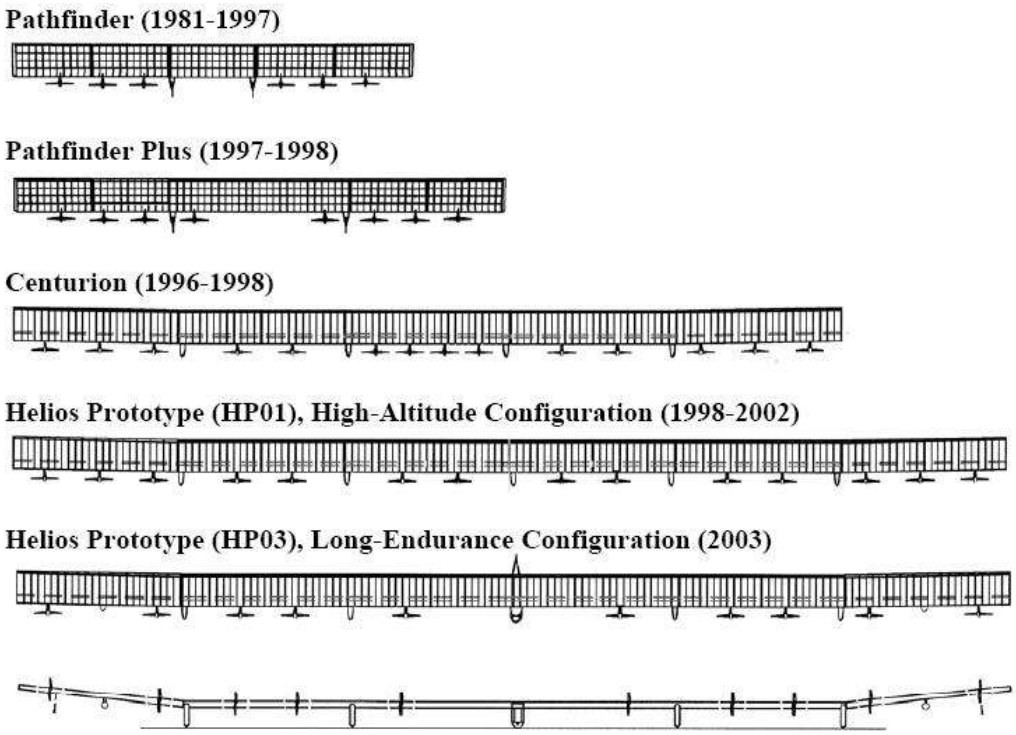

Figure 2.7: Solar aircraft evolution through the ERAST program [Noll et al., 2004].

The initial design of the Pathfinder was created by AeroVironment, the RAPTOR/Pathfinder. It was the first experimental prototype High Altitude Solar (HALSOL), having its wing covered with solar panels that generated peak power of 11.4 kW to drive its eight small electric motors. The RAPTOR/Pathfinder could carry a payload of 41 kg. The Pathfinder went into NASA service generally unchanged from its initial configuration, except for elimination of two motors, leaving six. In 1997, the Pathfinder broke a world's record for high-altitude flight by a propeller-driven aircraft when it reached an altitude of over 21,650 m. Following the good results obtained in the original Pathfinder flights, NASA then upgraded the Pathfinder to an improved configuration, the "Pathfinder Plus". Pathfinder Plus, seen in Fig. 2.8(a), featured a 6.7 m wing stretch to give a total wingspan of about 37 meters, the number of motors was restored to eight, and more and improved solar cells were used. The improvements gave the Pathfinder Plus an increased take-off weight of 315 kg [Noll et al., 2004, Flittie and Curtin, 1998].

In August 1998, Pathfinder Plus broke the Pathfinder's altitude record by reaching an altitude of over 24,400 m. However, it was intended simply as a stepping stone to an even bigger solar-powered UAV, the "Centurion". AeroVironment rolled out the Centurion (Fig. 2.8(b)) in the summer of 1998, and the UAV made its first flight in November 1998, with a pilot at the controls. It had a wingspan of 62.8 meters, was powered by twelve electric motors, had four gondolas instead of two, and weighed 630 kilograms.

It was expected to reach up to 30500 meters [Noll et al., 2004].

(a) Pathfinder (1993). (b) Centurion (1997-1999).

Figure 2.8: Pathfinder (1993) and Centurion (1997-1999) [NASA, 2013b].

The Centurion prototype was expanded to act as a Helios prototype, part of at the family of aircraft of ERAST (Environmental Research Aircraft and Sensor Technology), with a wingspan of 75.3 meters, five gondolas, and fourteen electric motors. The Helios (Fig. 2.9(a)) prototype first flew in the fall of 1999. It flew under battery power, since the lightweight solar cells required were expensive. On 13 August 2001, the Helios prototype established an absolute altitude record for a non-rocket-propelled aircraft of 29,420 meters, flying from the Hawaiian island of Kauai. Unfortunately, the aircraft was lost in a crash on Kauai on 26 June 2003 as shown Fig. 2.9(b), due to structural failures. Pathfinder Plus remained in service up to 2005, with the number of motors reduced to six again after the Helios crash to permit carriage of air sensing booms. It was finally retired in 2005 and is now in at the Smithsonian museum [Noll et al., 2004].

(a) Helios (1999-2003). (b) Helios falling towards the Pacific Ocean (2003).

Figure 2.9: Helios (1999-2003) and aircraft crash (2003) [NASA, 2013b].

Another example of a long endurance UAV, with the same purpose as Helios, is the Solong aircraft as depicted Fig. 2.10(a). Solong has a wingspan of less than 5 meters and is able to fly continously using only solar energy and thermal energy. The president and founder of ACPropulsion, Alan Cocconi, flew his Slong on the 22^{nd} of April 2005 during 24 hours and 11 minutes. Two months later, the aircraft

was able to fly for over 48 hours, proving the feasibility of eternal flight [AE, 2008].

Many projects were also conducted in Europe, such as the Zephyr (Fig. 2.10(b)). The British company, QinetiQ, tested the Zephyr aircraft in New Mexico in December 2005 and it was able to fly for six hours and reaching an altitude of 7,925 meters. The crowning achievement of the Zephyr was on the 10th of September 2007, when the aircraft flew continuosly for 54 hours and it was able to reach a peak altitude of 17,786m. In the future QinetiQ hopes to have the Zephyr aircraft do a test flight of several months at an altitude over 15,240 meters [QinetiQ, 2013, Rapinett, 2009].

(a) Solong (2005). (b) Zephyr (2005).

Figure 2.10: Solong (2005)and Zephyr (2005) [AE, 2008, QinetiQ, 2013].

A solar powered manned flight was achieved with the Solar Impulse [SI, 2013]. Solar Impulse is a Swiss long-range solar powered aircraft project being undertaken at the École Polytechnique Fédérale de Lausanne, it has 63 m wingspan, 21.85 m length, 11628 solar cells and a maximum take off weight of 2000 Kilograms. The project eventually hopes to achieve the first circumnavigation of the Earth by a piloted fixed-wing aircraft using only solar power. The project is led by Swiss psychiatrist and aeronaut Bertrand Piccard which began development in 2003, who co-piloted the first balloon to circle the world non-stop, and Swiss businessman André Borschberg. The first aircraft as depicted in Fig. 2.11, bearing the Swiss aircraft registration code of HB-SIA, is a single-seater monoplane, capable of taking off under its own power, and intended to remain airborne up to 36 hours.

Figure 2.11: Solar Impulse [SI, 2013].

On July 8, 2010, the Solar Impulse completed a 26 hours flight using only solar energy, the first

flight of its kind. In 2012, Piccard and Borschberg conducted successful solar flights from Switzerland to Spain and Morocco. In 2013, plans call for a flight from California to Virginia. Building on the experience of this prototype, a slightly larger follow-on design (HB-SIB) is planned to make a circumnavigation of the globe in 20–25 days. This flight was initially planned for 2014, but following a structural failure of the aircraft's main spar during static testing, a more likely date is 2015.

On a different front, the Defense Advanced Research Projects Agency (DARPA) is researching a future solar-powered HALE UAV. The new project is called Vulture (Fig. 2.12) and the main idea is to combine the key benefits of both, aircraft and satellite into one system, and keep the system in the air continuously for five years. As of September 15, 2010, the Vulture system entered in the technology phase, and a concept of the aircraft was designed [DARPA, 2013]. DARPA will continue to work with Boeing to advance this technology further and functional prototype will be built within the next three years.

Figure 2.12: Artistic rendering of Vulture Objective System [DARPA, 2013].

Chapter 3

Solar UAV, Mission and Energy Management

The content of this chapter describes the relevant aircraft characteristics to the design of its propulsion system, its mission and the corresponding energy requirements. This chapter is a very important part in the project because, depending on the characteristics of the aircraft and its mission, the necessary energy requirements can be determined only after these parameters are well defined, after witch can one proceed in designing and sizing the propulsion system.

3.1 Aircraft Description

The propulsion system that will be designed is meant for a small aircraft. This is part of a much larger collaboration project that involves several research institutes of LAETA [LAETA, 2013], in particular CCTAE [CCTAE, 2013], IDMEC [IDMEC, 2013], AEROG [AEROG, 2013] and INEGI [INEGI, 2013]. At the present, the conceptual design of the airframe has been completed and some of the UAV specifications relevant to the design of the propulsion system are summarized in Tab. 3.1.

Parameter	Symbol	Value	Units
Wing mean chord	c	0.335	m
Wingspan	b	4.53	m
Wing area	S_{ref}	1.518	m^2
Take off weight	W	48.12	N

Table 3.1: Solar UAV characteristics.

Although it is a small aircraft, with a mass less than 5 Kg, its wing in addition to its aerodynamic function, has an appropriate area to place the solar cells. The airfoil shown in Fig. 3.1 is another important factor. It is an essential part from the point of view of aerodynamics and, in this project, it has added importance because factors such as the airfoil curvature can be important when attaching the solar panels that will also have to conform to this curvature and, thus, must have some flexibility.

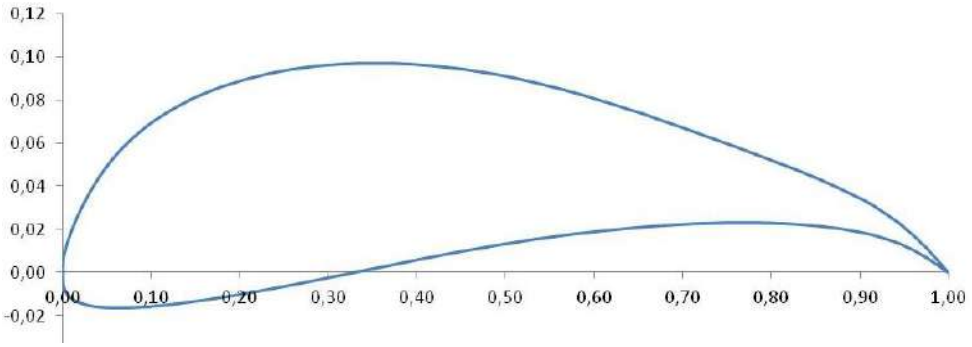

Figure 3.1: Airfoil of solar UAV in non-dimensional coordinates.

Solar Cells Location

The solar cells are to be installed on the wing upper surface. The area available S_{PV} will be less than the reference area S_{ref} shown in Tab. 3.1 due to factors related to the airfoil profile shape. The estimate of S_{PV} is obtained by using three correction factors applied to S_{ref}:

1. Curvature correction factor at the leading edge, CF_{LE}.

   To correct the curvature excess in this area, linked directly with the flexibility of the cells and problems with possible low radiation levels.

2. Correction factor at the trailing edge, CF_{TE}.

   Occupied area by the control elements, ailerons and flaps.

3. Wingspan correction factor, CF_W.

   At the ends of each wing there must be a safety zone.

Table 3.2 shows the values of these coefficients.

Correction factor	Symbol	Value (%)
Leading edge	CF_{LE}	15
Trailing edge	CF_{TE}	10
Wingspan	CF_W	18

Table 3.2: Correction factors to estimate available solar panel area.

The values c_{PV}, b_{PV} and S_{PV} were computed as:

$$c_{PV} = \frac{100 - CF_{LE} - CF_{TE}}{100} \cdot c \tag{3.1}$$

$$b_{PV} = \frac{100 - CF_W}{100} \cdot b \tag{3.2}$$

$$S_{PV} = c_{PV} \cdot b_{PV} \tag{3.3}$$

Parameter	Symbol	Value	Units
Wing mean chord with CF	c_{PV}	0.251	m
Wingspan with CF	b_{PV}	2.899	m
Wing Area with CF	S_{PV}	0.728	m^2

Table 3.3: Available area for solar panels.

The resulting available values of chord, wingspan and area are shown in Tab. 3.3.

At this point, an area where the solar cells can be installed have been estimated. An important part of the study will be to select and size the solar panels optimally.

3.2 Aircraft Mission

The increase in the rate of forest fires is a reality that can not be denied. Extinction tasks are important but the key is early detection but this task is complicated especially in mountain areas of difficult access. The mission for the aircraft is the observation and surveillance of land inaccessible to conventional observation methods, applied to the detection of fires in particular and forest surveillance method to obtain useful information in general.

The region of operation for the solar UAV determines the available solar radiation so the mission is situated in a particular place and bounded. This is done in Chapter 5.

Mission Characteristics

The solar UAV has a mission that is divided into the following parts:

1. Take off.

   The mission begins at this point with an estimated duration of 1 second, without taking into account the rolling period.

2. Climb.

   In this part, with an estimated duration of 10 minutes, the objective is to reach a cruise flying altitude of 1000 m above the runway level.

3. Cruise.

   This is the most important part of the mission, where the tasks of monitoring and data recording are carried out. Its endurance is target to 8 hours.

4. High speed.

   This is an optional stage where the UAV operates at full load. It is not included in the nominal mission but might be required in some operations.

5. Descent.

It is the final part of the mission in which the UAV loses altitude to prepare for landing. The approximate duration time is 29 minutes, but depends on the speed of descent.

6. Landing.

   It includes final approach and touch down.

The described nominal mission is graphically shown in Fig. 3.2.

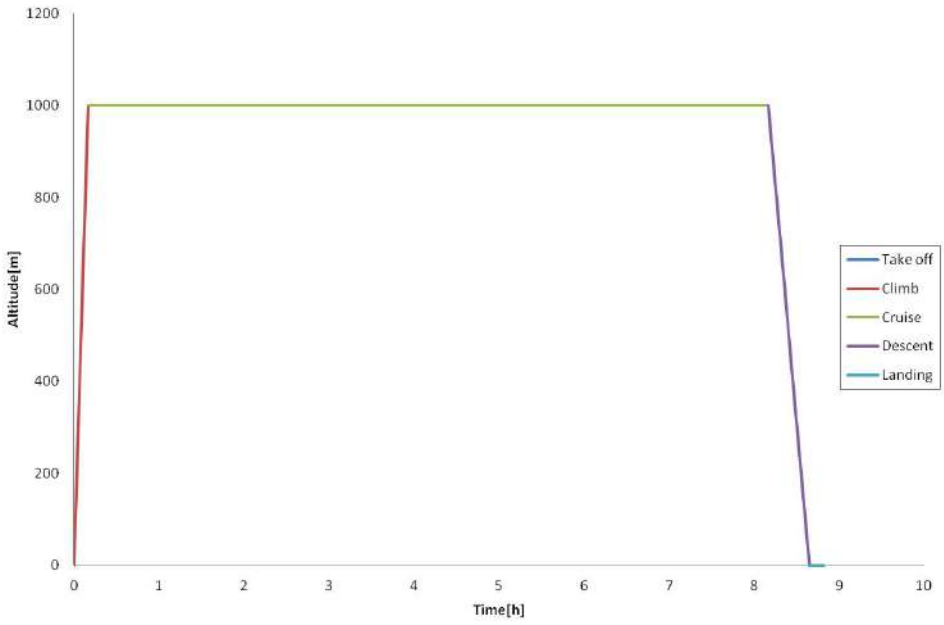

Figure 3.2: Mission of solar UAV.

The aircraft aerodynamic parameters have been calculated by the aerodynamic specialist in the project. For each mission segment, the flight speed (v), altitude (h), maximum lift coefficient(C_{Lmax}), lift coefficient (C_L), parasite drag coefficient (C_{Dp}), induced drag coefficient (C_{Di}), drag coefficient(C_D), air density (ρ), lift-drag ratio (L/D), lift force (L) and drag force (D)are summarized in Tab. 3.4.

Aerodynamics	v (m/s)	h (m)	C_{Lmax}	C_L	C_{Dp}	C_{Di}	C_D	ρ (kg/m^3)	L/D	L (N)	D (N)
Take off	4.91	0	1.557	1.062	0.0304	0.0120	0.0424	1.225	25.047	23.80	0.95
Climb	7.29	1000	1.552	1.081	0.0261	0.0291	0.0552	1.112	19.583	48.47	2.48
Cruise	7.29	1000	1.552	1.081	0.0261	0.0291	0.0552	1.112	19.583	48.47	2.48
High speed	20.66	1000	1.539	0.140	0.0304	0.0015	0.0319	1.112	4.389	50.42	11.49
Descent	10.44	1000	1.547	0.526	0.0212	0.0078	0.0290	1.112	18.138	48.37	2.67

Table 3.4: Aerodynamic characteristics of the aircraft.

Naturally, this mission will only be possible in locations where solar radiation is sufficient to meet the energy requirements, i.e, it is necessary a minimum radiation profile. In Chapter 5 the location where the mission will take place will be defined.

3.3 Energy Requirements

For this particular mission, the energy requirements have been calculated based on the efficiency of each component of the propulsion system.

Considering the efficiency of the different components of the propulsion system in every part of the mission, the energy required can be estimated. These efficiencies are previously established and shown in Tab. 3.5. The efficiency of battery, cables and ,Electronic Speed Controller, ESC is fixed for the entire mission while the efficiency of the electric motor and propeller are different in each stages.

Component	Take off	Climb	Cruise	Descent
Battery	100%	100%	100%	100%
Cable	100%	100%	100%	100%
ESC	95%	95%	95%	95%
Electric motor	89.01%	89.3%	89.15%	stop
Propeller	17.2%	25.41%	46.64%	-

Table 3.5: Efficiency of the propulsion system components at each mission stage.

Combining the data from Tab. 3.4, the power required for each stage of the mission can be estimated as

$$P_{req} = v_{stage} \cdot D_{stage}\,, \tag{3.4}$$

where v_{stage} is the corresponding aircraft speed and D_{stage} is the aircraft drag.

Knowing the duration of each stage t_{stage}, it is then possible to calculate the energy required at each stage of the mission,

$$E_{req} = P_{req} \cdot t_{stage}\,. \tag{3.5}$$

Applying the total efficiency of the components, it is possible obtain the final energy of the propulsion system. In this calculation it is added gravitational potential energy corresponding to the stage of the climb. Below is particularized for each segment of the mission:

1. Take off energy

   The total efficiency of the components for take off can be estimated as:

   $$\eta_{Ttoff} = \eta_B \cdot \eta_C \cdot \eta_{ESC} \cdot \eta_{E_{toff}} \cdot \eta_{P_{toff}}\,, \tag{3.6}$$

   where η_B, η_C and η_{ESC} are the efficiency of battery, cables and Electronic speed controller, common for all stages . While $\eta_{E_{toff}}$ and $\eta_{P_{toff}}$ are the efficiency of electric motor and propeller for take off.

   Then the required energy can be determined as:

   $$E_{req} = (\frac{1}{\eta_{Ttoff}} \cdot P_{req}) \cdot t_{toff}\,, \tag{3.7}$$

   where η_{Ttoff}, P_{req} and t_{toff} are total efficiency, power and time for take off respectively.

2. Climb energy

   The total efficiency of the components for climb can be estimated as:

$$\eta_{Tcli} = \eta_B \cdot \eta_C \cdot \eta_{ESC} \cdot \eta_{E_{cli}} \cdot \eta_{P_{cli}} \,, \tag{3.8}$$

   where $\eta_{E_{cli}}$ and $\eta_{P_{cli}}$ are the efficiency of electric motor and propeller for climb.

   Then the required energy can be determined as:

$$E_p = m \cdot g \cdot h \,, \tag{3.9}$$

$$E_{req} = E_p + (\frac{1}{\eta_{Tcli}} \cdot P_{req}) \cdot t_{cli} \,, \tag{3.10}$$

   where E_p is gravitational potential energy, m is the mass of UAV, g is gravitational acceleration constant ($9,81 m/s^2$) and h is the altitude in this case 1000 m. η_{Tcli}, P_{req} and t_{cli} are total efficiency, power and time for climb respectively.

3. Cruise energy

   The total efficiency of the components for cruise can be estimated as:

$$\eta_{Tcru} = \eta_B \cdot \eta_C \cdot \eta_{ESC} \cdot \eta_{E_{cru}} \cdot \eta_{P_{cru}} \,, \tag{3.11}$$

   where $\eta_{E_{cru}}$ and $\eta_{P_{cru}}$ are the efficiency of electric motor and propeller for cruise.

   Then the require energy can be determined as:

$$E_{req} = (\frac{1}{\eta_{Tcru}} \cdot P_{req}) \cdot t_{cru} \,, \tag{3.12}$$

   where η_{Tcru}, P_{req} and t_{cru} are total efficiency, power and time for cruise respectively.

4. Descent energy

   At this stage no energy is required because it's assuming that the engine is stopped then the UAV descends planning.

Mission Stage	Total efficiency $\eta_T\,[\%]$	Power required $P_{req}\,[W]$	Energy required $E_{req}\,[KJ]$
Take off	14.54	32.07	0.03
Climb	21.55	455.75	273.45
Cruise	35.51	50.81	1463.34
Descent	0	0	0
TOTAL			1736.82

Table 3.6: Energy required for the propulsion of the UAV.

The values for the required power and energy for each mission stage are summarized in Tab. 3.6. The total energy required ($E_{req} = 1737KJ$) and the maximum power requider ($P_{req} = 455W$) will be the basis for the sizing of the propulsion system. Figure 3.3 shown the power distribution for the complete mission.

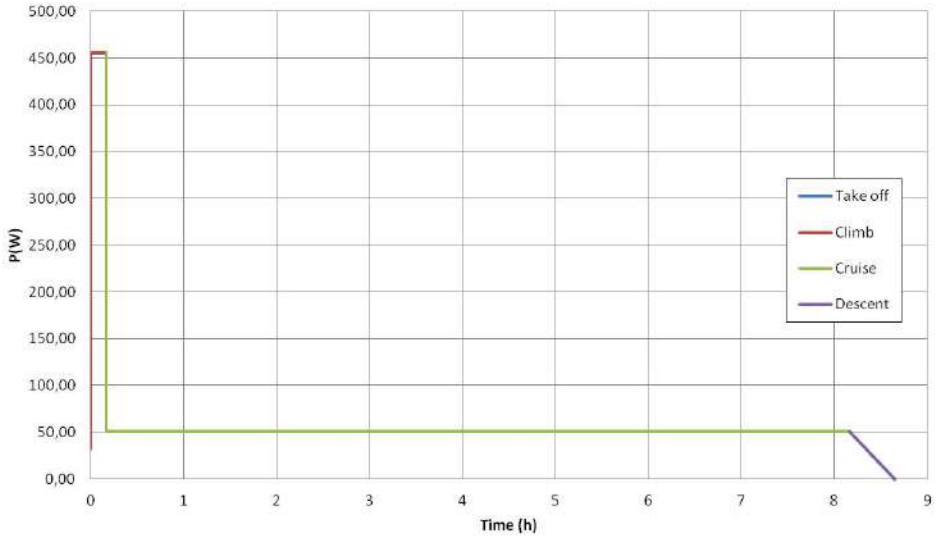

Figure 3.3: Power of the mission at every stage of the flight.

Chapter 4

Propulsion System Configuration

Before proceeding with the design and configuration of the solar-powered system, it is necessary to study conventional propulsion systems, new electrical systems and also the possibility of combining both. A complete study of all possibilities will be help full in the design of the propulsion system, specially if the mission requires obtaining hybrid systems to optimize the performance of the propulsion.

Figure 4.1 shows the types of propulsion applied to aeronautical engineering in general, for air transport and space missions.

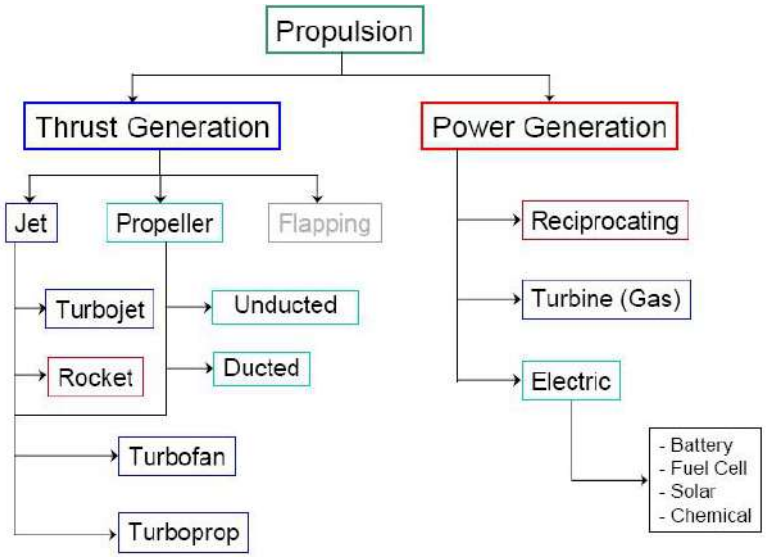

Figure 4.1: Propulsion systems [Juste, 2012].

4.1 Conventional Combustion Systems

Traditional forms of propulsion have one thing in common, independently of engine type, that is, produce energy from the combustion of a fossil fuel.This fuel is usually based on oil and is thermally decomposed, i.e. burnt. Technically, with small modifications, these systems are also capable of using gaseous fuels like hydrogen or natural gas. The fuel is burnt in either piston engines or in gas turbines to produce me-

chanical power. These machines are connected to a shaft which is linked to an aerodynamic propulsion device, either a propeller (piston-propeller or turbo-propeller) or a fan (turbo-fan). All systems accelerate an incoming mass flow of air to produce thrust. An additional part of the thrust may be created by recovering part of the thermodynamic energy in the exhaust, i.e. by passing the hot gases through suitable nozzles. In case of propulsion by propellers, it is often necessary to use a gearbox to adapt the performance characteristics of the core engine to the characteristics of the propulsion device so that the overall efficiency is maximized. Gearboxes are now also introduced to decouple the fan from the turbine of turbofan engines, thus increasing their total efficiency considerably [P&W, 2013].

A schematic of these conventional propulsion systems is illustrated in Fig. 4.2. A notable feature of these propulsion systems is that they burn the fuel and the exhaust is emitted into the atmosphere. Besides affecting the environment, this also reduces the mass of the airplane during the flight and therefore affects the performance.

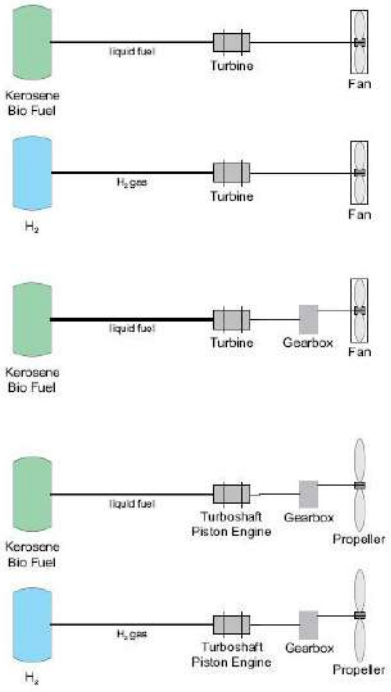

Figure 4.2: Different propulsion systems exploiting the energy in the fuel by burning it [Hepperle, 2012].

Each propulsion system will have a particular area of operation because each engine type will operate only within a certain range of altitudes and Mach numbers (velocities). Similar limitations in velocity and altitude exist for airframes. It is necessary, therefore, to match airframe and propulsion system capabilities. Figure 4.3 shows the approximate velocity and altitude limits, or corridor of flight, within which airlift vehicles can operate. The corridor is bounded by a lift limit, a temperature limit, and an aerodynamic force limit. The lift limit is determined by the maximum level-flight altitude at a given velocity. The temperature limit is set by the structural thermal limits of the material used in construction of the aircraft. At any given altitude, the maximum velocity attained is temperature-limited by aerodynamic heating effects. At lower altitudes, velocity is limited by aerodynamic force loads rather than by temperature. The operating regions of all aircraft lie within the flight corridor. The operating region of a particular aircraft

within the corridor is determined by aircraft design, but it is a very small portion of the overall corridor. Superimposed on the flight corridor in Fig. 4.3(a) are the operational envelopes of various powered aircraft. The operational limits of each propulsion system are determined by limitations of the components of the propulsion system and are shown in Fig. 4.3(b).

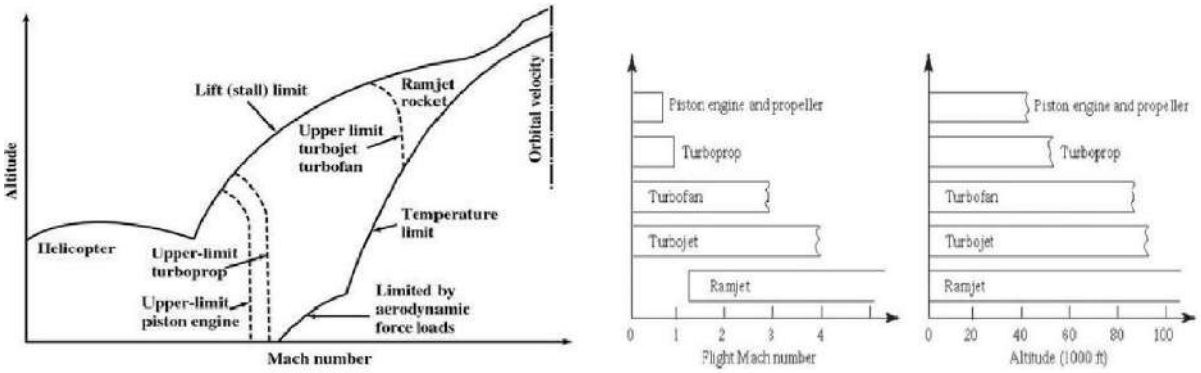

(a) Flight Limits.

(b) Engine Operational Limits.

Figure 4.3: Flight limits and engine operational limits [Juste, 2012].

Described conventional propulsion systems, it is time to particularize to the case of the UAV. In this case, the form of propulsion is similar to the previous engines. Generally, they have been derived from conventional aero-engine, by downscaling procedures. However, the design considerations are different and new problems arise due to the final application and reduced scale.

Traditionally UAV engines have been small reciprocating engines or small gas turbines (tubojets), characterized by low specific consumption and a high relation Thrust/Weigth.

In the case of turbojet for UAV, the differences to conventional engines for large aircraft are purely economic. The philosophy of these engines is very different because they are limited-life engines. From a cost viewpoint, it is most effective to eliminate the maintenance needs and design the engine like a unity disposable and with limited life. A limited life implies a different design: lifetimes between 50-250 hours. Compared with a civil aircraft engine which has more than 20.000 hours of lifetime, the difference is very representative. Figure 4.4 shows the different philosophy of each propulsion system based on the associated cost.

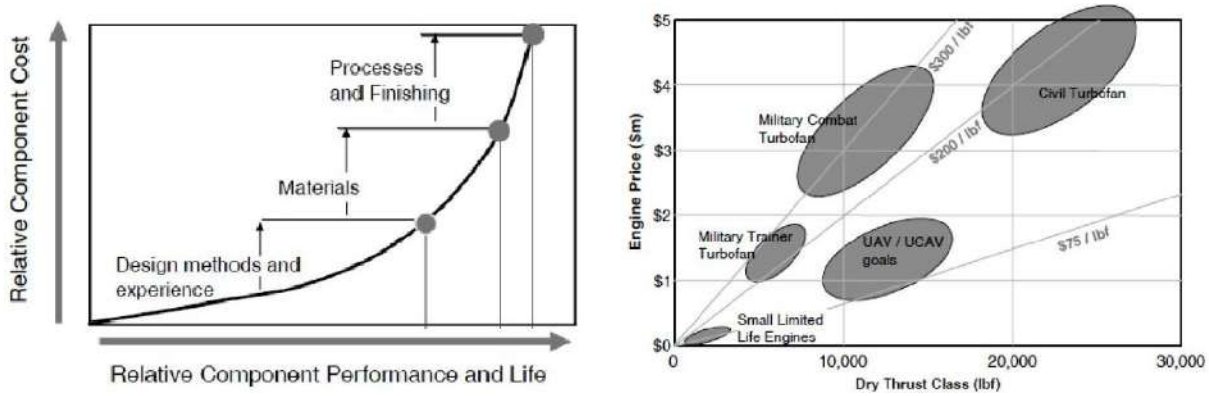

(a) Distribution of UAV costs.

(b) Different lifetime.

Figure 4.4: Different investment philosophies in UAV propulsion [Juste, 2012].

4.2 Electric Systems

In case of electric propulsion systems, there are a large number of possible concepts, they differ in the type of energy storage and conversion. Today, mainly three systems are of interest: fuel cell based systems, battery based systems and solar panels systems. All these systems are under constant development, driven by automotive and other mobile applications.

Fuel Cell Systems

A fuel cell is a device that converts the chemical energy from a fuel into electricity through a chemical reaction with oxygen or another oxidizing agent. Hydrogen is the most common fuel, but hydrocarbons such as natural gas and alcohols like methanol are sometimes used. Fuel cells are different from batteries in that they require a constant source of fuel and oxygen to run, but they can produce electricity continually for as long as these inputs are supplied. Welsh Physicist William Grove developed the first crude fuel cells in 1839 [Morus, 2005]. The first commercial use of fuel cells was in NASA space programs to generate power for probes, satellites and space capsules [NASA, 2013a]. Since then, fuel cells have been used in many other applications. Fuel cells are used for primary and backup power for commercial, industrial and residential buildings and in remote or inaccessible areas. They are used to power fuel cell vehicles, including automobiles, buses, forklifts, airplanes, boats, motorcycles and submarines.

In addition to electricity, fuel cells produce water, heat and, depending on the fuel source, very small amounts of nitrogen dioxide and other emissions. The energy efficiency of a fuel cell is generally between 40–60%, or up to 85% efficient if waste heat is captured for use.

The problem with this technology is the difficult storage, high weight and a relatively low range. Due to the high weight, this system is used in light UAVs.

Battery Systems

In this type of systems, the energy is stored in batteries which allows for a direct extraction of electric power. The efficiency is limited by the chemical processes occurring during charging and discharging. In most cases, the mass of the system is usually not changing, except for some specific air breathing cells like Li-O2. Battery systems are used in small UAVs and the key factor is density power and relation weight/energy. A more detailed study will be doing in Chapter 6.

Solar Panels Systems

Solar panels convert solar energy into electricity. This system stores energy during the day (either previous systems) and permit the possibility of night operations. Again, Chapter 6 will including a detailed study of such systems.

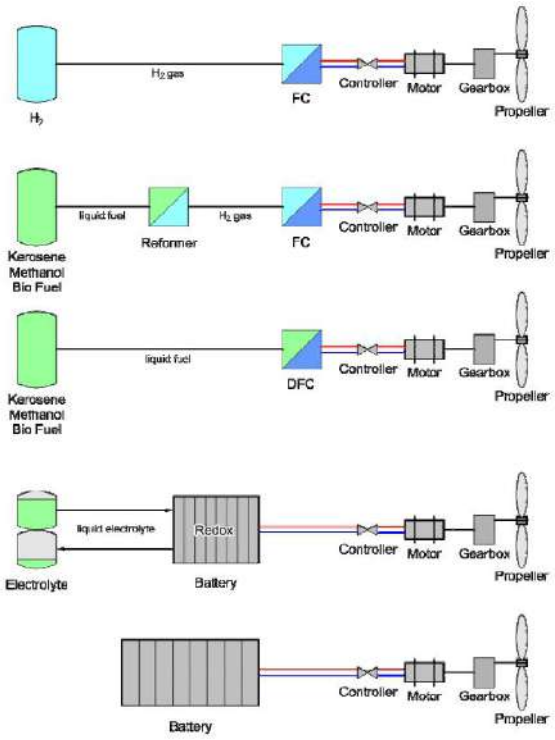

Figure 4.5: Components of different electric propulsion systems [Hepperle, 2012].

4.3 Hybrid Systems

Hybrid technology works with some success in the automotive world in recent decades, and every day is strongest in our society. This technology is being introduced in the world of aviation, although only significantly for light aircraft, small UAVs and similar. Aeronautics may give several cases of hybrid propulsion, battery-powered electric motor combined with combustion systems of engine (jet or piston), or combining any technologies mentioned in section 4.2.

Hybrid aircrafts, such the one shown in Fig. 4.6 can combine a combustion engine and electric motors [Vycital and Moravec, 2013]: it is a combination of two propeller propulsion units, one of which is based on the principle of an internal combustion engine (1) and the second one on the principle of an electric motor (2). The propulsion units are installed without an interdependent mechanical coupling in the push-pull configuration in the direction of flight on the aircraft fuselage, so that one of the propulsion units is located in the forward fuselage and generates a propulsion effect using a tractor propeller and the second one of the propulsion units is located in the rear fuselage and generates a propulsion effect using a pusher propeller. The batteries supplying the energy to the electric motor are rechargeable by recuperation during flight from the electric motor with a propeller (2) and/or from a generator installed on the internal combustion engine (1).

Another common example of hybrid propulsion is the combination of fuel cell and a Li ion battery. In this case there is only one electric motor, these two systems provide the energy necessary for the operation of the engine and, this last the propeller.The operation of one or the other depends on the type of mission but generally are used together in take off and climb. During cruise, the battery is

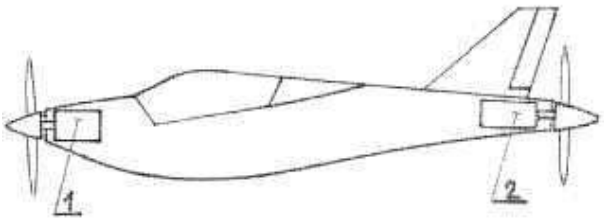

Figure 4.6: Example of aircraft hybrid (combustion engine + electric motor) [Vycital and Moravec, 2013].

disconnected and the fuel cell supplies all the power required to maintain a straight level flight. The battery may be recharged in flight if other additional systems of charge, for example a solar panels are present.

4.4 Comparison of the Different Configurations

Compare the different propulsion systems is not easy since there are multiple factors to be considered. The energy required for a flight must be stored on-board. For application in aircraft the most important parameters are the energy per mass $E^*$and to a lesser extent the energy per volume V^*. These specific values are shown in Fig. 4.7 for various energy storage systems. It can be seen that even the most advanced current battery storage systems fall short of the parameters of Kerosene. While the factor in specific volume is only about 18, the factor in mass specific energy density is in the order of 60. This is a core problem for application in aviation and imposes strict limits for battery powered systems.

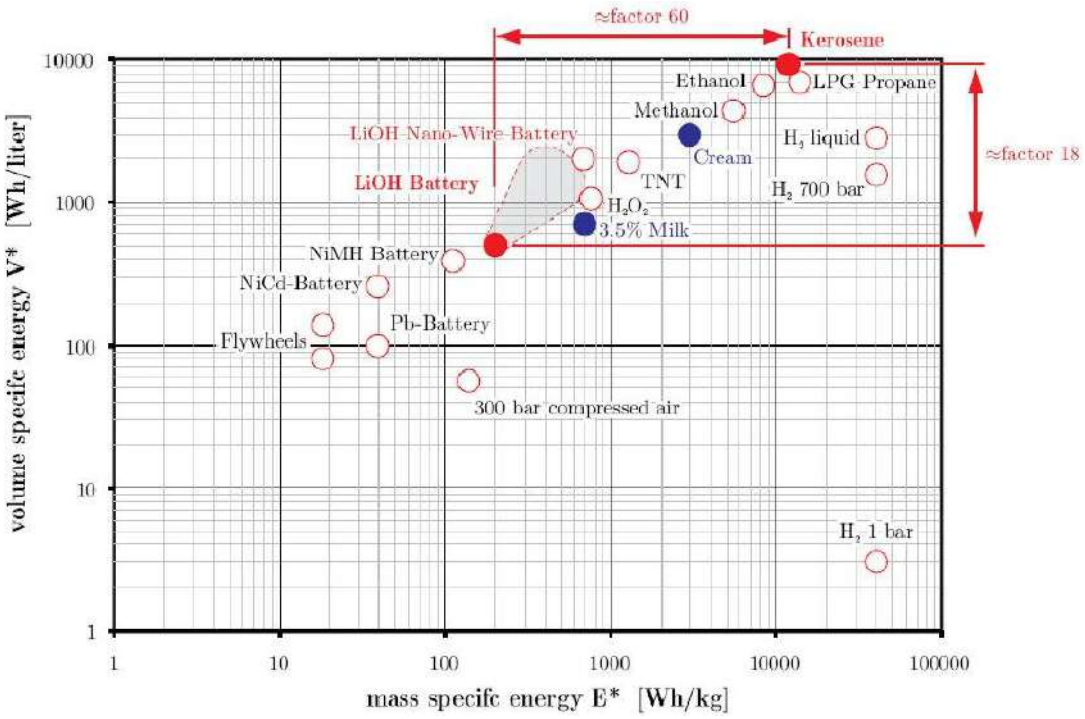

Figure 4.7: Volume and mass specific energy characteristics of different energy storage systems [Hepperle, 2012].

The lower volume specific energy content is less critical as long as the aircraft design is not limited by internal volume. Otherwise the vehicle would require larger wings or fuselages or additional external "energy pods" which would lead to losses in overall aircraft efficiency due to larger wetted surface. Of course, there are ideas to incorporate batteries and other storage systems into the primary structure, but these are still rather far from practical application. In case, of fuel cells hydrogen can be stored in porous metal, but the weight of these foams is very high and appears unsuitable for aeronautical application. However, such systems have been used in marine applications, where the additional mass is less critical. Table 4.1 lists some characteristics, advantages and disadvantages of energy storage systems.

Energy storage	Characteristics
Kerosene, AVGAS	Can be stored in wing and fuselage tanks. These are often part of the structure and therefore of low mass.
Hydrogen (gas)	Requires high pressure tanks (typically 350 to 700 bars). Tanks are much heavier than the actual fuel and are also a safety risk. If the pressure is reduced, tanks of large volume are required, which affect weight and drag and therefore aircraft performance. Could partially be stored in metallic structures, but practical application in aeronautics is rather limited so far.
Hydrogen (liquid)	Requires cryogenic tanks with insulation to keep the fuel at about $-250C^{\circ}$. Tanks are heavy and also require considerable volume with the drawbacks similar to gaseous hydrogen.
Battery	Requires casings with temperature control systems.
Fuel Cell	Requires liquid or gaseous fuel with all the aspects mentioned above. Additional infrastructure like air pumps, water supply or reformer devices is necessary.

Table 4.1: Characteristics of energy storage systems [Hepperle, 2012].

Other important point is the efficiency of each type of propulsion. The conversion of energy stored on-board to propulsive power involves several conversion steps. Each of them is affected by losses, which are expressed by individual efficiencies. For the comparison of different systems, the on-board conversion chain must be considered. For a complete picture one could extend this view to the complete energy chain from "well-to-wheel" in case of fossil fuel, but such an analysis is beyond the scope of this work and very difficult. Figure 4.8 shows four typical conversion chains [Hepperle, 2012]:

- conventional turboprop;
- conventional turbofan;
- battery powered system;
- fuel cell powered system.

Typical values for the efficiency of the individual components have been assumed. It is clearly visible that all electric systems exhibit high overall system efficiency. This is specially true for battery systems which avoid the conversion of fuel to electricity in the airplane offer the highest efficiency of more than 70%, compared with the efficiency of the classical combustion systems reaching efficiencies of only up

to 40%. Of course, these on-board chains do not contain the generation of electricity on the ground nor do they include the generation and distribution of fuel or electricity. For example the charging and discharging cycle of chemical batteries causes energy losses in the order of 15-20%. Nevertheless, in terms of efficient usage of on-board energy, the battery systems are very attractive.

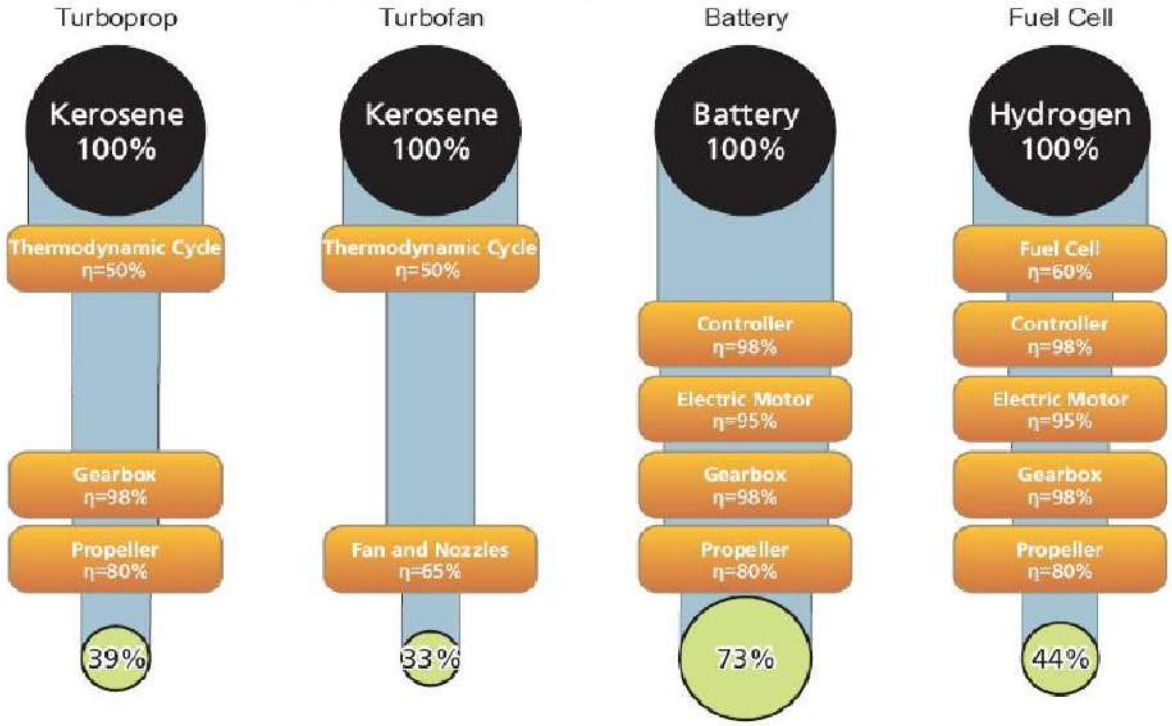

Figure 4.8: Typical on-board energy conversion chains with typical component and total efficiencies [Hepperle, 2012].

Another important aspect of the system is its mass.

In order to compare different electric power sources with a battery system, it is necessary to transform their parameters into an equivalent mass specific energy E^* of the complete system. First, the systems as electric power sources, that is, the chain up to the electric connector where the motor controller would be plugged in, are compared. Figure 4.9 relates the stored energy to the mass of the electric power source [Hepperle, 2012]. The example assumes identical flight performance of a general aviation airplane requiring a propulsive power of 50 kW for fast cruise. The required energy is determined from the respective efficiency chains so that 100 kWh are available for the mission. As the airplane has not been adapted to the mass of the propulsion system, this yields an optimistic view for the heavier systems. The mass given below the fuel tanks are for the fuel and the additional mass of the tank with its fuel systems. It can be seen that a high pressure tank for hydrogen outweighs the fuel mass almost by a factor of 20.

In Fig. 4.10 [Hepperle, 2012], the motor controller and the electric motor are added so that the chain extends up to the propeller shaft. This allows comparing the chain with an internal combustion engine. The results show that the classical internal combustion engine offers the lowest mass and hence an effective specific energy of almost 1600 Wh/kg, which is about 14% of the specific energy content of the raw kerosene fuel. This propulsion system is followed by the hybrid electric system which adds a

generator and an electric motor to the drive train.

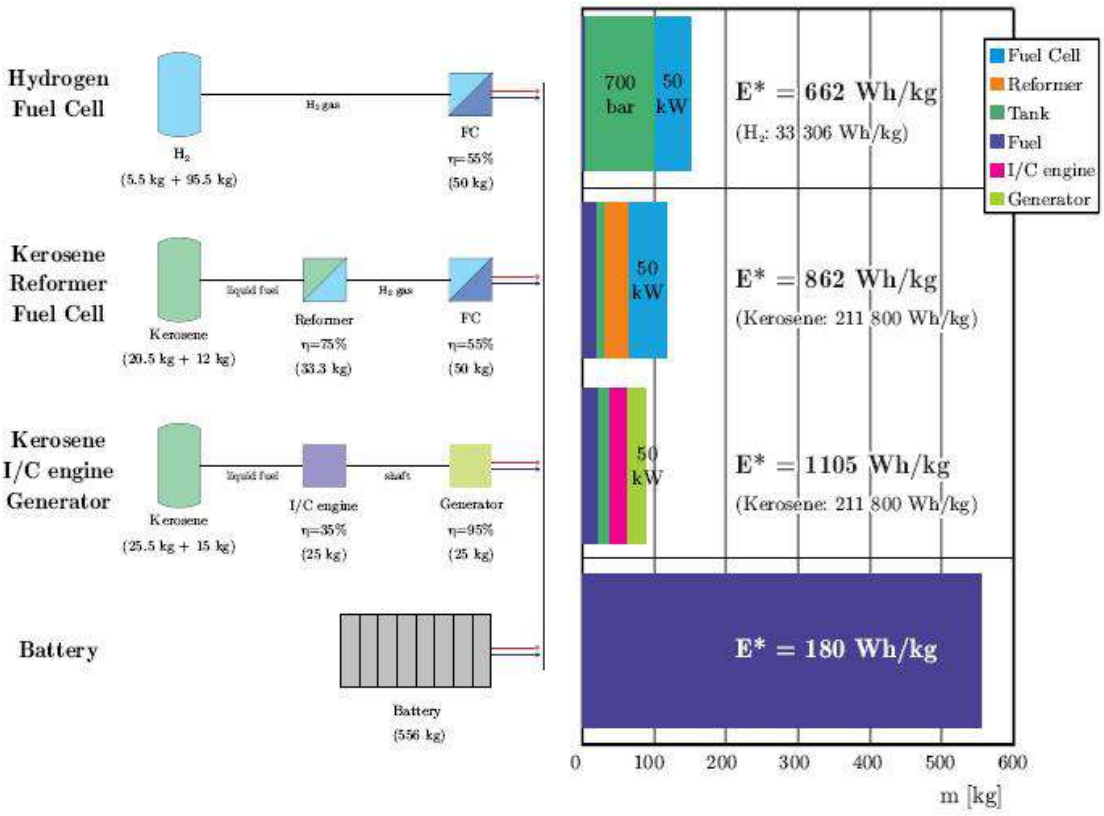

Figure 4.9: Mass and equivalent energy density of electric power generation systems delivering an electric power of 50 kW for 2 hours [Hepperle, 2012].

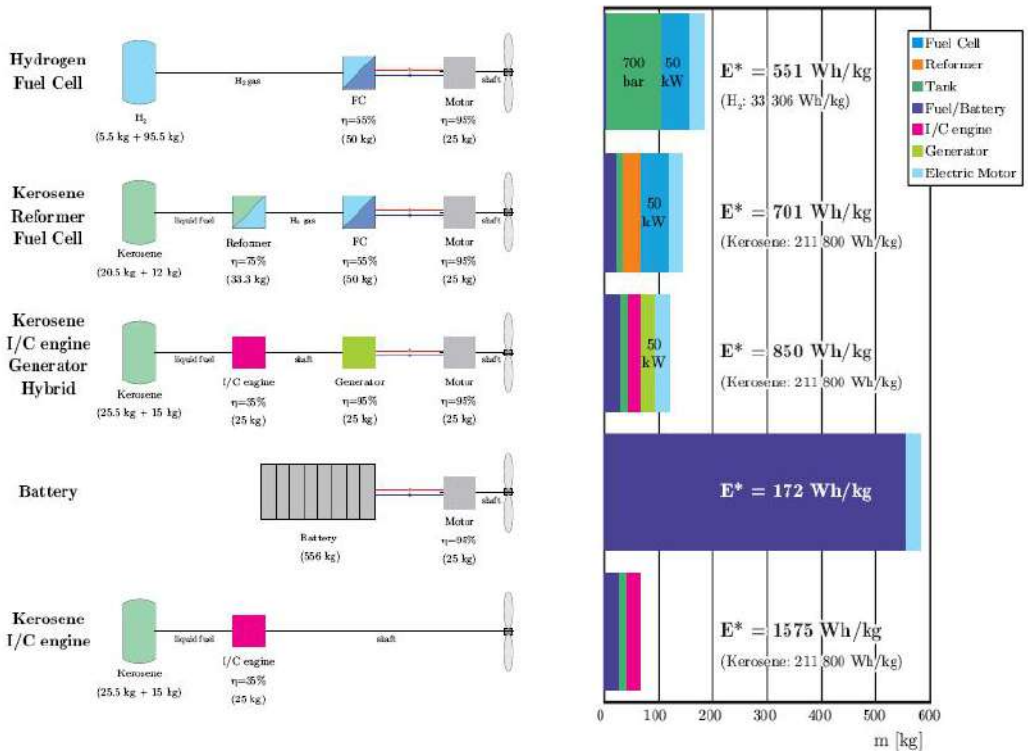

Figure 4.10: Mass and equivalent energy density of propulsion systems providing a shaft power of 50 kW for 2 hours [Hepperle, 2012].

Chapter 5

Solar Radiation Model

This chapter contains information about the solar radiation profiles. The radiation of the Sun is different in every part of the planet and this changes over the day, that is, the radiation is variable with time and, therefore, there exist maximums and minimums on the same day. For a specific mission located in a particular place, these parameters must be known to characterize how the solar panels work in terms of the time and type of mission.

5.1 Solar Irradiance

During the day, the propulsion energy of an electric UAV can be obtained by batteries, solar panels or a combination of both (Hybrid). The batteries can operate in any part or region of the world because they are independent of solar radiation. It is only necessary to consider the range to estimate the energy necessary to accomplish the mission. In contrast, in cases that have solar cells, it is necessary to define the mission in a particular place to know the parameters of solar radiation.

The energy coming from the sun depends on the wavelength, leading to the solar spectrum represented in Fig. 5.1 [PV-EDUCATION, 2013].

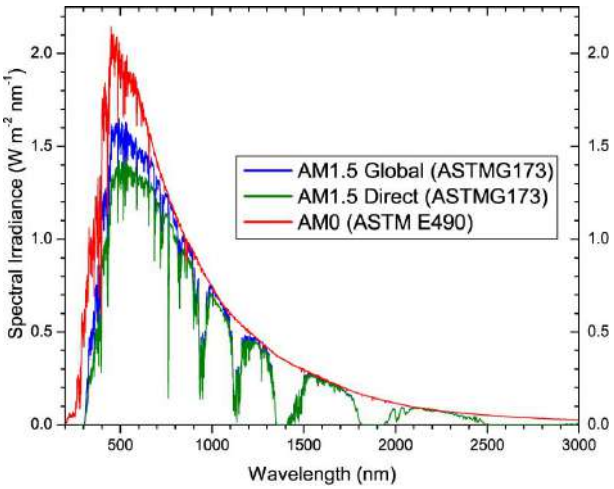

Figure 5.1: Solar radiation spectrum [PV-EDUCATION, 2013].

The standard spectrum for space applications is referred to as AM0. It has an integrated power of 1366.1 W/m^2. Two standards are defined for terrestrial use: the AM1.5 Global spectrum is designed for flat plate modules and has an integrated power of 1000 W/m^2 (100 mW/cm^2); and the AM1.5 Direct ($+$circumsolar) spectrum, defined for solar concentrator work, which includes the direct beam from the sun plus the circumsolar component in a disk 2.5 degrees around the sun. The direct plus circumsolar spectrum has an integrated power density of 900 W/m^2.

The SMARTS (Simple Model of the Atmospheric Radiative Transfer of Sunshine) program is used to generate the standard spectra and can also be used to generate other spectra as required [PV-EDUCATION, 2013, Gueymard, 1995].

An ideal (perfect) solar cell that would cover the entire spectrum and convert all this energy into electricity would have an efficiency of 100 %. In reality, depending on the semiconductors used, only a part of this spectrum is covered. The ratio of converted energy to the received radiation energy define the efficiency of a photovoltaic cell:

$$\eta_{PV} = \frac{E_{Converted}}{E_{Received}} \tag{5.1}$$

The solar irradiance intercepted by the earth at the top of the atmosphere, the solar constant, is quite stable with an observed value of 1365 W/m^2 $\pm$ 0.3%. However, on average, only about half of this energy reaches the surface and is available to drive surface and biological processes. Of the other half, approximately 30% is reflected back to space, and the remaining 20% is absorbed by clouds, dust, and "greenhouse" gases such as water vapor, carbon dioxide, and ozone [NOAA, 2013].

Solar radiation reaching the surface is made up of two components, direct and diffuse. Direct radiation is that which travels unimpeded through space and the atmosphere to the surface; and diffuse radiation is that scattered by atmospheric constituents such as molecules, aerosols, and clouds. In simple terms, direct radiation causes shadows, and diffuse is responsible for sky light. On a tilted plane, there is another irradiance component, the reflected ,which is the component reflected from the ground. The average ground reflection is about 20% of the global irradiance. Reflected irradiance is dependent on the albedo, which is a measure of the reflectivity of the Earth's surface. Fresh snow has an albedo of around 80 %, desert sand 40% and grass between 5% and 30 % [Quaschning, 2003]. The sum of the direct and diffuse components reaching a horizontal surface is global radiation.

For a better understanding, a schematic of these three irradiance components is shown in Fig. 5.2.

5.2 Daily Solar Energy

The irradiance depends on a lot of variables such as geographic location, time, plane orientation, weather conditions and albedo (or reflection coefficient of the surface) that represents the reflection on the ground surface. A good model was developed based on Appendix A [JRC-PVGIS, 2013]. This model, implemented in the *r.sun* software, can calculate the daily radiation profile for our mission aircraft given the following input data:

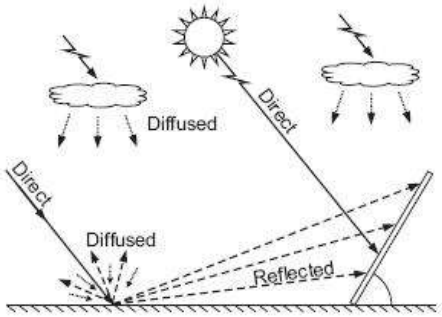

Figure 5.2: Irradiance components: direct, diffuse and reflected [Noth, 2008a].

1. Geographic location

   Selection of the geographical area where the mission takes place. The city of Covilhã (Portugal) is the location selected for the solar UAV primary mission.

2. Time

   Selection of the time of radiation and averaging period (annual or monthly). Since the mission is interest to take place over a single daylight period, average daily iradiation profiles in different months are used.

3. Plane orientation

   Selection of the orientation of the plane with respect to the incident solar irradiance. For this study, horizontal solar panels are considered, so the tilt and orientation of the panels is always 0º.

The output data obtained are the various components of irradiation, included in Appendix A. Using this data table, it is possible to create a graphic of the daily irradiance as shown in the Fig. 5.3. In the graph, two characteristic parameters can be obtained: maximum daily irradiation (I_{max}) and daily irradiation time (T_{day}).

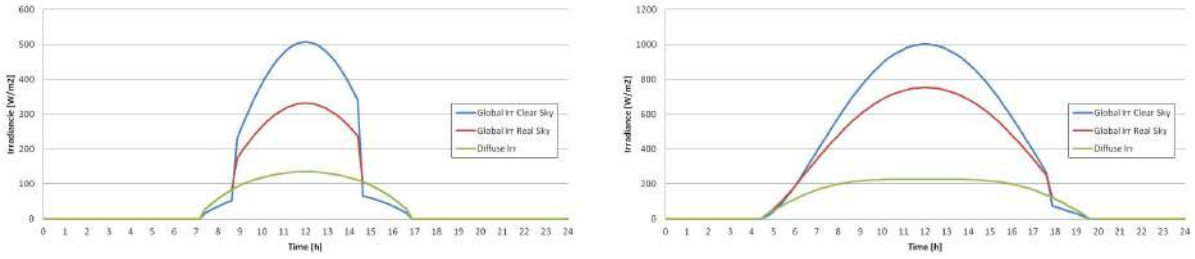

(a) January. (b) June.

Figure 5.3: Daily irradiance (monthly average).

As mentioned before, the two parameters $Imax$ and $Tday$ depend on the location and date. Figure 5.4 shows the evolution of these parameters throughout the year for Covilhã, Portugal.

It can be observed that, the duration of the day but also the maximum irradiance decrease in winter due to the very low sun elevation. For these reasons, it is easier to achieve 24 hours continuous flight in

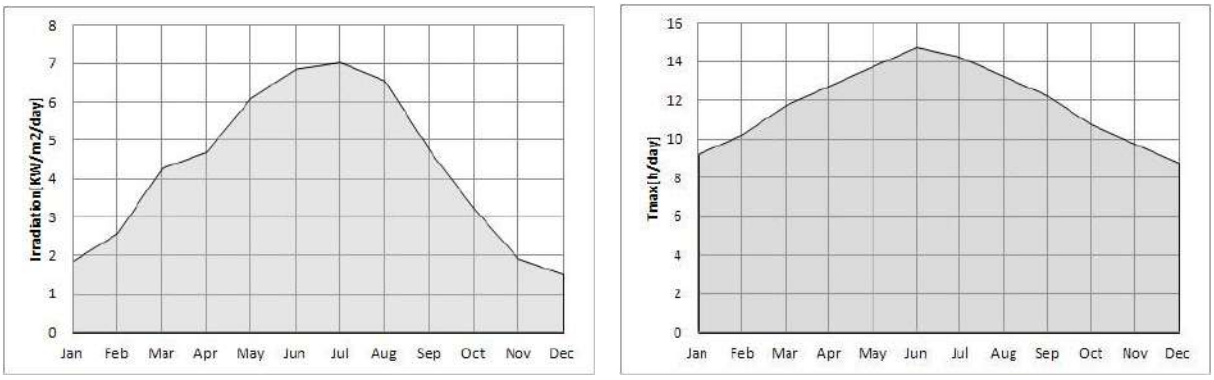

(a) Maximum daily irradiation.

(b) Daily irradiation time.

Figure 5.4: Evolution of the irradiation characteristic parameters throughout a year in Covilhã, Portugal.

summer than in winter in Europe when daytime lasts longer then night time. Concerning the influence of the location on Earth, the sun elevation becomes more favorable near the equator, but then the night and day duration are equivalent. Going in the opposite direction, at higher latitude in the North, one can take benefit of the sun the entire 24 hours, but the elevation being very low, the maximum power is also reduced.

Night Flight

At night, the only possibility of propulsion, due to non-existent solar irradiance and without considered conventional propulsion types, is by using batteries. Considering all the important technological advances in this area, using a battery with the optimum conditions in terms of specific energy, efficiency and durability, will provide the best features for a long range mission. For this reason, this matter is discussed in detail in sections 6.3 and 7.1.

Chapter 6

Architecture of the Propulsion System for Solar UAV

The basic concepts about solar powered aircraft and related technologies are briefly explain in this chapter. The different components of the solar powered system have a particular architecture, such as the one shown in Fig. 6.1. Each of these components is described in the following sections.

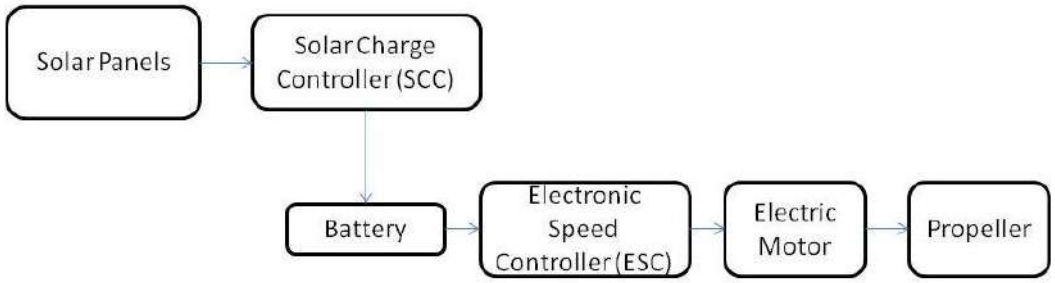

Figure 6.1: Scheme of the architecture of the propulsion system.

6.1 Solar Panels

A solar panel (also known as module, photovoltaic module or photovoltaic panel) is a packaged, connected assembly of photovoltaic (PV) cells. The solar panel can be used as a component of a larger photovoltaic system to generate and supply electricity in specific applications. Because a single solar panel can produce only a limited amount of power, most installations contain multiple panels.

PV modules are usually made from arrays of crystalline silicon solar cells. These cells are made of extremely thin silicon wafers (about 300 μm) and hence are extremely fragile. To protect the cells from damage, an arrays of cells is hermetically sealed between a layer of toughened glass and layers of ethyl vinyl acetate (EVA). An insulating tedlar sheet is placed beneath the EVA layers to give further protection

to the cell array. A sample of a single encapsulated PV cell is shown in Fig. 6.2.

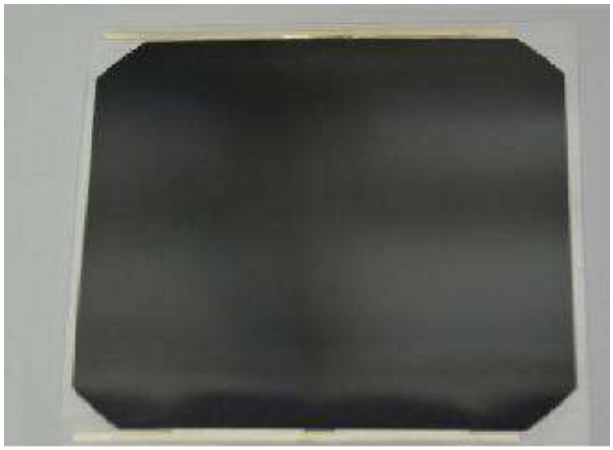

Figure 6.2: SunPower C60 cell (individually encapsulated).

An outer frame is sometimes attached to give strength to the module and to enable easy mounting on structures. A terminal box is attached to the back of a module; here, the two ends (positive and negative) of the solar string are welded or soldered to the terminals. This entire assembly constitutes a PV module. A sample PV module is shown in Fig. 6.3.

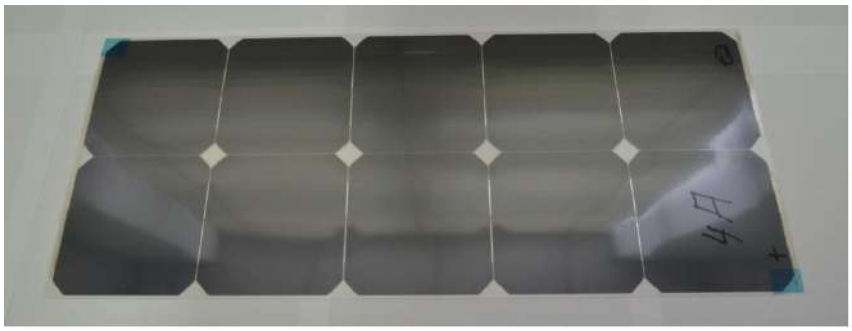

Figure 6.3: Solar panel using SunPower C60 cells in 2x5 array.

When the PV module is in use, the terminals are connected either directly to a load, or to another module to form an array. For large power applications, a PV array consisting of a number of modules connected in parallel and/or series is used. A photovoltaic system typically includes an array of solar panels, an inverter, and sometimes a battery and or solar tracker and interconnection wiring.

6.1.1 Standard Capacity/Ratings and Specifications

The wattage output of a PV module is rated in terms of peak watt (Wp) units. The peak watt output power from a module is defined as the maximum power output that the module can deliver under standard test conditions (STC). The STC conditions used in laboratory are:

- 1000 watts per square meter solar radiation intensity;
- Air-mass 1.5 reference spectral distribution;

- 25 °C ambient temperature.

PV modules of various capacities are available and are being used for a variety of applications. Theoretically, a PV module of any capacity (voltage and current) rating can be fabricated. However, the standard capacities available range from 5 Wp to 120 Wp. The voltage output of a PV module depends on the number of solar cells connected in series inside the module. The module provides a usable direct current (DC) , which is normally used to charge a 12-V battery.

6.1.2 Solar Cells

A solar cell or photovoltaic cell is a device that converts solar energy into electricity by the photovoltaic effect. It is very widely used in space application because it allows a clean and long-duration source of energy requiring almost no maintenance. Solar cells are composed of various semiconducting materials, constituting one or more layers. Silicon is very often used as it is the second most abundant element in Earth‘s crust and thus inexpensive. For this reason, this material will be considered in the further explanations that are also valid for other types of semiconductors.

Working Principles

In Fig. 6.4 , a simple silicon solar cell is represented with two doped semiconductors layers, p-type and n-type. When the sunlight strikes the solar cell surface the cell creates charge carriers as electrons and holes. The internal field produced by junction separates some of the positive charges (holes) from the negative charges (electrons). The holes are swept into the positive (or p-layer) and the electrons are swept into the negative (or n-layer). When a circuit is made, the free electrons have to pass through the load to recombine with the positive holes, thus producing current from the cells under illumination.

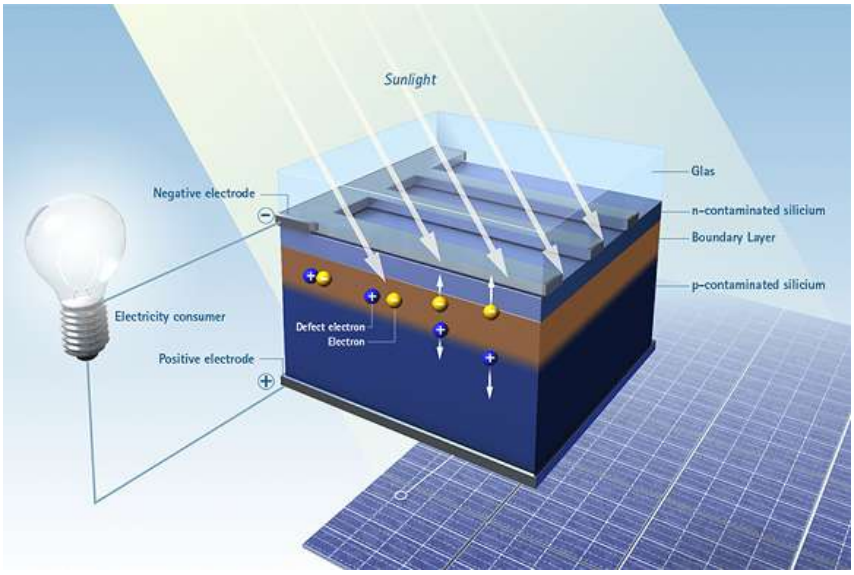

Figure 6.4: Working principle of a solar cell [MM, 2013].

6.1.3 Types of Solar Cells

There exist various types of photovoltaic cells that can be sorted according to the type of material, the fabrication process, substrate, etc.The most widely used type of material is silicon, because of its abundance and low cost. We can distinguish three types of silicon solar cells according to the type of crystal:

- Monocrystalline, for which absolutely pure semiconducting material is used which gives a high level of efficiency but at a high cost;
- Polycrystalline, composed of crystal structures of varying sizes. The manufacturing process is more cost efficient but leads to less efficient solar cells;
- Amorphous, or thin-layer cell, where a silicon film is deposited on glass or another substrate material, even flexible. The thickness of this layer is less than 1 μm, thus the production costs are very low, but the efficiency is poor as well.

However, other materials can be used as well like elements from groups three to five of the periodic table of the elements to produce compound solar cells. These include gallium arsenide, copper indium diselenide, cadmium telluride, etc. These cells are more expensive to produce, but lead to higher efficiency.

It should also be mentioned that the polymer solar cells, made of organic material, and the dye sensitized solar cells. Both are very promising technologies because they are inexpensive to fabricate. However, these technologies suffer from unstable efficiency problems that still must be solved and are not yet viable for industry.

6.1.4 Efficiency

The solar cell efficiency is the ratio of the electrical output of a solar cell to the incident energy in the form of sunlight as already expressed in equation 5.1. The energy conversion efficiency (η_{PV}) of a solar cell is the percentage of the solar energy to which the cell is exposed that is converted into electrical energy. This is calculated by dividing a cell's power output (in watts) at its maximum power point ($Pmax$) by the input light (I_{max}) and the surface area of the solar cell (A). As such, equation 5.1 can also be expresed as

$$\eta_{PV} = \frac{P_{PV}}{I_{max} \cdot S_{PV}} \,. \tag{6.1}$$

By convention, solar cell efficiencies are measured under standard test conditions (STC), unless stated otherwise, as defined in section 6.1.1.

There are many different kinds of solar cells and their features have many advantages and disadvantages. The efficiency that can be achieved is usually balanced by the complexity of the cell and, therefore, its cost. Figure 6.5 summarizes several different classes of solar cell showing how our experience in making the cells has led to improvements in efficiency over time.

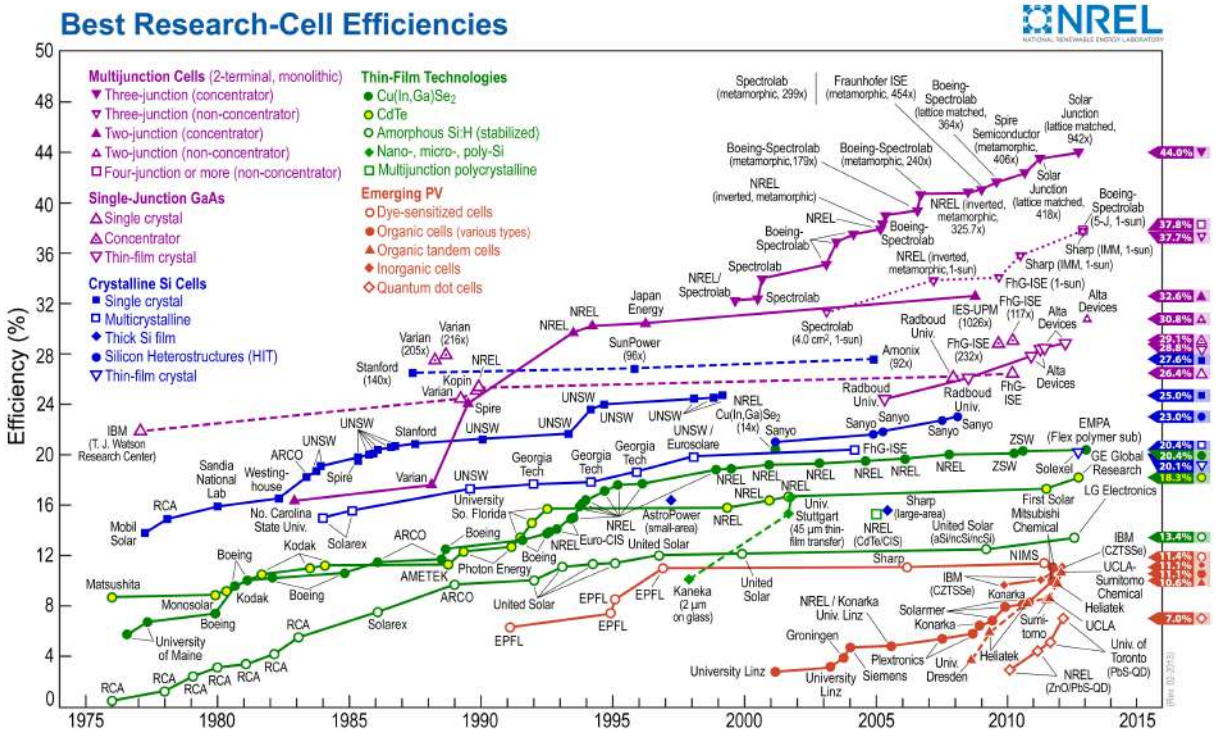

Figure 6.5: Evolution of solar cell efficiency by class type [NREL, 2013].

Four major classes can be identified in Fig. 6.5, being their main characteristics described next.

The purple line corresponds to multi-junction cells having a stack of semiconductor materials with band-gaps optimized to splitting the solar spectrum into segments and then absorbing the light preferentially into these three materials.

The blue lines correspond to silicon solar cells. These are based on large single crystals like those grown for integrated circuits (solid squares), or polycrystalline material, (open squares), or Si ribbon (solid diamonds). The higher crystal quality helps ensure higher efficiency and lower recombination or resistive loss.

The green lines correspond to a set of thin film cells with the Copper-Indium-Gallium-diSelenide (CIGS) cells having the best efficiencies found to date. Cadmium telluride (CdTe) cells are similar in performance, but with the CIGS it is possible to tune the composition and arrive at an optimum band gap value and increase the efficiency. The CIGS and CdTe cells are usually heterojunction solar cells based on a p-n junction made with two compositions of semiconductor – one of the semiconductors is the primary absorber – the other acts as a window but provides the electrical contacting required to achieved good current and voltage values. Most of these cells are fabricated by large area Chemical Vapor Deposition (CVD) or plasma deposition techniques.

The red lines are areas where much research and progress is on-going to improve the efficiency. The open circles are for dye-sensitized solar cells (DSC or DSSC – both abbreviations are used). DSSC's use dye molecules as the main light-absorbing medium. A class of nanostructure materials are able to host the dye molecules and allow for the photo-excited electrons to be donated to the structure and

yield reasonable efficiency. The pioneer for this work has been Michael Grätzel at École Polytechnique Fédérale de Lausanne (EPFL) in Switzerland [EPFL, 2013]. As a result these cells are often called "Grätzel cells".

6.1.5 Current and Voltage of a Solar Cell

The current to voltage curve of a solar cell has a very characteristic shape and can be described by the mathematical models of an ideal or real photovoltaic generator. As depicted in Fig. 6.6 , when the cell pads are not connected, no current is produced and the voltage equals to V_{OC}, the open circuit voltage. When it is short circuited, the voltage is zero but the current equals to I_{SC}. In between these two points where in both cases the power retrieved is zero, there is a working point, called the maximum power point, where the power one can retrieve is the highest and equals to

$$P_{max} = V_{MPP} \cdot I_{MPP} \,. \tag{6.2}$$

It is precisely at this point that the cells should be used and the ratio between $Pmax$ and the light intensity represents precisely the efficiency of the solar cell. However, the curve, and thus this point, is not fixed and varies depending on many parameters.

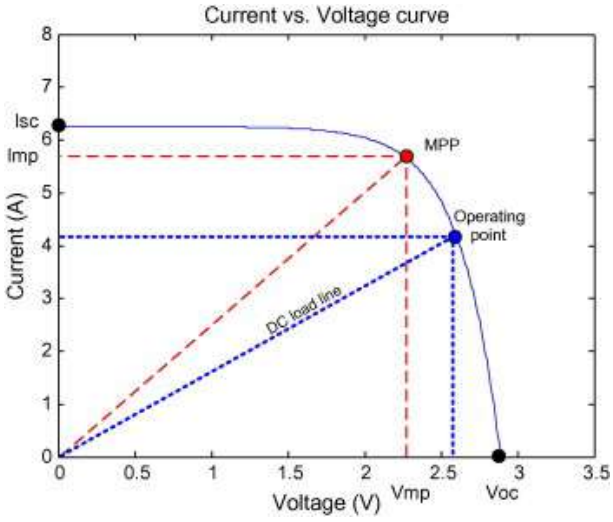

Figure 6.6: I-V characteristic of a solar cell [Karamia et al., 2012].

The current of a solar cell is proportional to its area and varies almost linearly with the light intensity (Fig. 6.7(a) and 6.7(b)). The voltage varies only a little bit when the light intensity changes and is independent of the cell surface, but depends on the semiconductor material. The important values of V_{OC}, I_{SC}, V_{MPP} and I_{MPP} are given in solar cells datasheets under standard spectrum conditions, either AM0 or AM1.5.

Temperature also affects the characteristics of solar cells. When it increases, the voltage decreases slightly whereas the current increases insignificantly. Globally, the power that a solar cell can give is higher for lower temperature, considering the same irradiance conditions (Fig. 6.7(c) and 6.7(d)). An assembly of solar cells connected electrically in parallel, which increases the current, or in series,

increasing then the voltage, is referred to as a solar module or solar panel. The I-V curve of a solar module has a scaled but similar shape to that of the single cell curve.

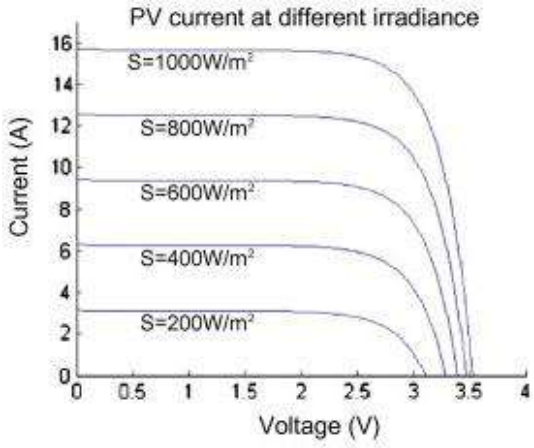

(a) Array current increases with irradiance.

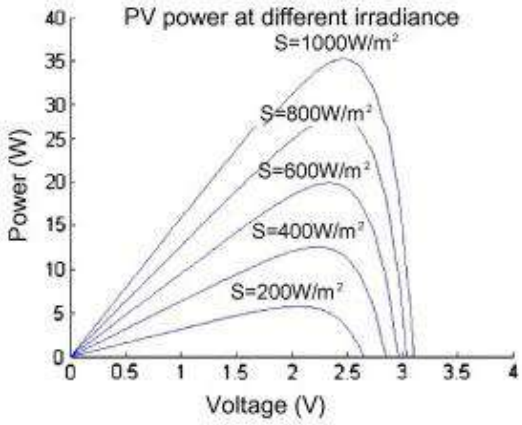

(b) Array power increases with irradiance.

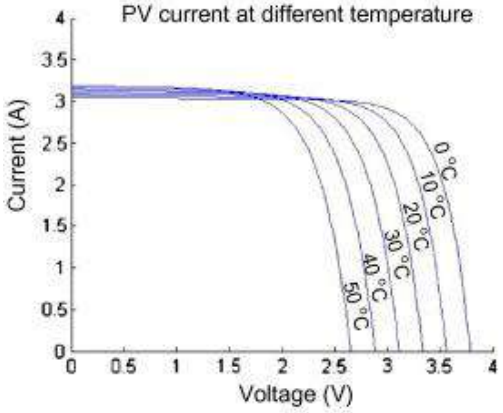

(c) Array voltage decreases as temperature increases.

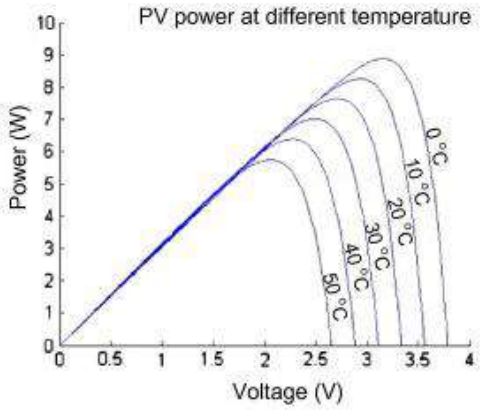

(d) Array power decreases as temperature increases.

Figure 6.7: Variation of current and power at different irradiances and temperatures [Karamia et al., 2012].

6.2 Solar Charge Controller

A charge controller, charge regulator or battery regulator limits the rate at which electric current is added to or drawn from electric batteries. It prevents overcharging and may prevent against overvoltage, which can reduce battery performance or lifespan, and may pose a safety risk. It may also prevent completely draining (”deep discharging”) a battery, or perform controlled discharges, depending on the battery technology, to protect battery life.

The terms ”charge controller” or ”charge regulator” may refer to either a stand-alone device, or to control circuitry integrated within a battery pack, battery-powered device, or battery recharger.

6.3 Batteries

The electrochemical batteries are energy storage devices which are able to convert chemically stored energy into electrical energy during discharging. They are composed of a cathode and an anode, made of two dissimilar metals, that are in contact with an electrolyte. When all elements are in contact with each other, a flow of electrons is produced. If the process is reversible so that they can be recharged, they are referred to as secondary batteries, in the other case they are primary batteries . Concerning a solar airplane, rechargeable batteries will of course be used.

6.3.1 Different Types

There are numerous types of rechargeable batteries. Of course, technology has evolved over the years and specific energy values continue to improve. Several technologies are available and, currently, the lithium-ion (Li-ion) or lithiumion- polymer (Li-Po) [Nazri and Pistoia, 2003] (where the electrolyte is a gel and not a liquid) technology is the best concerning gravimetric energy density, compared to lead-acid, nickel-cadmium (NiCd) or nickel-metal-hydride (NiMH). The nominal voltage of a lithium-polymer cell is 3.7V compared to 1.2V for NiCd and NiMH. Nowadays, most electric powered aircraft use battery systems of the Lithium-polymer type, producing a specific energy of about 200 Wh/Kg.

Type	Specific Energy(Wh/Kg)	Voltage (V)	Recharges	Charging time (h)	Self-discharge (% per month)
Lead	30-50	2	1000	8-16	5
Ni-Cd	48-80	1.25	500	10-14	30
Ni-Mh	60-120	1.25	1000	2-4	20
Li-Po	100-130	3.7	5000	1-1.5	10
Li-ion	110-160	3.16	4000	2-4	25

Table 6.1: Typical characteristics of batteries of different chemistry [BU, 2013, Vutetakis, 2001].

Table 6.1, there are several real examples of aeromodelling batteries. These are the values that will be used in the present work.

6.3.2 Charge and Discharge Process of a Lithium-polymer Battery

The charging process of lithium-polymer batteries is quite simple, but it has to be done very carefully because of safety reasons. During a first phase, a constant current charges the battery while the voltage increases, as depicted in Fig. 6.8. Once 3.7V is reached, the second phase starts, during which the voltage is kept constant while the current accepted by the cell slowly decreases. When this current is below 5% of the maximum current, the battery is charged.

The maximum charge rate, depending on the manufacturer, is always lower than 1 C, where C stands for the capacity of the battery. For instance considering a cell with a capacity of 800mAh, 1C represents a current of 800mA during one hour, 0.5C gives 400mA during 2 hours, etc. Concerning the charging voltage, it should never exceed 4.2 V. Using a charge rate higher than 1C or overcharging above the maximum voltage damages the cell and potentially results in explosion and/or fire. For this reason, lithium-polymer cells always need a minimum of one hour to be charged.

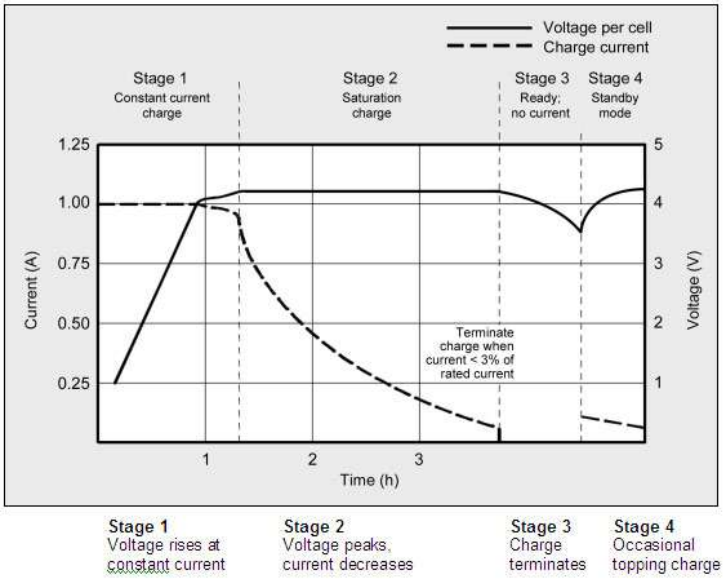

Figure 6.8: Charge process of a lithium-polymer battery [BU, 2013].

Concerning the discharge process, the maximum discharge current is specific to each model. Batteries with high discharge rates of around 20C are available, but the models that offer a high gravimetric energy density are always rated to less than 1C. At the end of the discharge, the voltage drops very fast below 3 V, as seen in Fig. 6.9. At that moment, the load has to be removed as soon as the voltage reaches approximately 2.7V per cell, or else the battery will subsequently no longer accept a full charge and may experience problems holding voltage under load.

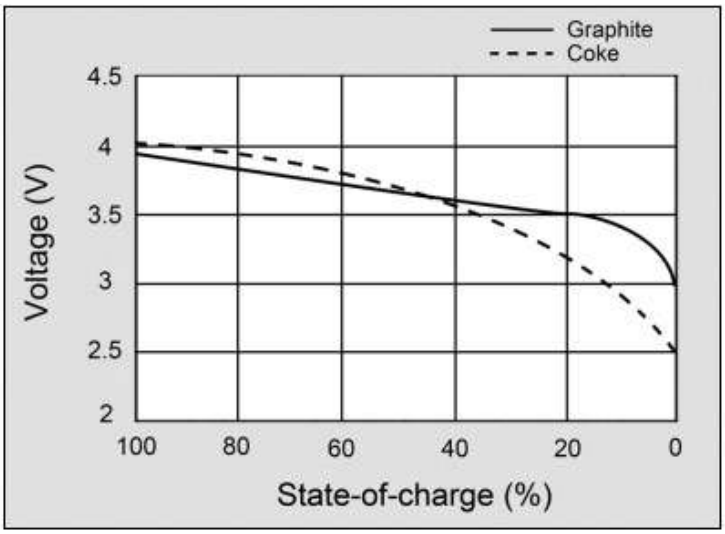

Figure 6.9: Discharge process of a lithium-polymer battery [BU, 2013].

Figure 6.9 illustrates the voltage discharge curve of a modern Li-Po with graphite anode and the early coke version.

6.4 Electronic Speed Controller

An electronic speed control(ESC) is an electronic circuit with the purpose to vary the speed of an electric motor, its direction and possibly also act as a dynamic brake. ESCs are often used on electrically powered radio controlled models, with the variety most often used for brushless motors essentially providing an electronically-generated three phase electric power low voltage source of energy for the motor.

ESCs designed for radio-control airplanes usually contain a few safety features. If the power coming from the battery is insufficient to continue running the electric motor, the ESC will reduce or cut-off power to the motor while allowing continued use of ailerons, rudder and elevator functions. This allows the pilot to retain control of the plane to glide or fly on low power to a safe landing.

6.5 Electric Motor

An electric motor uses electrical energy to produce mechanical work. This definition is very general and, in fact, there exists a very large variety of electric motors that coexist because of different supply sources, sizes, torques and speeds. The selection of a particular motor depends, obviously, on the application.

In the present case, DC (Direct Current or Continuous Current) motors will be used as they are designed to run on DC electric power supplied by a battery. By far, the most common types are the brushed and brushless types, which use mechanical and electronic commutation, respectively, to create a rotating magnetic field vector that pulls an electromagnet or a permanent magnet.

In a classic DC motor, the inner part is the rotor, which consists of a wound coil generating a rotating magnetic field, and the outer part is either an electromagnet or permanent magnet stator, which creates a fixed magnetic field. The electrical connection between the rotor and the external power supply are ensured by brushes. Thus these motors are called brushed in runners. Hence, the rotation will continuously change the coil polarity, thus generating an oscillating current. This current is at the origin of the rotating magnetic field and the turning moment. The limitations of DC motors are due to the need for brushes to press against the commutator what creates friction, sparks and electrical noise, especially as currents and speeds get higher. Also, the windings induce a high inertia to rotate and as they are placed in the center of the motor, they have trouble getting rid of the heat created by the eddy currents. To have high efficiency, a precision assembly and good components are required. Anyway, their speed control is easily achieved by varying the constant voltage or the duty cycle of a Pulse Width Modulated signal (PWM).

In a brushless DC motor, often abbreviated BLDC, the coils do not move. Instead, the permanent magnets rotate and the armature remains static. This gets around the problem of how to transfer current to a moving armature. In order to do this, the brush-system/commutator assembly is replaced by an electronic controller that performs the same power distribution found in a brushed DC motor. The drive electronics is more complex that for brushed motors because it has to activate the coils one phase after the other, that synchronized to the position of the rotor. To sense the position of the rotor, either Hall

Effect sensors or Back Electro Magnetic Force (BEMF) are used. When configured with the magnets on the outside, they are referred to as outrunner motors, else they are called inrunner. The advantages of BLDC motors are numerous : very precise speed control, high efficiency, high reliability, reduced noise, longer lifetime (no brush abrasion), no ionizing sparks. Additionally, they run much cooler than brushed motors, which allows the use of higher currents.

6.6 Propeller

The propeller is a device consisting of a set of two or more twisted, airfoil shaped blades mounted around a shaft and spun to provide propulsion of a vehicle through a fluid. It accelerates incoming air particles creating a reaction force called thrust. If one considers a stream tube around it, as the mass of air passing through the stream tube must be constant, the increased velocity leads to a contraction of the stream tube passing through the propeller disk, neglecting compressibility.

In order to better understand how it works, the Blade Element Theory (BET) [MDP, 2013] gives basic insight into the rotor performance as well as other characteristics. In this, theory the blade is assumed to be composed of numerous, infinitesimal strips with width 'dr' that are connected from tip to tip, as illustrated in Fig. 6.10. The lift and drag are estimated at the strip using the 2-D airfoil characteristics of the section. Also, the local flow characteristics are accounted for in terms of climb speed, inflow velocity, and angular velocity. The section lift and drag may be calculated and then integrated over the blade span.

Efficiency

The propeller efficiency η_P is defined as the ratio between the propeller thrust T times the propeller axial speed v and the resistance moment M_P times the rotational speed ω,

$$\eta_P = \frac{T \cdot v}{M_P \cdot \omega} \,. \tag{6.3}$$

Designing an efficient propeller presents the same challenges as for an airplane wing : find the best airfoil, chord and incidence angle that minimize the resistance torque and maximize the thrust for a given axial speed. This optimum varies along the blade, from hub to tip, due to the increasing radius and thus airspeed, which explains the twisting shape found on propellers. A good propeller designed for a specific flight domain should have an efficiency of at least 80%, 85% being an excellent value that is difficult to surpass. Unfortunately, it is not constant and varies with air speed and rotational speed, or more precisely with the dimensionless propeller advance ratio

$$J = \frac{v}{n \cdot d} \,, \tag{6.4}$$

where n is the number of blades and d their diameter (Fig. 6.11). As the propeller rotates through one circle the airplane advances a distance v/n. J is then the ratio of this value and the diameter.

For airplanes flying in changing conditions, in terms of speed and altitude for example, a variable pitch propeller can be used at the expense of weight.

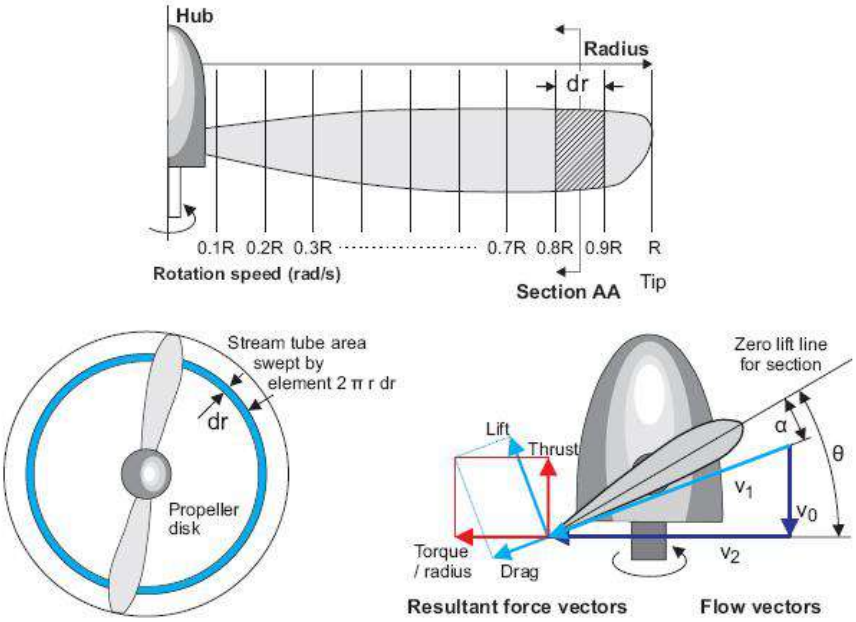

Figure 6.10: Concept of the blade element theory [MDP, 2013].

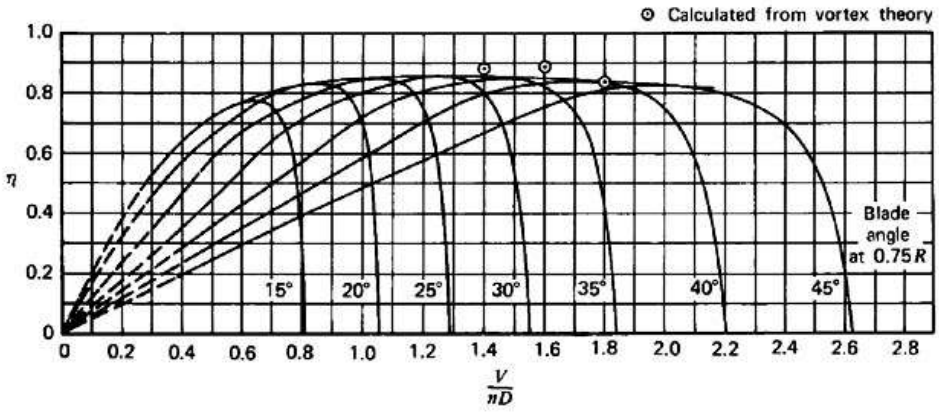

Figure 6.11: Typical propeller efficiency curves as a function of advance ratio and blade angle [McCormick, 1979].

Chapter 7

Design of the Electric Propulsion System for Solar UAV

The variation of solar radiation over time requires a detailed study to decide which of the electric propulsion methods will be appropriate for our mission. This factor will be key in the design of the propulsion system because it determines the final configuration of the system. There will be months in which the output power of the solar panels will be insufficient to ensure a flight, as established in the mission, due to low solar radiation levels. So this chapter includes the three possibilities of propulsion: batteries, solar panels or a hybrid selection of both. In each case, the type of technology needed is selected.

7.1 Battery Based Propulsion

Assuming that the aircraft flies only with energy stored in batteries, this first study is relatively simple. With the energy data calculated in section 3.3 and the different characteristics of batteries discussed in section 6.3.1,it is possible to create comparative graphs to estimate the required size of the battery. The calculation is simple because the energy required by the mission and the specific energies of the different types of batteries are known. With these data, the mass of the batteries, an extremely important factor for aircraft, can also be calculated.

Two safety factors will be considered:

1. The system consists of two separate batteries, one which stores energy for propulsion system and another which stores energy for flight systems (primary and secondary battery, respectively).

   The primary battery will have a capacity equal to the calculated energy in section 3.3, while the secondary battery capacity has been estimated by the specialists of the aircraft project to be 146.7 Wh as shown in Tab. 7.1.

2. An additional energy percentage will be considered in each battery.

   All fully charged battery is subject to the action of a slow and gradual self-discharge, which in other words is the fact that the battery voltage decreases and therefore the battery loses energy. The

Mission	Propulsion energy (Wh)	Systems energy (Wh)	Total energy (Wh)
Battery energy	482.4	146.7	629.1

Table 7.1: Total energy for the mission with batteries.

percentage of self-discharge depends on the type of battery, in this calculation was used 10%, that is the self-discharge percentage of the lithium batteries. According to this, that 10% is the percentage of additional energy.

The mass of each battery will be calculated as

$$m_{bat1} = \frac{E_{req}}{E^*_{bat}}\,, \tag{7.1}$$

$$m_{bat2} = \frac{E_{sys}}{E^*_{bat}}\,, \tag{7.2}$$

where E_{req} is the required propulsion energy, E_{sys} is the required energy for flight systems and E^*_{bat} is the mass specific energy of the battery. Calculating it for different types of batteries, one obtains Fig. 7.1.

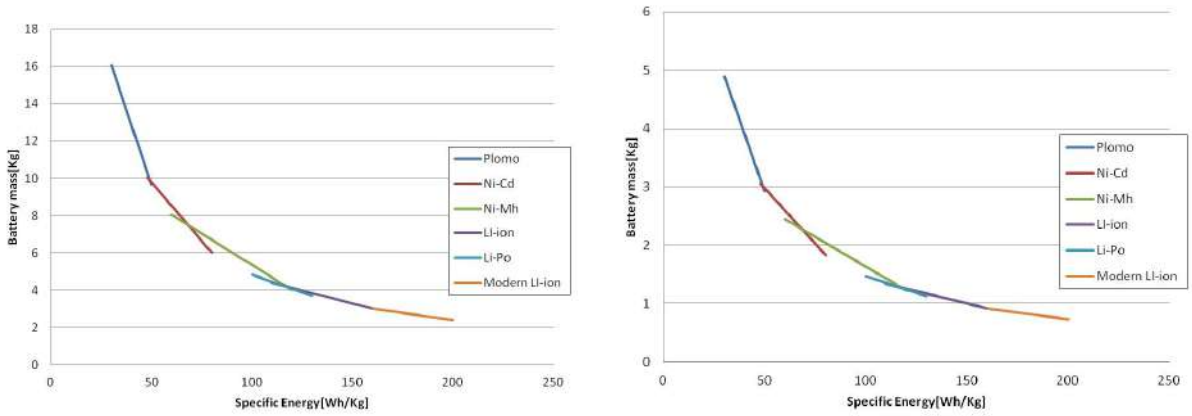

(a) Batteries for propulsion energy.

(b) Batteries for flight systems.

Figure 7.1: Battery types, mass and specific energy.

Figure 7.1 shows that with increasing mass specific energy, it is possible to reduce the mass of the batteries, a factor which is certainly beneficial. It is checked that Li-ion batteries have the best properties. Therefore, if the aircraft is only powered by lithium batteries to achieve our mission, the batteries should have the properties shown in Tab. 7.2. This configuration also enables night missions.

E^*_{bat} (Wh/Kg)	$m_{bat1}(Kg)$	$m_{bat2}(Kg)$	Total mass(Kg)
200	2.41	0.73	3.14

Table 7.2: Battery mass for mission with lithium battery only.

If one recalls the estimated total aircraft weight of 5 Kg from Tab. 3.1, it is clear that a battery only solution is not possible due to its excessive weight.

7.2 Solar Panel Based Propulsion

7.2.1 Selection of PV Cells

The PV cell selection is a key part of the study. The characteristics of different types of PV cells (section 6.1.3) will mark the criteria of selection. Specifically, mono-crystalline silicon PV cells will be installed due to their high efficiency level. There are PV cells with more efficiency than silicon but their price is excessively high, so eventually the mono-crystalline silicon is the best option. Besides price and efficiency, factors such as flexibility or weight will also be important factors of selection.

Recent research has developed very flexible PV cells but with low efficiencies. There are, however, semi-flexible cells with higher efficiency thus are still able to conform to the curved surfaces of the wing. Needless to say, low weight values improved the aircraft operating conditions. Basing on these selection criteria and considering that there are different manufacturers on the market. Some examples are shown in Tab. 7.3.

Company	PV Cell	η_{SC} (%)	Flex	Weight (g/m^2)	Dimensions (mm)
Gochermann Solar Technology	SunPower C60	22.6	Semi-flexible	950–1000	125 x 125
IXYS (IXOLAR)	KXOB22-12X1	22	Semi-flexible	2645	27 x 7
Bosch Solar Energy	M 3BB	18.43	No-flexible	1027	156 x 156
sunOWE	156 MM	18.2	No-flexible	1027	156 x 156

Table 7.3: Comparison of different mono-crystalline silicon PV cells [DR, 2013].

The selected PV cell is the SunPower C60 because it has the best characteristics for our aircraft. It has a high efficiency and also meets the requirements regarding flexibility and weight are designed for installation in the aircraft. Another plus is that the dimensions of these cells are adequate for small areas and will allow an orderly distribution on the wing.

7.2.2 Sizing of PV Arrays

In section 3.2, the available wing area (S_{PV}) was obtained considering certain correction factors. Using that value, the maximum number of PV cell (N_{SC}) can be calculated as

$$N_{SC} = Floor \cdot (\frac{S_{PV}}{S_{SC}}) \,, \tag{7.3}$$

where S_{SC} is the area of one PV cell.

Therefore, with the wing area available ($S_{PV} = 0.728m^2$) and the area of one PV cell ($S_{SC} = 0.016m^2$), will be possible install 44 PV cells, generating a set of 22 arrays per wing as shown Fig 7.2. The analytic study that follows takes this value as reference and the properties of the SunPower C60 cell.

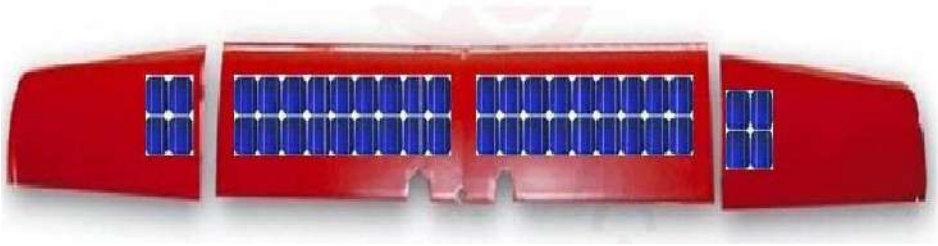

Figure 7.2: Scheme of the distribution of the solar panels on the wing.

7.2.3 Solar Panels Propulsion

Now it will be assumed that the aircraft flies only with the output power of solar panels. Knowing the solar radiation values, which were explained in section 5.2, it will be possible to determine the solar cells power considering their efficiency according with the equation 6.1.

This way, it is possible to determine the daily power profile for each month of the year. Figure 7.3 shows the typical profile in July, corresponding to the month when more power is generated.

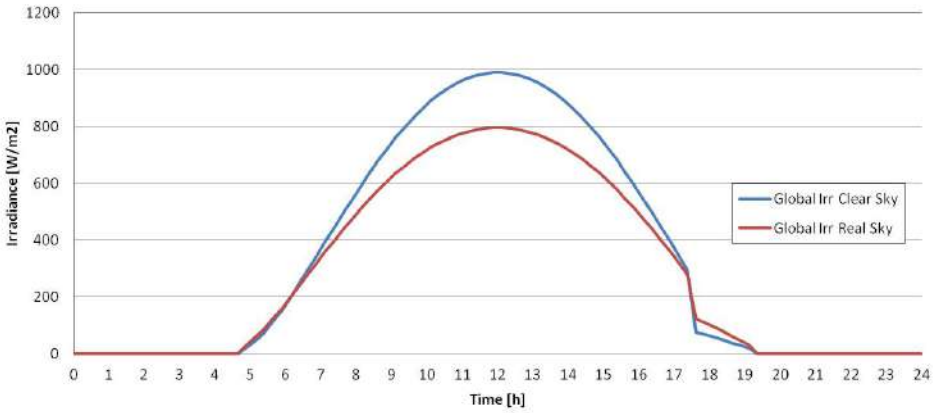

Figure 7.3: Daily power profile(July).

The mission time is known and, therefore, the power that can be obtained from this curve depends on the start time of the mission. Two factors were assumed to calculate the power of the solar panels:

1. The start time of the mission will be the hour of the day in which is the generated power value is greater than the minimum power required for take off.

2. The area under the curve of daily power is the energy provided by the solar panels and will be calculated by the method of trapezoids.

$$\int_a^b f(x)\,dx \approx (b-a)\cdot\frac{f(a)+f(b)}{2}\,. \tag{7.4}$$

Table 7.4 contains the energy generated by solar panels and shows the energy deficiency or excess energy, per day on a monthly average, compared with energy required by the mission.

An energy deficit means that one have not enough energy to carry out the mission, only with solar panels, this occurs in months with low irradiation (autumn and winter). While excess energy implies not

Month	Jan	Feb	Mar	Apr	May	Jun	Jul	Aug	Sept	Oct	Nov	Dec
Energy generated (Wh)	251.1	370.1	626.1	645.1	782.8	851.7	903.3	887.6	691.2	475.7	262.9	197.9
Defect/excess energy (Wh)	−378.0	−258.9	−2.8	15.9	153.7	223.6	274.2	258.4	62.1	−153.6	−366.1	−431.1

Table 7.4: Comparison of available solar energy on a monthly average to complete the UAV mission.

only that it is possible to achieve the mission but also there exist additional available energy, generally, for recharging the battery (spring and summer).

Although there are months in which the aircraft could fly only with solar panels, in energy terms, it is necessary to verify that these panels provide the power necessary to achieve the mission. The output power of the solar panels varies with time, as showed in Fig. 7.3, but the mission demand a particular power in each stage of the flight as shown in Fig. 7.4.

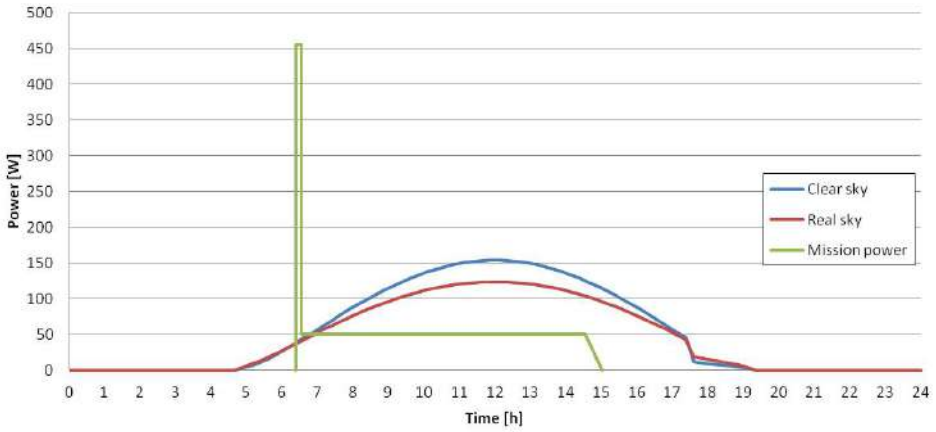

Figure 7.4: Power of the mission at every stage of the flight.

Figure 7.4 shows a power peak of 450 W at climb. When compared, in a same graphic, with Fig. 7.3 one can see that the output power of the panels has not at any time the value of power required for the mission. Looking at Appendix B one can see that this is true for all months. Then one can not achieve a mission with these features, due to the climb time. The solution is to opt for a hybrid propulsion.

7.3 Hybrid Battery and Solar Panels Based Propulsion

In section 7.2 it has been determined that is impossible to achieve the mission with the characteristics described in section 3.2 due to the power required for climb. So the proposed solution is to use a hybrid propulsion combining solar panels and batteries. The battery will be used primarily for climb which is the part of the mission where the aircraft can not reach the necessary power. Within the study, it is distinguished two different cases, corresponding to the excess energy months and months with energy deficiency. Also, in cases where there is excess energy, it is considered battery recharge in flight and its benefits explained.

7.3.1 Hybrid Propulsion with Excess Energy

This study was achieved with July irradiation values, because they are the highest in the year and, therefore, have more interest. The results can be extrapolated for all summer period, though in this case, the mission characteristics correspond to section 3.2. Representing the power distribution with solar panels over time and the distribution power for the mission, two different studies can be made. In Fig. 7.5 one can see areas with excess energy and the climb area where exist energy deficiency, therefore two options will be considered:the battery is not recharged in flight and the possibility of recharging the battery in flight.

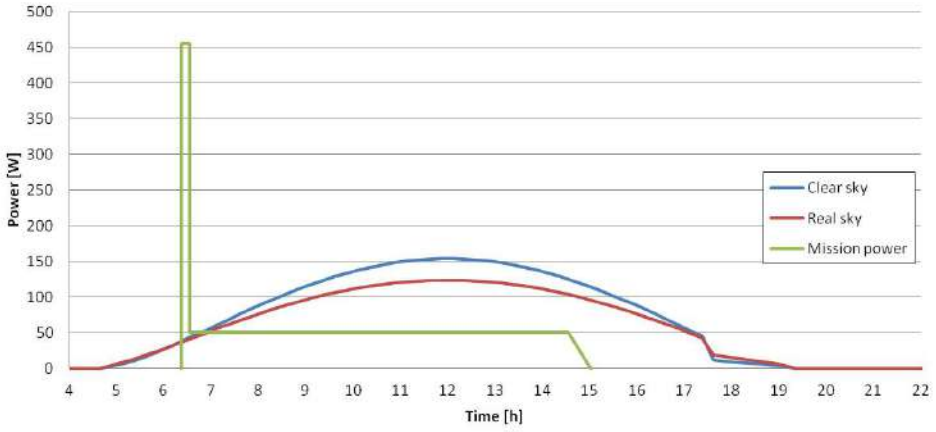

Figure 7.5: Power provided by the solar panels in July and power required by the mission.

Non-rechargeable battery in flight.

Figure 7.5 shows an area with negative energy (climb) and a large area of excess energy. In this study, the battery is not recharged in flight, so the mission start will need to have a battery with enough energy to satisfy the energy deficit on the climb. In cruise, the solar panels have excess energy to propel the aircraft , so the excess energy can be utilized in flight auxiliaries systems (adicional to Tab. 7.1), as propulsion power for additional payload or recharge the battery. In this case, one just has to add a battery that allows to realize the climbing maneuver, which has a power deficit.

The values obtained are shown in Tab. 7.5.

$E_{req_{cli}}$	$79.9Wh$
$E_{PV_{cli}}$	$21.7Wh$

Table 7.5: Energy required versus solar energy available for climb.

Being $E_{req_{cli}}$ the required energy for climb (calculated in section 3.3) and $E_{PV_{cli}}$ the generated energy with the solar panels at time instant of climb, calculated as

$$E_{PV_{cli}} = P_{PV_{cli}} \cdot t_{cli}\,, \tag{7.5}$$

where $P_{PV_{cli}}$ is the generated power by solar panels in climb.

Only by installing a battery with the capacity resulting from the subtraction between the two values calculated in the Tab. 7.5, will it be possible to realize the climb. As the climb stage is critical, for safety reasons, it should be installed a battery with the capacity to accomplish fully this stage, i.e. a battery with 79.9 Wh. Thus, having an extra margin of safety from the energy supplied by solar panels.

Rechargeable battery in flight.

In this case, the mission begins with a battery that must have a capacity at least equal to capacity calculated in Tab. 7.5 that permit the full climb. The excess energy seen in Fig. 7.5 , is now used to recharge the battery. The advantage of this is to have the battery (climb battery) charged ,for the next flight. The fact of recharge battery in flight allows new study possibilities:

- Changing the start time of the mission;
- Reducing the number of solar cells.

These two new studies try to check if the mission can be achieved with these new characteristics and, if so, in what conditions should the excess energy be used to recharge the batteries and how should they be subsequent used.

Changing the start time of the mission

Throughout the study, it was considered the beginning of the mission when the power provided by the solar panels allowed take off. Now, a new starting point will be chosen. This will be the time of day with maximum radiation, as shown in Fig. 7.6.

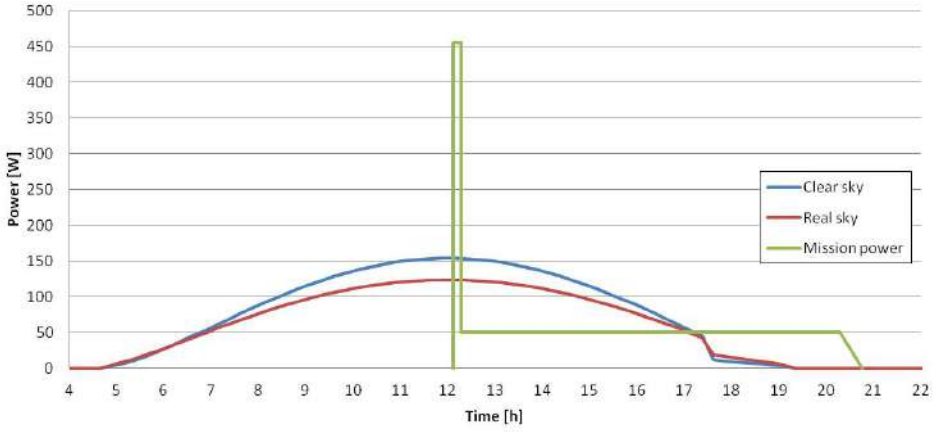

Figure 7.6: Power profile for new start time mission.

Figure 7.6 shows that in this configuration there exists a large area of energy deficiency at the end of the mission. Under these conditions, the energy produced by the solar panels will be $E_{SC} = 526.09Wh$. As it can be observed it is insufficient to carry out the mission with the specific characteristics at first

(original start time), ($E_{req} = 629.15$) . The solution is to put a battery with more energy and, depending on its storage capacity, it can have different configurations to recharge as Tab. 7.6 shows.

% Battery	0	10	20	30	40	50	60	70	80	90	100
% Solar Panels	100	90	80	70	60	50	40	30	30	10	0
Available energy for % Bat	0	62.61	125.22	187.84	250.45	313.07	375.68	438.29	500.91	563.52	626.14
Energy for % SP	626.14	563.52	500.91	438.29	375.68	313.07	250.45	187.84	125.22	62.61	0
Rechargeable Energy	Not pos	Not pos	25.18	87.79	150.41	213.02	275.63	338.25	400.86	463.48	526.09

Table 7.6: Trade-off of possible hybrid configurations and power available to recharge.

A study with different battery capacities according to a percentage of required total power by the mission was carried out, where the capacity of the battery will have a determinate value and the solar panel always provide an energy of 526.0 Wh but one part is for complete the propulsion energy (Energy for % SP) and the rest is for recharge. The two extreme cases, 0% battery and 100% battery, correspond to section 7.2 and section 7.1 respectively. Therefore, Tab. 7.6 shows, for different battery capacities, how much energy surplus exist to recharge the battery, considering that more battery capacity will imply that less power of solar panels will be required, and more energy will be available for recharge.

Reducing the number of solar cells

This study consist in determining how the generation of output power varies depending on the number of solar cells. In the summer months, there exist, a considerable excess power due to high levels of radiation, so it is possible to adjust these values for certain number of solar panels as shown in Fig. 7.7. This is calculated by varying the surface of the solar panels considering equation 6.1.

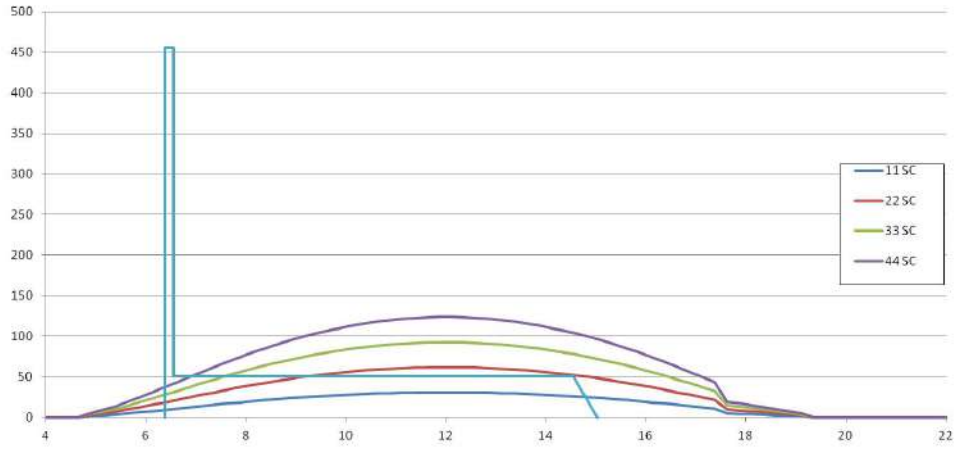

Figure 7.7: Power levels for different number of solar cells.

The mission could be achieved with only 31 solar cells and a battery for climb, being the energy produced by the other solar cells used to recharge the battery. Table 7.7 shows the possible energy for recharge the battery with each cell number configuration. Only values near to forty-four solar cells allow fully recharge the battery in case of being completely discharged in climb.

Nº SC	Energy production	Energy excess
31	636.48	10.34
32	657.01	30.87
36	739.14	113.00
40	821.27	195.13
44	903.39	277.29

Table 7.7: Excess energy in function of solar cells number.

7.3.2 Hybrid Propulsion with Deficiency Energy

This study was achieved with the lowest values radiation corresponding to winter, in particular, the month of December. The characteristics of the mission are as in 3.2 except the purpose, now is not fire detection missions but other purposes such as observation of roads after snowstorms.

The hybrid propulsion with energy deficiency is simpler than in the previous section. In this case, one has to correct the deficiency of battery total energy, peak power common to all months and the power deficit corresponding to the weaker radiation. The calculation is simple following Fig. 7.8 that is calculated with equation 6.1 and the December average irradiance profiles. Now the battery is not rechargeable in flight due to the low power of the solar panels.

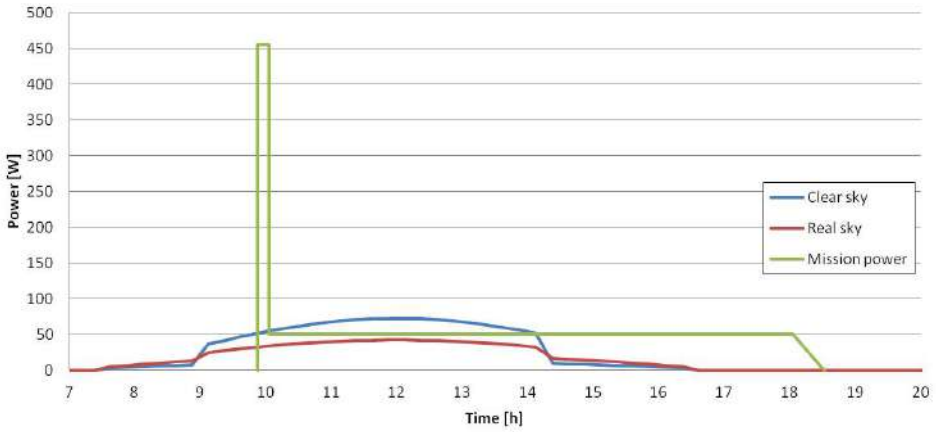

Figure 7.8: Power provided by the solar panels and power required by the mission in December.

It can be clearly seen in Fig. 7.8 the values of power and energy-deficient areas, then one can calculate the energy that the battery should provide so that the mission duration is achieved. The results are shown in Tab. 7.8, where E_{SC} is the value of generated energy, in December and E_{bat} will be the needed capacity to complete the mission.

E_{SC}	$198.0Wh$
E_{bat}	$431.2Wh$

Table 7.8: Energy required from battery and solar panels for a winter mission.

The main conclusions obtained to this study are:

1. Using batteries one could fly day or night independently. Mission range will depend on the type battery, high specific energy improve the Thrust/Weight ratio.

2. The flight only by solar panels is impossible due to power deficit in the climb stage. Therefore, a hybrid propulsion system is required.

3. Hybrid systems with excess energy and non-recharged battery in flight should have, as minimum, an installed battery with energy for climb.

4. Rechargeable batteries in flight for excess power systems can leave the batteries charged but with limitations. In most of the studies, it will be possible to charge the battery but limited by the energy excess and time. Generally in almost all cases, the battery (climb battery) would recharge completely.

5. Hybrid systems with energy deficiency should have an installed battery with enough energy to finish the mission, due to the low power output solar panels.

7.4 Final Configuration of the Electric Propulsion System

After studying the three possible forms of electric propulsion, a hybrid propulsion has been selected system as shown in Fig 7.9.

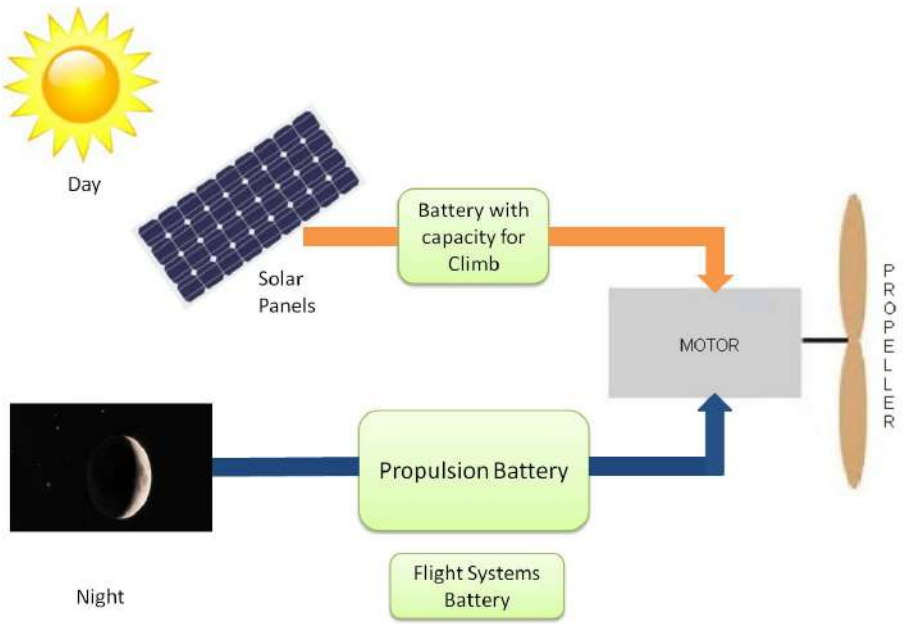

Figure 7.9: Scheme of the selected propulsion method.

The system consists of 44 solar cells, and a rechargeable battery with a capacity of 79.9 Wh. In these conditions, the solar UAV may only satisfy the mission requirements during the summer months and so the battery will recharge during flight theoretically, being recharging for the next operation. Night flight is outlined such as was described in section 7.1, that is, a pure battery powered system.

In this chapter, the energy inputs that should allow to carry out the mission were designed. The system output will be suitable when all components of the system are designed. So, the entire system has to be designed by selecting all intermediate electric elements. This will be done in the next chapter.

Chapter 8

Selection of the Hybrid Propulsion System Components

This chapter is closely related to Chapter 6 where the working principle of all component of the solar-powered system was described. Chapter 8 contains a selection of possible propulsion system components. For each components, the most appropriate reference will be selected according to the calculated requirements and their main characteristics will be presented. Another important part of this chapter is to describe the electrical coupling of all components to see under what conditions the system has to work.

8.1 Solar Cell Selection

The PV cell selection was discussed in 7.2.1. The solar panel will be made of SunPower C60 cells whose main characteristics are shown in Fig. 8.1 and Tab. 8.1.

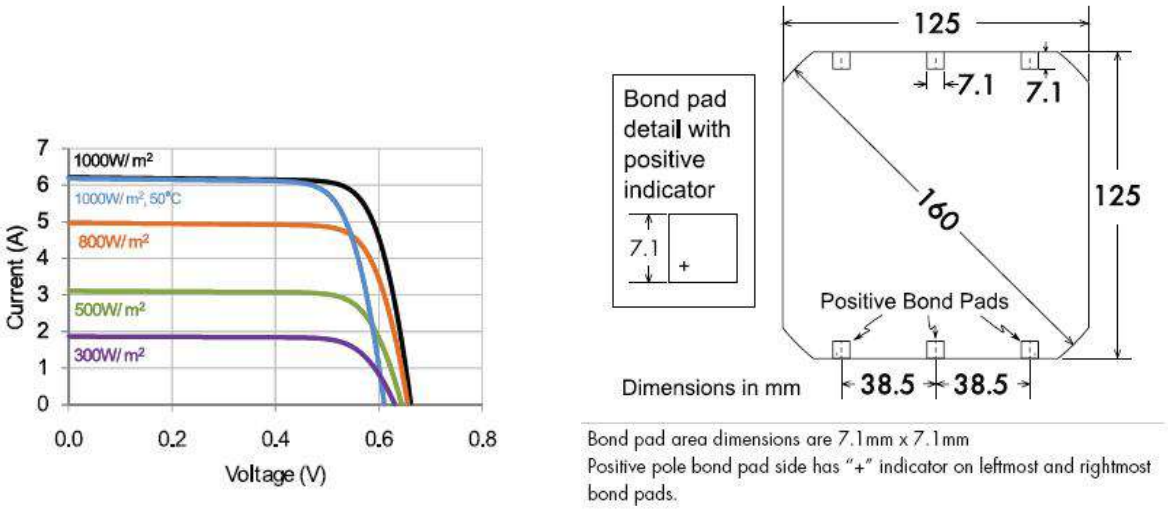

(a) Typical I-V curve.

(b) Cell and bond pad dimensions.

Figure 8.1: SunPower C60 properties [SunPower, 2013].

Solar Cell	P_{mpp} (Wp)	η_{SC} (%)	V_{mpp} (V)	I_{mpp} (A)	V_{OC} (V)	I_{SC} (A)
SunPower C60	3.43	22.6	0.583	5.94	0.689	6.29

Table 8.1: Electric characteristics of SunPower C60 at STC [SunPower, 2013].

The electric characteristics shown in Fig. 8.1 and in Tab. 8.1 are for a single C60 solar cell. It can be seen that a single solar cell produces about 0.5 volts (V_{mpp}) but the propulsion system will need at least a voltage of 12V, the typical working values of rechargeable batteries. To produce those 12 V, it is necessary to connect 22 cells in series as shown in Fig. 8.2.

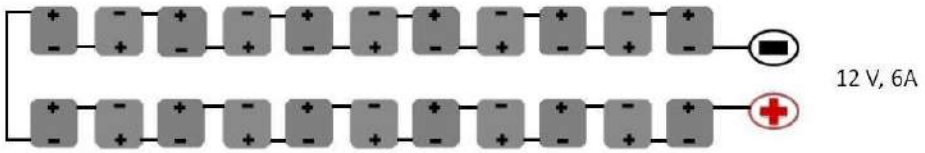

Figure 8.2: 22 PV cells connected in series in a 11x2 array.

Following the same reasoning, the current of the PV cells connected in series would be about 6A (I_{mpp}), so connecting in parallel another array of 22 PV cells, the current would increase to a value of approximately 12 A, as illustrated in Fig. 8.3.

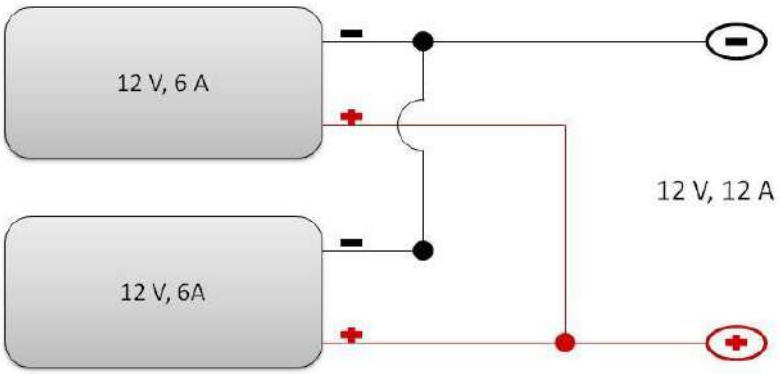

Figure 8.3: Solar arrays connected in parallel.

8.2 Solar Charge Controller Selection

Battery chargers used in solar systems come in all shapes, sizes, features, and price ranges. Important factors to consider include not requiring excessive power, small footprint, lightweight and low cost. Figure 8.4 shown the two most appropriate models of solar charge controllers (SCC) operating at 12 V for small systems.

1. Morningstar SunKeeper (12 Amp, 12 Volt);

2. Morningstar SunSaver (6 Amp, 12 Volt).

(a) Morningstar SunKeeper. (b) Morningstar SunSaver.

Figure 8.4: Solar charge controllers [Morningstar, 2013].

SCC	Solar Current (A)	Voltage (V)	Dimension (mm)	Weight (g)	Price ($)
Morningstar SunKeeper	12	12	99 x 51 x 13	110	66.30
Morningstar SunSaver	6-10	12	152 x 55 x 34	230	40.30

Table 8.2: SCC specifications [Morningstar, 2013].

Considering the factors shown in Tab. 8.2 the Morningstar SunKeeper SCC will be selected which, despite being more expensive, has better characteristics in terms of weight, size and working solar current.

Looking at Fig. 8.4(a), it looks it might be possible to save additional weight by removing the casing in the final installation. This will be tried during the UAV assembly.

8.3 Battery Selection

The battery selection depends solely of its capacity since the nominal voltage is fixed at 11.1 V corresponding to three Li-Po cells connected in series (3S). In this case, one is looking for batteries that allow a flight with hybrid propulsion with a minimum capacity of 58.1 Wh or 5239 mAh (value calculated in section 7.5 resulting from subtracting the energy needed for climb and the available energy in solar panels). The capacity required for additional safety is 7202 mAh. Figure 8.5 shows different batteries ordered from lowest to highest capacity corresponding to the following models:

1. Hyperion G3 CX - 3S 3300mAh (25C)(x2);
2. Hyperion G3 CX - 3S 4000mAh (25C)(x2);
3. Turnigy nano-tech - 3S 6400mah (40-80C);
4. Turnigy nano-tech - 3S 8400mah (40-80C).

(a) Hyperion G3 CX - 3300mAh.

(b) Hyperion G3 CX - 4000mAh.

(c) Turnigy nano-tech 6400mah.

(d) Turnigy nano-tech 8400mah.

Figure 8.5: Batteries with similar capacity [HK, 2013, Hyperion, 2013].

Battery	Capacity (mAh)	Voltage (V)	Constant Dis	Dimension (mm)	Weight (g)	Price ($)
Hyperion G3 CX	3300	11.1	25C	138 x 46 x 25	276	64.53
Hyperion G3 CX	4000	11.1	25C	138 x 42 x 29	306	76.45
Turnigy nano-tech	6400	11.1	40C / 80C Burst	137 x 41 x 44	506	58.97
Turnigy nano-tech	8400	11.1	40C / 80C Burst	157 x 45 x 45	641	81.38

Table 8.3: Battery specifications [HK, 2013, Hyperion, 2013].

The Hyperion batteries have less capacity that the required by the mission then it will be necessary install two batteries. Installing two batteries in parallel, it is possible to compare with high capacity batteries as shown Tab. 8.3.

Observing Tab. 8.3, all batteries are lithium-polymer type and in particular 3S, that is, three cells that provide 3.7 V each one, connected in series, resulting in a total voltage of 11.1 V. In this case and for additional safety the battery Turnigy nano-tech with 8400mAh of capacity will be selected. Furthermore, the weight difference with the other batteries is small, indicating that this battery has a very good energy density factor which helps to build a lightweight propulsion system.

8.4 Electronic Speed Controller Selection

For the ESC selection, one has to take into account the type of battery chemistry (always Li-Po) and an adequate current, without forgetting the compatibility with the type of electric motor. There are some ESC which detect the type of battery automatically, as well as the number of cells connected in series. In Fig. 8.6 and Tab. 8.4, it is shown four examples and corresponding specifications.

1. Hyperion ATLAS 45A Brushless ESC;
2. Hyperion ATLAS 60A Brushless ESC;
3. Turnigy Super Brain 60A Brushless ESC;
4. Turnigy AE-65A Brushless ESC.

ESC	Constant Current (A)	Battery	BEC(V/A)	Motor Type	Weight (g)	Size (mm)	Price($)
Hyperion ATLAS	45	2-4 S	5/4	Brushless	45	75.7x30.1x9.6	100.92
Hyperion ATLAS	60	2-4 S	6/4	Brushless	63	69.7x30.1x14	113.36
Turnigy Super Brain	60	2-6 S	5/4	Brushless	50	71x26.5x15	49.99
Turnigy AE-65A	65	2-6 S	5/4	Brushless	73	70x34x17	32.76

Table 8.4: Electronic speed controller specifications [HK, 2013, Hyperion, 2013].

Choosing a good ESC is not an easy task because it will depend the characteristics of the electric motor. The main factor one must consider is the maximum current. The appropriate ESC must be able to work with a higher current than the maximum current that the electric motor draws, so the selection of the electric motor and ESC are strictly linked.

Therefore, the critical factor that can make the system work well is an adequate current between these two components. Other factors like weight, dimensions and price for these component are similar and will not be decisive in the selection. This task will be carry out together with the electric motor selection.

8.5 Electric Motor Selection

The selection criteria for the electric motor will be those that allow to have the power needed in every stage of the mission and also take into account other factors such as weight and cost, without forget the link with the ESC. The maximum power occurs in the climb stage (450W), so the motor selected must be able to provide this power. The list below shows four different electric motors that are considered adequate.

1. NTM Prop Drive Series 35-36A 1400Kv;
2. Turnigy D3548/4 1100Kv;
3. Hyperion ZS 3020 8-Turn 1135Kv;

(a) Hyperion ATLAS 45A.

(b) Hyperion ATLAS 60A.

(c) Turnigy Super Brain.

(d) Turnigy AE-65A Brushless ESC.

Figure 8.6: Electronic speed controllers [HK, 2013, Hyperion, 2013].

4. Hyperion ZS 3025 10-Turn 775Kv.

Their pictures and main characteristics are shown in Fig. 8.7 and Tab. 8.5, respectively. The previous list is a selection of electric motors capable of providing the power required for the mission. This is a single factor but it limits the range of possible motors available on the market. Besides the power as a selection factor, two new considerations can be added: first, the motor maximum current must be adjusted to the current values of ESC seen in Tab. 8.5; the second is related with the propellers, each motor may use a different range and the power and thrust obtained depend of that.

E. Motor	Voltage (V)	rpm/V (Kv)	Max Current(A)	Weight (g)	Length (mm)	Diameter (mm)	Price($)
NTM Prop Drive Series	11.1	1400	55	117	38	35	18.36
Turnigy D3548/4	11.1	1100	50	159	64	48	19.83
Hyperion ZS3020-8	11.1	1135	70	162	43	38	109.99
Hyperion ZS3025-10	11.1	775	65	197	50	38	124.99

Table 8.5: Electric motor specifications [HK, 2013, Hyperion, 2013].

It is a great advantage that manufacturers of electric motors recommends to use a determinate propeller. Some manufacturers not only recommend a propeller, but also provide test data (Tab. 8.6). These data will be used only as an aid in the components selection and later it will be experimentally tested.

(a) NTM Prop Drive Series 35-36A.

(b) Turnigy D3548/4.

(c) Hyperion ZS3020-8.

(d) Hyperion ZS3025-10.

Figure 8.7: Electric motors [HK, 2013, Hyperion, 2013].

8.6 Propeller Selection

Typically, the propellers are identified by a set of two values in the form

$$d \times p\,, \tag{8.1}$$

where the first term (d) is the propeller diameter and the second (p) is the blade pitch. Therefore, diameter and pitch will be the global parameters that characterize the propellers. In Tab. 8.6, the recommended propellers that can be used with each electric motor to generate the required power are listed. Other cases exist so it will always be necessary to do some tests.

E. Motor	Propeller	Voltage (V)	Current (A)	Electric power (W)	Propulsive power (W)
NTM Prop Drive Series	APC 10x5 - 11x5.5	11.1	46 - 49	510 - 543	386 - 411
Turnigy D3548/4	APC 11x7	11.1	40	483	366
Hyperion ZS3020-8	APC 11x5.5E	11.1	49	545	412
Hyperion ZS3025-10	APC 15x8E	10	51	514	389

Table 8.6: Data propeller-electric motor manufacturer [HK, 2013, Hyperion, 2013].

The cost of the propellers is not very high, so it is possible to test different propellers in terms of diameter and pitch, using as reference the test data included in Tab. 8.6.

The data shown in Tab. 8.6 were tested with battery, ESC, motor and propeller, and contains the

voltage, currents and power for a particular propeller test. To estimate a propulsive power of reference for each motor, the study would be much more complicated.

The propulsive power can be calculated as

$$\eta_{prop} = \eta_E \cdot \eta_P = \frac{P_{Propulsive}}{P_{Electric}}\,, \tag{8.2}$$

then

$$P_{Propulsive} = \eta_E \cdot \eta_P \cdot P_{Electric}\,. \tag{8.3}$$

The calculation is not so simple because the efficiency of the propeller depends on many factors, such as: speed, thrust, rpm and advance ratio, and the combination of these values will only be achieved through an experimental test as shown Fig. 8.8. The APC propellers manufacturer provides test data for the mentioned propellers where it can be observed typical values for each propeller [APC, 2013].

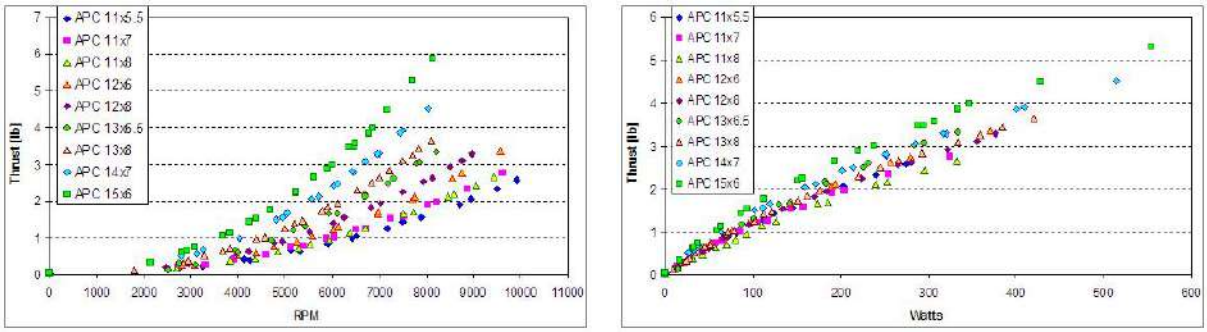

(a) Experimental test values of thrust-rpm.

(b) Experimental test values of thrust-power.

Figure 8.8: Experimental tests for different models of APC propellers [APC, 2013].

The propulsive power will be estimated with the theoretical values of efficiency for this two components, propeller and motor, $\eta_E = 89\%$ and $\eta_{Plr} = 85\%$ respectively. The value obtained in each case has to ensure the necessary power for climb ($P_{Propulsive} \geq 450W$). This estimate is only valid for a possible selection but actually the exact values will have to be obtained from an experimental test.

As seen in the Tab. 8.6 there are values near 450 W , it serves as a first reference for pre-selecting one or the other but consider that the component will be selected and then necessarily it will be tested.

8.7 Final Configuration of the Propulsion System Components

At this point, by looking at tables 8.4, 8.5 and 8.6 the selection of the combo ESC-Motor-Propeller can be made. The selected components are a speed controller Turnigy Super Brain, a electric motor NTM Prop Drive Series and a APC 11x5.5 propeller. Electrical connection characteristics of the battery, ESC and electric motor are suitable. Acording to the criteria established in the previous tables also have been important factors to selecting the weight and cost. The selected ESC is light compared to the other three, only Hyperion Atlas 45A have less weight but its price is very high. The electric motor is chosen based on the lowest weight and also price, which also coincides with the best value of provide power.

Finally the selection of the propeller is in accordance with the recommendations of the manufacturer since in this case the cost price is similar in all models. This component could be replaced if the test results are not appropriate to achieve the required power but, it will be checked with experimental test. The scheme of the selected components is illustrated in Fig. 8.9.

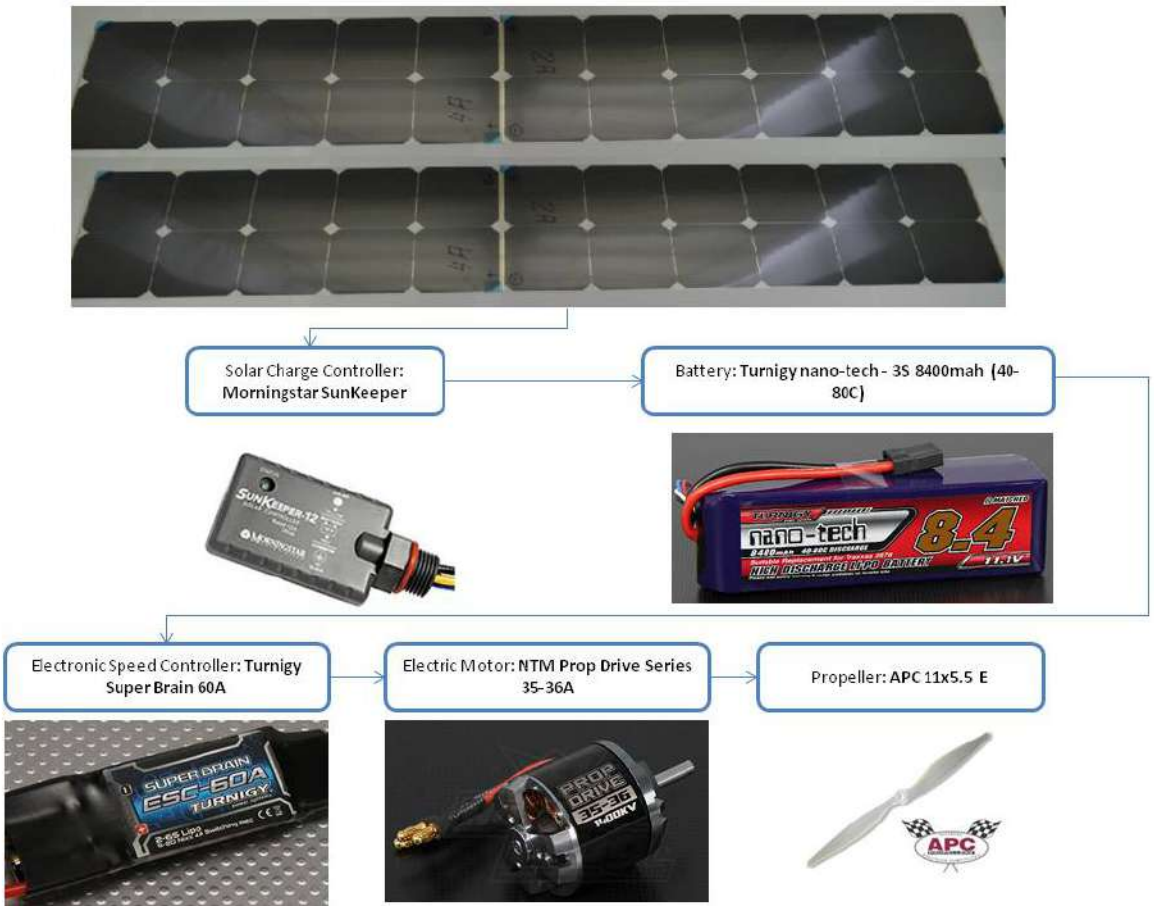

Figure 8.9: Scheme of the propulsion system components selected.

Chapter 9

Experimental Test of Propulsion System and Subsystems

In this chapter, a road-map for the different experimental tests of the designed system will be proposed. Not only are described some of the possible tests but also it will be facilitated the work in the near future when the propulsion system will be actually assembled and tested. The chapter begins with testing of individual cells, different combinations of arrays, intermediate subsystems and finally, the experimental test of the complete propulsion system.

9.1 Experimental Test of the Solar Panels

It is necessary to test the solar panels to ensure that the solar cells are providing values near the nominal voltage and current. It will be possible to experiment with different array configurations and at different times of the day to see how these values evolve. Also, this type of test will help to detect possible errors of operating for deterioration or an inadequate manufacture of the solar panels.

9.1.1 Solar Cells

The first test will be to characterize a single PV cell as shown in Fig. 9.1. With a multimeter, the voltage and current values will be measured and compared with the nominal values. This procedure may be repeated a few times to characterize the behavior of different cells. This data will help to form arrays optimally, where the cells are matched.

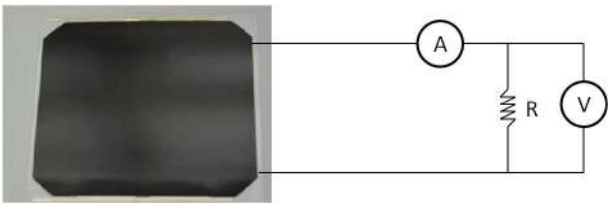

Figure 9.1: Test of an individual PV cell.

Placing a variable resistor in the circuit as shown Fig. 9.1, the curve I-V can be determine for different time periods, obtaining a similar graphic to exposed in Fig. 8.1(a), but in this case experimental values.

9.1.2 Solar Array

Although it has been determined the final solar array configuration, different configurations can be tested to study the difference between series connections or parallel connections. The assembly of the two tests with different solar array configurations will have the following structure:

1. Ten cells connected in series(10S).

   Figure 9.6 illustrates a configuration (10S), in this test it will be checked that the solar arrays produce approximately 5 V and 6 A.

(a) Physical layout. (b) Scheme of electronic connection.

Figure 9.2: Test of 10S configuration.

2. Two sets, each of 5 cell connected in series, connected in parallel (5S2P).

   Figure 9.3 illustrates a configuration (5S2P), in this test will be check that the solar arrays produce approximately 2.5 V and 12 A.

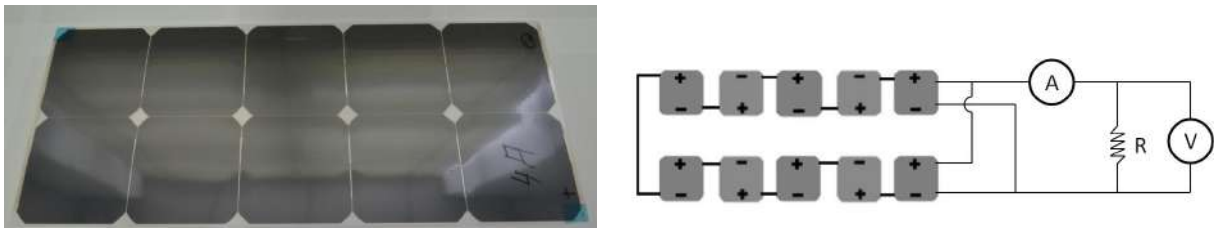

(a) Physical layout. (b) Scheme of electronic connection.

Figure 9.3: Test of 5S2P configuration.

   Figure 9.3(b) also shows the multimeter connection, including a variable resistor to determinate the I-V curve that corresponding to this configuration.

9.1.3 UAV Solar Panels

Finally, the final configuration of the solar panel of the UAV will be tested. This configuration contains two sets, each of 22 cells connected in series, connected in parallel (22S2P) as shown in the Fig. 9.4.

In the test will be check that the solar arrays produce approximately 12 V and 12 A approximately.

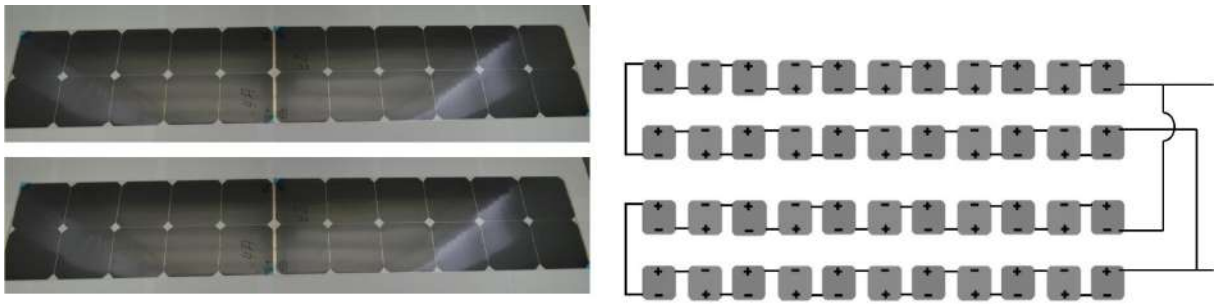

(a) Physical layout. (b) Scheme of electronic connection.

Figure 9.4: Test of 22S2P configuration.

9.2 Experimental Test of the Electric Motor and Propeller

In section 8.6, it was seen that motor-propeller test is a critical part. Besides testing the propellers described in that section, testing can be made with other types of propellers to find the optimal configuration. For this test, one will need a specific configuration connected to a stabilized power supply, to determine the thrust of the propeller with the input values that the electric motor is produced. It will be used a power supply, instead of batteries or solar panels, to get the results with the greatest possible accuracy and stability.

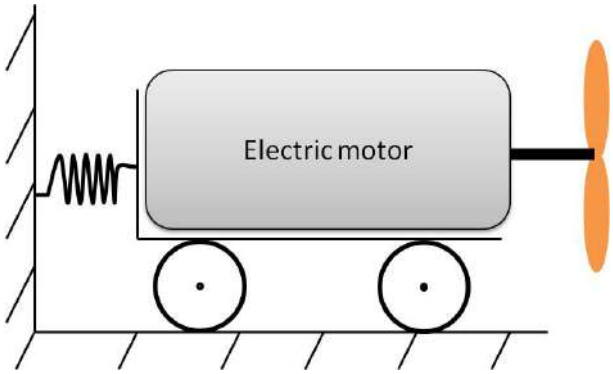

Figure 9.5: Installation for motor-propeller test.

Testing installations for internal combustion engines consists of a hydraulic brake which determines the thrust of the propeller. In the case of electric motors and aeromodelling, those installations are simpler systems, as depicted in Fig. 9.5. These facilities can be made easily with a mechanism (similar to a spring) which measures the force of the propeller and so determines the thrust produced.

In this test, it will be measures electrical values of the motor, namely voltage, current and power, and, through the mechanism explained, the thrust of the propeller will be determined.

9.3 Experimental Test of the Solar Charger

Tests are needed to study how the different levels of solar radiation influence the battery charge. For this test, it will be assembled the subsystem consisting of solar panels, solar charger and batteries as shown Fig. 9.6.

Figure 9.6: Experimental test of the solar charger controller.

This way one can know how much energy is stored in the battery, in each case, depending on the radiation, thus estimating when the mission is possible. This study also allows knowing real values of the battery recharging times, a factor that will be very useful to know how much energy will be stored in the battery during flight (recharge energy).

9.4 Experimental Test of the Speed Controller

Another important subsystem is shown in Fig. 9.7, which consist of battery, ESC and the link motor-propeller.

Figure 9.7: Experimental test of the electronic speed controller.

In this case, one has to verify that the ESC performs its function properly and provides the specifications that the electric motor, in each stage of the mission, will require. It would be interesting to obtain graphs that relate the rpm with the throttle values, and thus it can determine the motor answer in based on the operation of ESC.

9.5 Experimental test of the Complete Hybrid System

When all other tests has been successfully completed, it is then possible to test the final and complete architecture shown in Fig. 9.8.

In this case, as the operation of all subsystems was tested previously, it is only necessary to control the correct operation of all components. The voltages and currents have to be adequate and the propeller parameters (trust and power) must have the value that the mission requires.

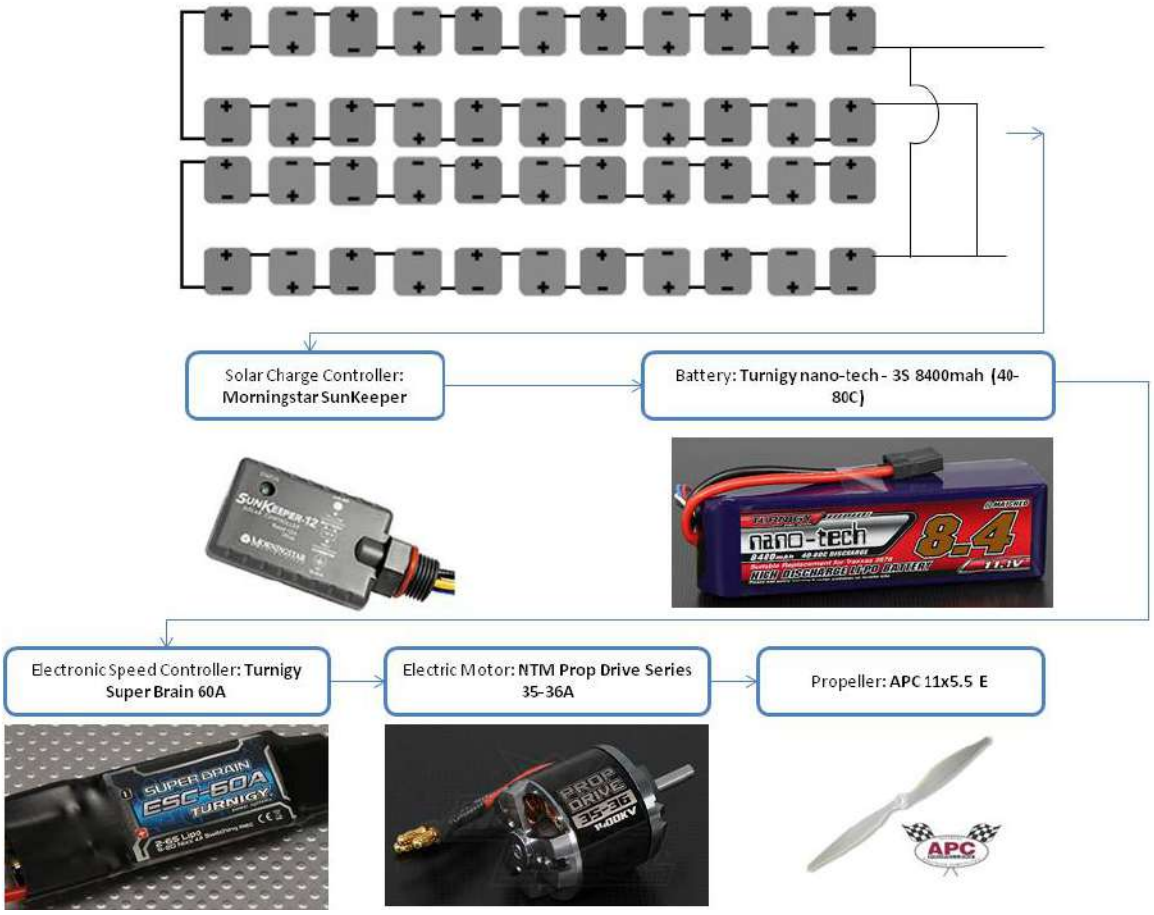

Figure 9.8: Experimental test of the complete hybrid system.

Chapter 10

Conclusions

In this chapter, a summary of what was achieved during this work is presented, also some future works are considered.

10.1 Achievements

In this thesis, the architecture of the propulsion system of a solar UAV has been defined and has been particularized for a specific mission. It was found that the design of the solar-powered plant depends not only on the mission but also the type of aircraft. Logically, depending on the characteristics of each stage of the mission, the systems can have different dimensions. According to these two conditions -mission and aircraft- and taking into account the efficiency of the propulsion system components, it has been possible to calculate the mission energy requirements that will affect all design process.

Another key point is the storage of energy. It has been seen that batteries store energy, according to a determinate capacity, but the important part was the evolution of the solar radiation profiles. These values mean that the mission specified is only possible in the summer months when the radiation values are higher. The solar-powered system is designed with a Li-Po battery and mono-crystalline solar panels with an efficiency of 22.6%, concluding that it is only possible to achieved the mission with a hybrid propulsion system. The main cause of this was determined by a very high required power for the climb stage(450 W), therefore, this is the most critical stage of the mission.

For the hybrid propulsion system designed, the possible configurations of battery and solar panels have been studied in detail, and it was shown that the best configuration to achieve the mission is a rechargeable battery with 5239 mAh of capacity as a minimum, together with a 44 photo-voltaic solar array, providing the power. Solar panels provide the remaining energy to finish the mission and sometimes provide additional energy to recharge the battery.

Once defined the hybrid propulsion system, the components were selected based on appropriate selection criteria following the design methodology. Finally, it was established a test plan to determine the accuracy and proper functioning of the designed system and that the different components and subsystems work properly.

As a general conclusion, once finished this thesis and with the knowledges learned, it is possible to discuss the direction that solar aviation will take and the applications that it might cover. In respect of direction, clearly will be increased. The topic of renewable technologies,nowadays, is present in many aspects of our lives and every day one can see the evolution in the different sectors. Therefore is reasonably thinking that the design of this type of aircrafts will increase. Moreover applications are closely related to the improvements that solar technology can achieve the next years. Typically, the world of electric aircraft was always linked to aeromodelling but now, largest prototypes and designs of green aircrafts has been developed for different applications, such as border surveillance, forest fire fighting or power line inspection. The characteristics of these aircraft are a small wingspan and low weight, which implies a small payload. In the coming years, it is expected that these parameters can improve and the aircrafts can be larger.

10.2 Future Work

Naturally, the next phase in the immediate future, is to acquire all these components and test then according to the defined test-planning. Once the tests have been successfully overcomed, the system would be in the right conditions to be installed in the aircraft and carry out the corresponding flight tests.

Other factors to be taken into account will be to discuss whether it would be necessary to add to the system a gearbox. In this first preliminary design, the gearbox was not considered because except in the climb, where more power is required, in the cruise stage, which is the longest, the speed values are constant and low compared to combustion engines, in which the gearbox is indispensable. A new design could then be proposed and see what results are obtained with this new configuration.

In addiction, new missions with different characteristics, such as higher speeds, different endurance or cruise altitudes, could be studied.

Bibliography

AE. Alternative Energy. http://www.alternative-energy-news.info/10-best-solar-airplane-concepts/, 2008. Accessed in 2013.

AEROG. Aeronautics and Astronautics Research Center. http://aeronautics.ubi.pt/, 2013. Accessed in March.

APC. Advanced Propellers Precision Composites. http://www.apcprop.com/v/downloads/PERFILES_WEB/datalist.asp, 2013. Accessed in March.

R. J. Boucher. History of solar flight. Paper 84-1429, AIAA, June 1984.

H. Bruss. *Solar Modellflug Grundlagen, Enwicklung, Praxis*. Vth, 1991.

BU. Battery University. http://batteryuniversity.com/learn/article/lithium_based_batteries, 2013.

CCTAE. Centre for Aeronautical and Space and Technology. https://fenix.ist.utl.pt/investigacao/cctae, 2013. Accessed in March.

DARPA. Defense Advanced Research Projects Agency. http://www.darpa.mil/Our_Work/TTO/Programs/Vulture.aspx, 2013. Accessed in March.

DLR. Solitair at DLR. http://www.dlr.de/ft/en/desktopdefault.aspx/tabid-1388/1918_read-3385/, 2013.

DR. Direct Industry. http://www.directindustry.com/industrial-manufacturer/photovoltaic-solar-cell-80157.html, 2013.

EERE. Energy Efficiency and Renewable Energy. http://www.fueleconomy.gov/feg/fcv_pem.shtml, 2013.

EERE. History of solar. http://www1.eere.energy.gov/solar/pdfs/solar_timeline.pdf, 2013.

EPFL. Michael Graetzel. http://lpi.epfl.ch/graetzel, 2013.

FAI. The international air sports federation. http://www.fai.org, 2013.

K. Flittie and B. Curtin. Pathfinder Solar–Powered Aircraft Flight Performance. AIAA paper 98–4446, 1998.

GRASS. Geographic Resources Analysis Support System. http://grass.osgeo.org/, 2013.

C. A. Gueymard. SMARTS, A Simple Model of the Atmospheric Radiative Transfer of Sunshine: Algorithms and Performance Assessment. Technical Report FSEC-PF-270-95, Florida Solar Energy Center., December 1995.

M. Hepperle. Electric Flight – Potential and Limitations. Lisbon, Portugal, 2012. NATO-OTAN.

HK. Hobby King. http://www.hobbyking.com/hobbyking/store/index.asp, 2013.

Hyperion. Hyperion World. http://www.hyperion-world.com/, 2013. Accessed in March.

IDMEC. Institute of Mechanical Engineering. http://www.idmec.ist.utl.pt/, 2013. Accessed in March.

INEGI. Institute of Mechanical Engineering and Industrial Management. http://inegi.inegi.up.pt/, 2013. Accessed in March.

Iroquois. History of Electric Flight. http://www.iroquois.free-online.co.uk/hist.htm, 2013.

C. J.Hartney. Design of Small Solar Powered Unmanned Aerial Vehicle. Master's thesis, San José State University, August 2011.

JRC-PVGIS. Joint Research Centre -Photovoltaic Geographical Information System. http://re.jrc.ec.europa.eu/pvgis/, 2013.

G. L. Juste. Aerorreactores en la propulsion de misiles y UAVs. Universidad Politecnica de Madrid, September 2012.

N. Karamia, N. Moubayedb, and R. Outbiba. Analysis and implementation of an adaptative pv based battery floating charger. In *Solar Energy*, volume 86, pages 2383—-2396. El Sevier, 2012.

B. Keidel. *Auslegung und Simulation von hochfliegenden, dauerhaft stationierbaren Solardrohnen*. PhD thesis, Lehrstuhl für Flugmechanik und Flugregelung, Technische Universität München, May 2000.

LAETA. Associated Laboratory for Energy, Transports and Aeronautics. http://www.idmec.ist.utl.pt/laeta/, 2013. Accessed in March.

W. McCormick. *Aerodynamics, Aeronautics and Flight Mechanics*. Wiley & Sons, Incorporated, John, 1979.

MDP. Aerodynamics for Students. http://www-mdp.eng.cam.ac.uk/web/library/enginfo/aerothermal_dvd_only/aero/propeller/prop1.html, 2013.

A. Mehta. Solar Aircraft: Future Need. Technical Report 10, Government Engineering College, Godhra, November 2012.

MM. Magazine Merckgroup. http://magazine.merckgroup.com/en/Life_and_Style/isishape/solar_cells1.html, 2013.

Morningstar. Solar Controller. http://www.morningstarcorp.com, 2013.

I. R. Morus. Grove, Sir William Robert (1811–1896). *Oxford Dictionary of National Biography*, May 2005.

NASA. National Aeronautics and Space Administration. http://www.nasa.gov/centers/glenn/technology/fuel_cells.html, 2013a.

NASA. National Aeronautics and Space Administration. http://www.nasa.gov/centers/dryden/news/FactSheets/FS-056-DFRC.html, 2013b. Accessed in January.

G. A. Nazri and G. Pistoia. *Lithium Batteries Science and Technology*. Number ISBN 978-1-4020-7628-2. 2003.

C. L. Nickol, M. D. Guynn, L. L. Kohout, and T. A. Ozoroski. High altitude long endurance uav analysis of alternatives and technology requirements development. TP 214861, NASA, March 2007.

NOAA. National Oceanic & Atmospheric Administration. http://www.esrl.noaa.gov/gmd/grad/about/rad.html, 2013.

T. E. Noll, J. M. Brown, M. E. Perez, S. D. Ishmael, G. C. Tiffany, and M. Gaier. *Investigation of the Helios Prototype Aircraft Mishap*. NASA, January 2004.

A. Noth. *Design of Solar Powered Airplanes for Continuous Flight*. PhD thesis, Swiss Federal Institute of Technology Zürich (ETHZ), September 2008a.

A. Noth. History of solar flight. July 2008b.

NREL. National Renewable Energy Laboratory. http://www.solar.rutgers.edu/DifferentTypes.htm, 2013.

PV-EDUCATION. Photovoltaic Education Network. http://pveducation.org/, 2013.

P&W. Pratt & Whitney. http://www.pratt-whitney.com/Videos/Story/pw1000g-how-it-works, 2013.

QinetiQ. Qinetiq's Zephyr UAV achieves flight record. http://www.qinetiq.com/what/products/Documents/Zephyr-UAV.pdf, 2013.

V. Quaschning. The Sun as an Energy Resource. *Renewable Energy World*, pages 90–93, May 2003.

A. Rapinett. Zephyr: A High Altitude Long Endurance Unmanned Air Vehicle. Master's thesis, University of Surrey, April 2009.

G. Romeo and G. Frulla. Heliplat: high altitude very-long endurance solar powered uav for telecommunication and earth observation applications. *The Aeronautical Journal*, 108:277–293, 2004.

K. Scharmer and J. Greif. *The European Solar Radiation Atlas*. École des Mines de Paris, 60, Boulevard Saint-Michel, 75272 Paris cedex 06, 2-911762-21-5 edition, March 2000.

SEH. Solar Electricity Handbook. http://solarelectricityhandbook.com/solar-irradiance.html, 2013.

SI. Solar Impulse. http://www.solarimpulse.com/, 2013.

D. Stinton. *The Design of the Aeroplane,*. Blackwell Science, 2001.

SunPower. C60 Solar Cell Mono Crystalline Silicon. http://us.sunpowercorp.com/, 2013.

T. C. Tozer, D. Grace, J. Thompson, and P. Baynham. IEE colloquium on "military satellite communications". In *UAVs and HAPs - Potential Convergence for Military Communications*. 2000.

D. G. Vutetakis. *The Avionics Handbook*, chapter 10. 2001. ISBN 0-8493-8348-X.

J. Vycital and T. Moravec. Espacenet. http://worldwide.espacenet.com/publicationDetails/biblio?CC=WO&NR=2010020199A1&KC=A1&FT=D&ND=&date=20100225&DB=&locale=en_EP, 2013.

Appendix A

Solar Radiation Profiles - Calculation Methodology

The content of this appendix explains the calculation methodology to obtain the solar radiation profiles. It is taken as reference the JRC (Joint Research Centre), specifically from the Photovoltaic Geographical Information System (PVGIS), which provides a map-based inventory of solar energy resource and assessment of the electricity generation from photovoltaic systems in Europe, Africa, and South-West Asia [JRC-PVGIS, 2013].

A.1 Interaction of Solar Radiation with the Earth

The term irradiance is used to consider the solar power (instantaneous energy) falling per unit area [W/m^2]. The term irradiation is used to consider the amount of solar energy falling on unit area over a stated time interval [Wh/m^2]. The same symbols are used for irradiance and irradiation but the two concepts can be differentiated by context or by the attached units.

The interaction of solar radiation with the earth's atmosphere and surface is determined by three groups of factors:

1. The Earth's geometry, revolution and rotation (declination, latitude, solar hour angle);
2. Terrain (elevation, surface inclination and orientation, shadows);
3. Atmospheric attenuation (scattering, absorption) by:
   - 3.1 gases (air molecules, ozone, CO_2 and O_2);
   - 3.2 solid and liquid particles (aerosols, including non-condensed water);
   - 3.3 clouds (condensed water).

The first group of factors determines the available extraterrestrial radiation based on solar position above horizon and can be precisely calculated using astronomic formulas.

The radiation input to the Earth's surface is then modified by its terrain topography, namely slope inclination and aspect, as well as shadowing effects of neighboring terrain features. This group of factors can be also modeled at high level of accuracy. The elevation above sea level determines the attenuation of radiation by the thickness of the atmosphere.

Intensity of the extraterrestrial solar radiation traversing through the earth's atmosphere is attenuated by various atmospheric constituents, namely gases, liquid and solid particles and clouds. The path length through atmosphere is also critical. Because of its dynamic nature and complex interactions the atmospheric attenuation can be modeled only at a certain level of accuracy that decreases from 3.1 to 3.3.

The attenuation by gas constituents (factors 3.1) describes clear and dry (Rayleigh) atmosphere and is given by its relative optical air mass and optical thickness (m and d_R(m) respectively).

The attenuation by solid and liquid particles (factors 3.2) is described by the Linke turbidity (T_{LK}). It indicates the optical density of hazy and humid atmosphere in relation to a clean and dry atmosphere.

Clouds (factor 3.3) are the strongest attenuates. Theoretical analysis of the attenuation of solar radiation passing through clouds requires great deal of information regarding instantaneous thickness, position and number of layers of clouds, as well as their optical properties. Therefore a simple empirical techniques are used to estimate the attenuation of cloud cover. The radiation, selectively attenuated by the atmosphere, which is not reflected or scattered and reaches the surface directly is beam (direct) radiation. The scattered radiation that reaches the ground is diffuse radiation. The small part of radiation that is reflected from the ground onto the inclined receiver is reflected radiation. These three components of radiation together create global radiation.

In many applications, a study of solar radiation under clear (i.e. cloudless) skies is very important. Maximum insolation is obtained when skies are absolutely clean and dry and relatively less radiation is received when aerosols are also present. Omitting the clouds attenuation factor (factor 3.3) leads to clear-sky radiation values.

A.2 Computation Scheme of Solar Radiation Database

Solar energy is one of the environmentally sustainable resources for producing electricity using photovoltaic (PV) systems. The main input data used in the planning process is solar radiation. A solar radiation database from climatologic data homogenized for Europe is available in the European Solar Radiation Atlas, using the *r.sun model* [GRASS, 2013].

The model algorithm estimates beam, diffuse and reflected components of the clear-sky and real-sky global irradiance/irradiation on horizontal or inclined surfaces. The total daily irradiation [Wh/m^2] is computed by the integration of the irradiance values [W/m^2] calculated at regular time intervals over the day. For each time step during the day, the computation accounts for sky obstruction (shadowing) by local terrain features (hills or mountains), calculated from the digital elevation model.

The database consists of raster maps representing twelve monthly averages and one annual average of daily sums of global irradiation for horizontal surfaces, as well as those inclined at angles of 15, 25,

and 40 degrees. Besides these data, raster maps of clear-sky irradiation, the Linke turbidity, and the ratio D/G were computed. The scheme below describes the methodology and accuracy of the database. See the interactive web applications to browse and query the data [JRC-PVGIS, 2013].

Calculation steps:

1. Computation of clear-sky global irradiation on a horizontal surface.
2. Calculation and spatial interpolation of clear-sky index and computation of raster maps of global irradiation on a horizontal surface.
3. Computation of the diffuse and beam components of overcast global irradiation and raster maps of global irradiation on inclined surfaces.
4. Accuracy assessment and comparison with ESRA interpolated maps.

These four steps are described in some detail in the following subsections.

A.2.1 Clear-sky Global Irradiation on a Horizontal Surface

All raster maps (4500 x 5000 cells) with a cell resolution of 1x1 km were integrated into a GIS database. The elevation was derived from the USGS SRTM digital elevation model with a primary resolution of 30 arc seconds.

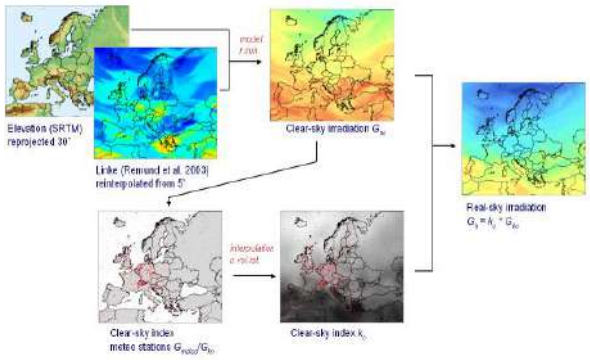

Figure A.1: Calculation scheme for horizontal irradiation.

The monthly averages of the Linke turbidity factor T_{LK} were reinterpolated from the global database [Remund et al, 2003], available also at the SoDa service. The accuracy of the data from this source is reported to $RMSE = 0.7T_{LK}$ units. To eliminate the effect of elevation, the pressure correction suggested by [Remund et al, 2003] to T_{LK} values was applied. The 12 monthly raster maps of T_{LKn} values were prepared (Fig A.2).

Following the 12 monthly averages of daily sums of clear-sky global irradiation G_{hc} [Wh/m^2] were computed. The time step for the integration of irradiance values was set to 0.25 hour while day numbers and declination values for each month were set according to the ESRA. The most critical issue in this stage is the Linke turbidity factor as its estimation is still prone to large uncertainty.

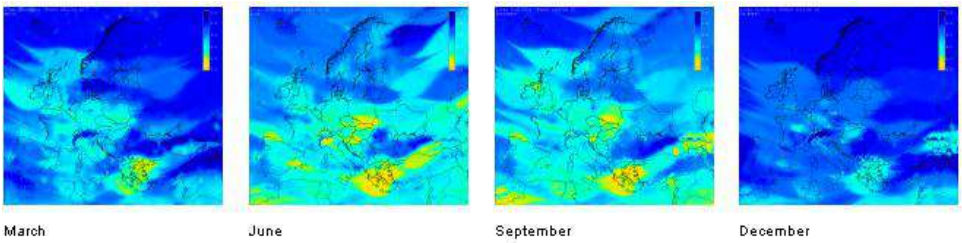

Figure A.2: Monthly averages of the Linke turbidity coefficient (T_{LK}).

A.2.2 Global Irradiation on a Horizontal Surface

The global irradiation for real-sky conditions was calculated using the clear-sky radiation G_{hc} and the clear-sky index k_c. For the European subcontinent, the climatologic database for 566 meteorological stations was available (source ESRA), comprising geographical position and monthly means of global G_{hs}, beam B_{hs} and diffuse D_{hs} irradiation on a horizontal surface. The clear-sky index k_c in this case expresses the ratio between monthly averages of global irradiation for real-sky and clear-sky conditions. For each meteorological station, k_c was calculated (equation A.40) from the clear-sky irradiation values G_{hc} computed in the previous step and interpolated into the maps.

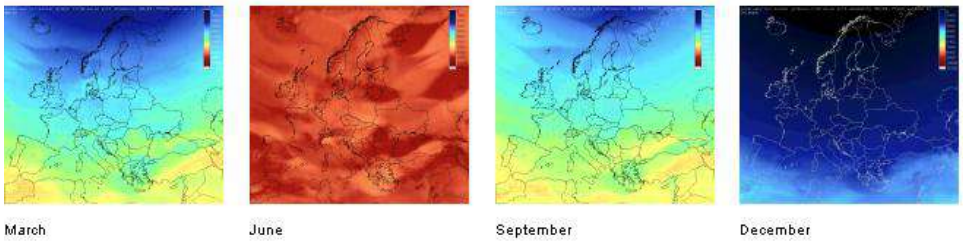

Figure A.3: Monthly averages of daily sum of clear-sky global irradiation (G_{hc}).

Although the available meteorological stations do not cover the study area evenly and in mountainous regions they are rather rare, it can be seen that the clear-sky index is correlated with SRTM-30 elevation, especially in summer and winter (Fig A.4). Therefore, to create the raster maps of k_c, accounting for changes in vertical dimension, it was decided to apply a multivariate spatial interpolation procedure using regularized spline with tension that was implemented in the GRASS GIS as the *s.vol.rst* command. As the interpolation results are very sensitive to the setting of input parameters (tension, smoothing and vertical scaling), a crossvalidation procedure was applied separately for each of the twelve monthly data sets. The raster maps of overcast global irradiation on a horizontal surface G_h [Wh/m^2] were then calculated using equation (A.39).

A.2.3 Global Irradiation on Inclined Surfaces

The components of the irradiance/irradiation are affected in different ways by cloudiness and shadowing by the terrain features, or by tilting the surface away from the horizontal position. Variation in any of these parameters will therefore change the ratio between the beam and diffuse components.

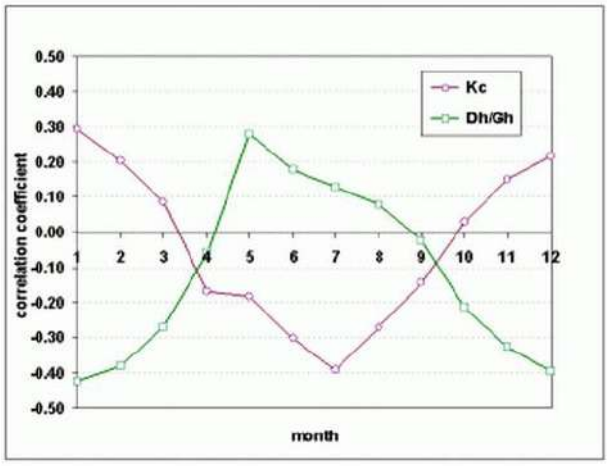

Figure A.4: Correlation between k_c and D_h/G_h to elevation (based on a subset from the Central and Southeastern Europe).

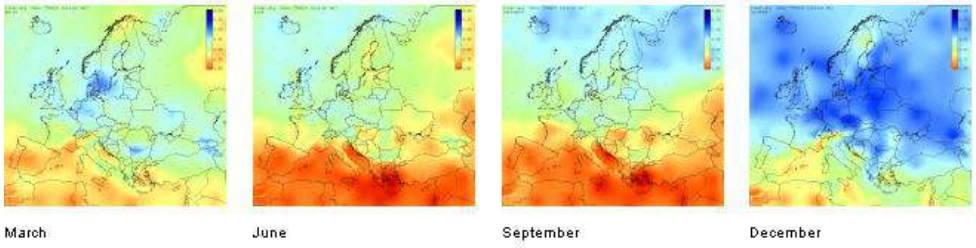

Figure A.5: Monthly averages of the clear-sky index (k_c).

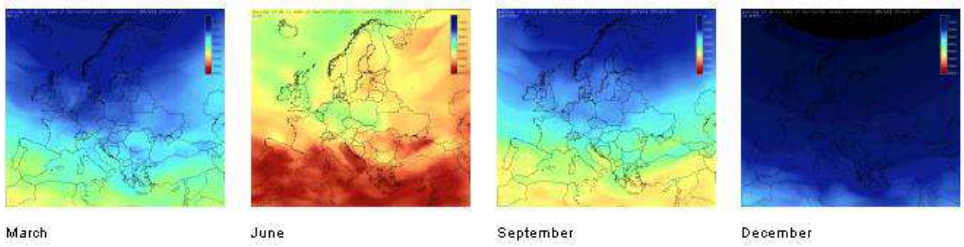

Figure A.6: Monthly averages of daily sum of global irradiation (G_h) - unified color table.

To compute global irradiation on inclined surfaces G_i at real (average) atmospheric conditions, the ratio D_{hs}/G_{hs} was calculated using the meteorological data. The monthly averages of raster maps were interpolated using *s.vol.rst* in the same procedure as for the clear-sky index (Fig A.7).

The raster maps of diffuse and beam components of global irradiation for overcast conditions as well as both components of the clear-sky index were computed (equations A.41). Finally, the monthly averages of daily sums of global irradiation input to southwards-oriented solar panels were computed for the inclination angles of 15, 25, 40 and 90 degrees. The ground albedo was considered as a constant 0.15. The methodological details can be seen in section A.3.

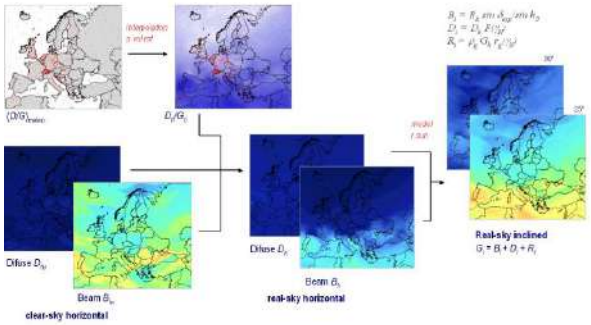

Figure A.7: Calculation scheme for irradiation at inclined surface.

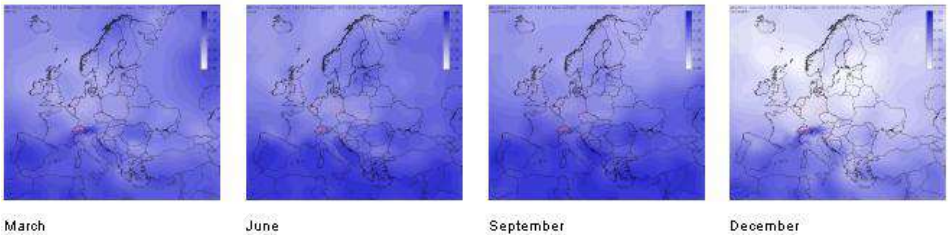

Figure A.8: Monthly averages of the diffuse/global ratio D_h/G_h.

A.2.4 Accuracy Assessment and Comparison of PVGIS and ESRA Maps

The ESRA database consists of primary irradiation data measured or calculated for a set of European meteorological stations (566 of them in our region). The raster maps of monthly averages of daily sums of global radiation for horizontal surface were created from the primary data by kriging. The co-kriging method supported by satellite data did not prove to give higher accuracy due to low resolution of satellite data and their unsatisfactory correlation with ground measurements, particularly in winter months.

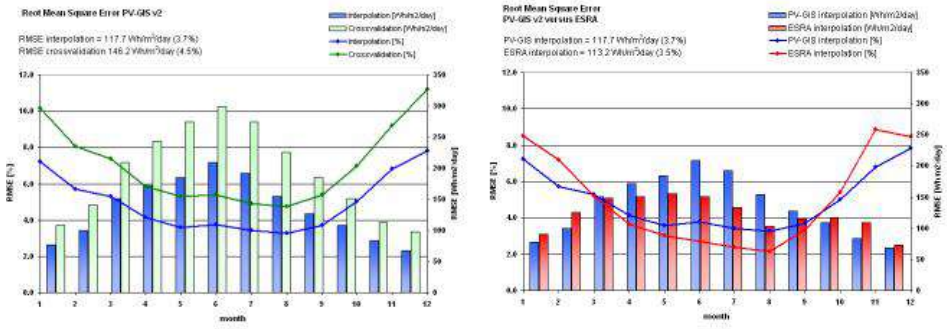

Figure A.9: RMSE of PVGIS and ESRA maps (interpolation and crossvalidation).

The modelling accuracy of the PVGIS values in the database was evaluated against the input meteorological data used in the computation. Comparing the yearly averages of the daily global horizontal irradiation, the mean bias error (MBE) is 8.9 Wh/m^2 (0.3%) and the root mean square error (RMSE) is 118 Wh/m^2 (3.7%).

The calculation of RMSE for comparing the primary irradiation (from meteo stations) with PVGIS (version 2) and ESRA raster maps respectively is presented in Fig A.9. The tests were realized using

measurements of horizontal irradiation from 563 stations across the region. The root mean square error (RMSE) of our results to the original measurements of daily global irradiation that were used for the interpolation of kc index occur within an interval of 68 to 209 Wh/m^2. In relative terms, it is within the interval of 3.2% to 7.8%, the RMSE values peak in winter months. The comparison of the ESRA interpolation approach shows, that although the overall accuracy is practically the same (the yearly average of the RSME for ESRA is 113 Wh/m^2, i.e. 3.5%), the PVGIS modeled values are slightly better in period from October to April and poorer in summer months.

This analysis provides information about the errors only in locations for which the measurements are known. Therefore a cross-validation was applied in order to estimate the predictive accuracy of the modelling approach that better explains the distribution of errors further from the locations with known measurements. The crossvalidation error shows the maximum possible error that might occur at the given point if it was not taken into consideration in the interpolation. The average yearly MBE from cross-validation is smaller: 1 Wh/m^2 (0.03%), but the range of monthly averages of MBE is higher – from -3 Wh/m^2 in January to 4 Wh/m^2 in August. The cross-validation RMSE is higher, within the interval of 97 to 299 Wh/m2/day (4.7% to 11.2%), and the yearly average is 146 Wh/m^2 (4.5%).

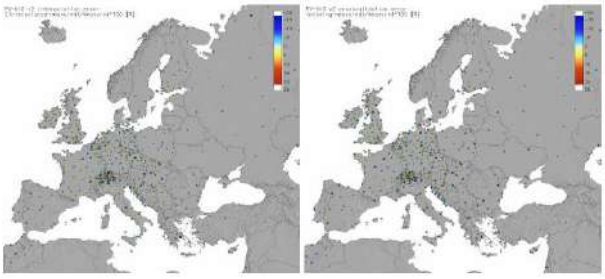

Figure A.10: RMSE of interpolation (detail of mountains) and crossvalidation.

The advantage of this approach is linking the terrain features with changes in radiation fields and considering the shadowing effects - see the comparison of the annual average of global horizontal irradiation calculated by ESRA and r.sun (Fig A.10). The multivariate regularized spline with tension provides k_c raster maps that better fit the regional specifications of radiation climate in the mountainous areas on condition that a more dense pattern of ground measurements would be available. The influence of terrain shadowing is more visible when higher resolution data (namely digital terrain model) are used. As can be seen the raster cell resolution of 1 km^2 is still too rough to reveal the real shadowing patterns in mountainous landscape.

A.3 Solar Radiation Model *r.sun* and its Implementation in GRASS GIS

The *r.sun* model is implemented in the GRASS GIS open source environment using the C programming language and is freely available since release 5.0.0 [GRASS, 2013]. The model works in two modes. In mode 1 for the instant time [second], it calculates raster maps of selected components (beam, diffuse

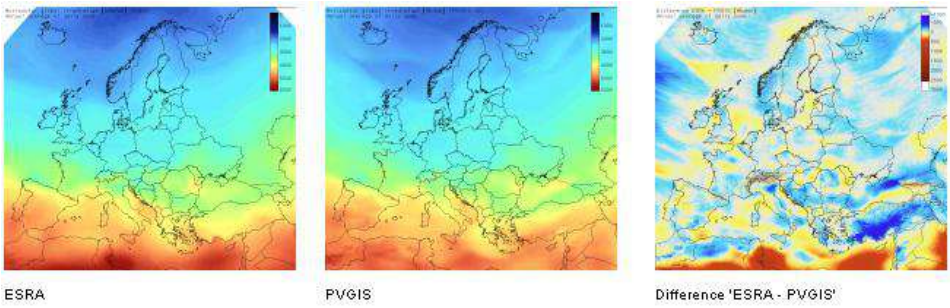

Figure A.11: Comparison of yearly averages of daily sum of global horizontal irradiation (G_h) calculated by ESRA, PVGIS and the differences.

and reflected) of solar irradiance [W/m^2] and solar incident angle [degrees]. In mode 2, the raster maps of daily sum of solar irradiation [Wh/m^2] and duration of the beam irradiation [minutes] are computed as integration of irradiance values that are calculated in a selected time step from sunrise to sunset. Using a command script, these two modes can be used separately or in a combination to provide estimates for any desired time steps or intervals. Besides clear-sky irradiances/irradiations, the model can calculate overcast values on condition that the clear-sky index is defined. The model accounts for a sky obstruction by local terrain features using an optional shadowing parameter. Considering shadowing effects in mountainous areas can result in a dramatic decrease of radiation values especially at low sun altitudes.

The model requires only a few mandatory input parameters – elevation above sea level, slope and aspect of the terrain or surface, day number (for mode 2), and a local solar time (for mode 1). The other input parameters are either internally computed (solar declination) or the values can be overridden by explicitly defined settings to fit the specific user needs: Linke atmospheric turbidity, ground albedo, beam and diffuse components of clear-sky index, time step used for calculation of all-day irradiation from sunrise to sunset and sampling density at which the visibility of a raster cell is evaluated. Spatially distributed parameters can be set as raster maps. Geographical latitude for each cell can be computed internally. According to the setting of parameters, the model automatically recognizes between modes 1 and 2. Details of the command (synopsis, description, notes) can be found in the program manual pages [JRC-PVGIS, 2013].

A.3.1 Computing Clear-sky Radiation

Beam radiation

Outside the atmosphere, at the mean solar distance, the beam irradiance, also known as the solar constant (I_0), is 1367 $W.m^2$. The Earth's orbit is lightly eccentric and the Sun-Earth distance varies slightly across the year. Therefore, a correction factor e, to allow for the varying solar distance, is applied in calculation of the extraterrestrial irradiance G_0 normal to the solar beam as

$$G_0 = I_0 \cdot e\,, \tag{A.1}$$

where:

$$e = 1 + 0.03344 \cdot cos(j' - 0.048869)\,, \tag{A.2}$$

with the day angle j' in radians as

$$j' = 2 \cdot p \cdot j/365.25\,, \tag{A.3}$$

being j the day number which varies from 1 on January 1st to 365 (366) on December 31st.

The beam irradiance normal to the solar beam B_{0c}, is attenuated by the cloudless atmosphere, and calculated as

$$B_{0c} = G_0 \exp\left(-0.8662 \cdot TLK \cdot m \cdot dR(m)\right). \tag{A.4}$$

The term -0.8662 TLK is the air mass 2 Linke atmospheric turbidity factor [dimensionless] corrected by Kasten (1996). The parameter m in equation (A.4) is the relative optical air mass [-] calculated using

$$m = (p/p0)/(sin\, h_0^{ref} + 0.50572 \cdot (h_0^{ref} + 6.07995) - 1.6364)\,, \tag{A.5}$$

where h_0^{ref} is the corrected solar altitude h_0 (an angle between the sun and horizon) in degrees by the atmospheric refraction component Dh_0^{ref} using

$$Dh_0^{ref} = 0.061359 \cdot (0.1594 + 1.123 \cdot h_0 + 0.065656 \cdot h_0^2)/(1 + 28.9344 \cdot h_0 + 277.3971 \cdot h_0^2)\,, \tag{A.6}$$

with

$$h_0^{ref} = h_0 + Dh_0^{ref}\,. \tag{A.7}$$

The p/p_0 component in equation (A.5) is the correction for a given elevation z given by

$$p/p0 = \exp\left(-z/8434.5\right). \tag{A.8}$$

The parameter d_R in equation (A.4) is the Rayleigh optical thickness at air mass m and is calculated according to the improved formula by Kasten (1996) [JRC-PVGIS, 2013] as follows:

for m $<=$ 20:

$$d_R(m) = 1/(6.6296 + 1.7513 \cdot m - 0.1202 \cdot m^2 + 0.0065 \cdot m^3 - 0.00013 \cdot m^4) \tag{A.9}$$

for m $>$ 20

$$d_R(m) = 1/(10.4 + 0.718 \cdot m) \tag{A.10}$$

The beam irradiance on a horizontal surface B_{hc} is then calculated as

$$B_{hc} = B_{0c} \cdot sin\, h_0\,, \tag{A.11}$$

where h_0 is the solar altitude angle given by equation (A.30).

The beam irradiance on an inclined surface B_{ic} is calculated as

$$B_{ic} = B_{0c} \cdot sin\, d_{exp} \tag{A.12}$$

or

$$B_{ic} = B_{hc} \cdot sin\,(d_{exp}/sin\, h_0)\,, \tag{A.13}$$

where d_{exp} is the solar incidence angle measured between the Sun and an inclined surface (equation A.34).

Diffuse radiation

As the cloudless sky becomes more turbid, the diffuse irradiance increases while the beam irradiance decreases. The estimation of the diffuse component on a horizontal surface D_{hc} is made as a product of the normal extraterrestrial irradiance G_0, a diffuse transmission function *Tn* dependent only on the Linke turbidity factor T_{LK}, and a diffuse solar altitude function F_d dependent only on the solar altitude h_0:

$$D_{hc} = G_0 \cdot Tn\,(TLK) \cdot Fd\,(h_0) \tag{A.14}$$

The estimate of the transmission function *Tn(TLK)* gives a theoretical diffuse irradiance on a horizontal surface with the Sun vertically overhead for the air mass 2 Linke turbidity factor. The following second order polynomial expression is used:

$$Tn\,(TLK) = -0.015843 + 0.030543 \cdot TLK + 0.0003797 \cdot TLK^2\,. \tag{A.15}$$

The solar altitude function is evaluated using

$$Fd\,(h_0) = A1 + A2 \cdot sin\, h_0 + A3 \cdot sin^2\, h_0\,, \tag{A.16}$$

where the values of the coefficients *A1*, *A2* and *A3* depend on the Linke turbidity TLK as

$$A1' = 0.26463 - 0.061581 \cdot TLK + 0.0031408 \cdot TLK^2 \tag{A.17}$$

$$A1 = 0.0022/Tn\,(TLK), \quad if:\ A1'\,Tn(TLK) < 0.0022$$
$$A1 = A1', \quad if:\ A1'\,Tn(TLK) >= 0.0022$$
$$A2 = 2.04020 + 0.018945 \cdot TLK - 0.011161 \cdot TLK^2$$
$$A3 = -1.3025 + 0.039231 \cdot TLK + 0.0085079 \cdot TLK^2$$

The model for estimating the clear-sky diffuse irradiance on an inclined surface D_{ic} distinguishes between sunlit, potentially sunlit and shadowed surfaces. The equations (Muneer 1990) [JRC-PVGIS, 2013] are

a) for sunlit surfaces and non-overcast sky (h_0 in radians):

$if \;\; h_0 >= 0.1\,(i.e.\,5.7^{\circ})$

$$D_{ic} = D_{hc} \cdot (F\,(g_N) \cdot (1 - K_b) + K_b \cdot sin\, d_{exp}/sin\, h_0) \tag{A.18}$$

$if \;\; h_0 < 0.1$

$$D_{ic} = D_{hc} \cdot (F\,(g_N) \cdot (1 - K_b) + K_b \cdot sin\, g_N \cdot cos A_{LN}/(0.1 - 0.008 \cdot h_0)) \tag{A.19}$$

where

$$A^*_{LN} = A_0 - A_N \tag{A.20}$$

$$A_{LN} = A^*_{LN}, \quad if: \; -p <= A^*_{LN} <= p$$
$$A_{LN} = A^*_{LN} - 2p, \quad if: \; A^*_{LN} > p$$
$$A_{LN} = A^*_{LN} + 2p, \quad if: \; A^*_{LN} < -p$$

b) for surfaces in shadow ($d_{exp} < 0\, and\, h0 >= 0$):

$$D_{ic} = D_{hc} \cdot F\,(g_N) \tag{A.21}$$

where $F\,(g_N)$ is a function accounting for the diffuse sky irradiance that may be calculated by the following equation (g_N in radians):

$$F\,(g_N) = r_i\,(g_N) + (sin\, g_N - g_N \cdot cos\, g_N - p \cdot sin^2\,(g_N/2)) \cdot N \tag{A.22}$$

where $r_i\,(g_N)$ is a fraction of the sky dome viewed by an inclined surface given by

$$r_i\,(g_N) = (1 + cos\, g_N)/2\,, \tag{A.23}$$

and value of N for surfaces in shadow is 0.25227. For sunlit surfaces under clear sky, N is calculated as

$$N = 0.00263–0.712 \cdot K_b–0.6883 \cdot K_b^2\,. \tag{A.24}$$

The K_b is a measure of the amount of beam irradiance available (proportion between beam irradiance and extraterrestrial solar irradiance on a horizontal surface) given by

$$K_b = B_{hc}/G_{0h}\,, \tag{A.25}$$

where G_{0h} is calculated as

$$G_{0h} = G_0 \cdot sin\, h_0\,. \tag{A.26}$$

Ground reflected radiation

The estimation of the clear-sky ground reflected irradiance for inclined surfaces (R_i) relies on an isotropic assumption. The ground reflected clear-sky irradiance received on an inclined surface is proportional to the global horizontal irradiance G_{hc}, to the mean ground albedo r_g and a fraction of the ground viewed by an inclined surface $r_g(g_N)$,

$$R_i = r_g \cdot G_{hc} \cdot r_g(g_N)\,, \tag{A.27}$$

where:

$$r_g(g_N) = (1 - cos\, g_N)/2 \tag{A.28}$$

and global irradiance on a horizontal surface G_{hc} is given as a sum of its beam and diffuse component,

$$G_{hc} = B_{hc} + D_{hc}\,. \tag{A.29}$$

In Scharmer and Greif (2000, page 141) [Scharmer and Greif, 2000] typical albedo values for a variety of ground surfaces are listed. In general the values of 0.2 or 0.15 are mostly used.

Position of the Sun

The position of the Sun with respect to a horizontal surface is given by the two co-ordinates – solar altitude h_0 (an angle between the Sun path and a horizontal surface), and solar azimuth A_0 (horizontal angle between the Sun and meridian - measured from East), and is calculated as (Krcho 1990, Jenčo 1992) [GRASS, 2013]

$$sin\, h_0 = C_{31} \cdot cos\, T + C_{33} \tag{A.30}$$

$$cos\, A_0 = (C_{11} \cdot cos\, T + C_{13})/((C_{22} \cdot sin\, T)^2 + (C_{11} \cdot cos\, T + C_{13})^2)^{1/2}$$

where

$$C_{11} = sin\, j \cdot cos\, d \tag{A.31}$$

$$C_{13} = -cos\, j \cdot sin\, d$$

$$C_{22} = cos\, d$$

$$C_{31} = cos\, j \cdot cos\, d$$
$$C_{33} = sin\, j \cdot sin\, d$$

The Sun declination d [rad] is computed according to Gruter (1984) [GRASS, 2013]

$$d = arcsin\left(0.3978 \cdot sin\left(j' - 1.4 + 0.0355 \cdot sin\left(j' - 0.0489\right)\right)\right), \tag{A.32}$$

where the calculation of the day angle j' is explained in equation (A.3). The hour angle T [rad] is calculated from the local solar time t expressed in decimal hours on the 24 hour clock as

$$T = 0.261799 \cdot (t - 12) \tag{A.33}$$

The position of the Sun with respect to an inclined surface (the solar incidence angle) is defined by the angle d_{exp}. If an inclined surface is defined by the inclination angle g_N and the azimuth (aspect) A_N (an angle between the projection of the normal on the horizontal surface and East) then:

$$sin\, d_{exp} = C'_{31} \cdot cos\left(T - l'\right) + C'_{33}\,, \tag{A.34}$$

where

$$C'_{31} = cos\, j' \cdot cos\, d \tag{A.35}$$
$$C'_{33} = sin\, j' \cdot sin\, d$$

and

$$sin\, j' = -cos\, j \cdot sin\, g_N \cdot cos\, A_N + sin\, j \cdot cos\, g_N \tag{A.36}$$
$$tg\, l' = -(sin\, g_N \cdot sin\, A_N)/(sin\, j \cdot sin\, g_N \cdot cos\, A_N + cos\, j \cdot cos\, g_N).$$

The hour angle of the time of sunrise/sunset over a horizontal surface $T_h^{r,s}$ can be calculated then as

$$cosT_h^{r,s} = -C_{33}/C_{31}\,. \tag{A.37}$$

The hour angle of the time of sunrise/sunset over an inclined surface $T_i^{r,s}$ can be calculated by analogy as

$$cos(T_i^{r,s} - l') = -C'_{33}/C'_{31}\,. \tag{A.38}$$

A.3.2 Computing Real-sky Radiation

The real-sky irradiance/irradiation are calculated from clear-sky raster maps by the application of a factor parameterizing the attenuation of cloud cover. However, the cloudiness observation by a meteorological service routine is usually prone to subjective errors and does not describe sufficiently the physical nature

and dynamic spatial-temporal pattern of different types of cloud cover. Therefore, a simpler parameter has to be used. The solutions for horizontal and inclined surfaces are slightly different.

For the assessment of global irradiance/irradiation on a horizontal surface under overcast conditions G_h, the clear-sky values G_{hc} are multiplied by clear-sky index k_c:

$$G_h = G_{hc} \cdot k_c \,. \tag{A.39}$$

The index k_c represents the atmospheric transmission expressed as a ratio between horizontal global radiation under overcast and clear-sky conditions. For a set of ground meteorological stations the clear-sky index can be calculated from measured global radiation G_{hs} and computed values of clear-sky global radiation G_{hc} as

$$k_c = G_{hs}/G_{hc} \,. \tag{A.40}$$

As an alternative the k_c can be derived also from other climatologic data. The raster maps of k_c must be then derived by spatial interpolation. The k_c can be calculated directly as a raster map from short-wave surface irradiance measured by satellites. This method is based on the complementarity between the planetary albedo recorded by the radiometer and the surface radiant flux (Cano et al 1986, Beyer et al 1996, Hammer et al 1998).

To compute the overcast global irradiance/irradiation for inclined surfaces, G_i the diffuse D_h and beam B_h components of overcast global radiation and of the clear-sky index k_c have to be treated separately as follows from the equations (A.18), (A.19), (A.21) and (A.29):

$$D_h = D_{hc} \cdot k_c^d \tag{A.41}$$

$$B_h = B_{hc} \cdot k_c^b$$

The ratio of diffuse to the global radiation D_h/G_h for clear and overcast skies changes according to the cloudiness. In Europe the D_h/G_h values are typically in interval 0.3-1.0. The underlying physical processes are quite complicated and computationally represented only by empirical equations (cf. Scharmer and Greif, 2000, Kasten and Czeplak 1980, Hrvoľ 1991) [Scharmer and Greif, 2000]. However, for many meteorological stations, besides the global horizontal radiation G_{hs}, the diffuse component D_{hs} is either measured or calculated from cloudiness, sunshine or other climatologic data. The raster map of D_{hs}/G_{hs} can be derived from the point values by spatial interpolation. Consecutively, the raster maps of diffuse and beam components of the clear sky index can be computed:

$$D_h = G_h \cdot D_{hs}/G_{hs} \tag{A.42}$$

$$B_h = G_h – D_h$$
$$k_c^d = D_h/D_{hc}$$
$$k_c^b = B_h/B_{hc}$$

where subscript s is meant to distinguish data measured on meteorological stations B_{hs} and D_{hs} from the estimated values B_h, and D_h.

A.3.3 Implementation in GRASS GIS

The presented solar radiation model is a substantial improvement of the older version (Hofierka 1997) [GRASS, 2013], which application was limited only to small areas and clear-sky beam radiation. The new model provides a solution for all three components of global solar radiation under clear-sky or overcast conditions. Large areas can be modelled accurately using spatially variable parameters, and shadowing effects of terrain can be modelled by new effective shadowing algorithm.

The *r.sun* works in two modes. In the mode 1 - for the instant time - it calculates a solar incident angle [degrees] and solar irradiance values [W/m^2]. In the mode 2 the daily sum of solar irradiation [$Wh/m^2/day$] and duration of the beam irradiation are computed within a given day. By scripting, the two modes can be used separately or in a combination to provide estimates for any desired time steps or intervals. The model accounts for a sky obstruction by local relief features using an optional shadowing parameter. Details of the command (synopsis, description, notes) can be found on *r.sun* manual page [GRASS, 2013].

Model inputs

The model requires only a few mandatory input parameters – digital terrain model (elevation, slope, aspect – elevin, slopein, aspin), day number day (for mode 2), and additionally a local solar time time (for mode 1). However, several other parameters can be set to fit the specific user needs. These parameters have default values that are used unless they are overridden by user settings as a single value or a name of the raster. The table 1 presents a list of all input parameters.

Parameter name	Type of input	Description	Mode	Units	Interval of values
elevin	raster	elevation	1, 2	meters	[0,8900]
aspin	raster	aspect (solar panel azimuth)	1, 2	decimal degrees	[0,360]
slopein	raster	slope (solar panel inclination)	1, 2	decimal degrees	[0,90]
linkein	raster	Linke atmospheric turbidity	1, 2	dimensionless	[0,7]
lin	single value	Linke atmospheric turbidity	1, 2	dimensionless	[0,7]
albedo	raster	ground albedo	1, 2	dimensionless	[0,1]
alb	single value	ground albedo	1, 2	dimensionless	[0,1]
latin	raster	latitude	1, 2	decimal degrees	[-90,90]
lat	single value	latitude	1, 2	decimal degrees	[-90,90]
coefbh	raster	clear-sky index for beam component	1, 2	dimensionless	[0,1]
coefdh	raster	clear-sky index for diffuse component	1, 2	dimensionless	[0,1]
day	single value	day number	1, 2	dimensionless	[0,366]
declin	single value	solar declination	1, 2	radians	[-0.409,0.409]
time	single value	local (solar) time	1	decimal hours	[0,24]
step	single value	time step	2	decimal hours	[0.01,1]
dist	single value	sampling distance coefficient for shadowing	1, 2	dimensionless	[0.1,2]

Table A.1: *r.sun* input parameters.

Solar declination is computed internally using equation (A.32) and day number unless an explicit value of declin is used. In the case that user's data are localised in GRASS location with defined projection, *r.sun* uses internal GRASS function to get geographical latitude for every raster cell. Otherwise, the

user can set the latitude as a constant lat for the whole computed region or, as a raster latin representing spatially distributed values over larger region. Similarly, the Linke turbidity factor and ground albedo can be set as a spatially averaged (single) values lin, alb or spatially distributed parameters linkein, albedo. The step parameter defines time step used for all-day irradiation calculation from sunrise to sunset. The default value is 0.5 hour. The shadowing effect of terrain can be taken into account using the –s flag. The dist parameter defines the sampling density at which the visibility of a raster cell is computed in the direction of solar beam. The values above 1.0 are suitable for fast, but less accurate estimates, while values less 1.0 for slower and more precise calculations. It is recommended to use values in the range 0.5 – 1.5.

Model outputs

According to the setting of output parameters the model automatically recognises between modes 1 and 2. When calculating in mode 1 the solar incident angle incidout, and solar irradiance raster maps *beam_rad*, *diff_rad* and *refl_rad* are computed. Calculation in mode 2 gives the sums of solar irradiation within a specified day for selected components of global irradiation *beam_rad*, *diff_rad* and *refl_rad*. A raster map showing duration of beam irradiation *insol_time* can be computed as well.

Besides clear-sky irradiances/irradiations, the model can calculate overcast radiation on conditions that coefbh and coefdh input raster maps are defined, expressing the beam and diffuse components of clear-sky index (equations A.42).

The incidence angle and irradiance/irradiation maps can be computed without considering the terrain shadowing by default or with shadowing effects by setting the flag -s. In mountainous areas this can lead to very different results especially at low sun altitudes. The value of a shadowed area is written to the output maps as zero. The table 2 presents a list of all output raster maps.

Besides output raster maps, the model stores basic solar radiation parameters used in the computation in *r.sun_out.txt* local text file. Currently it contains day number, solar constant, extraterrestrial irradiance, solar declination, interval of latitude, times of sunrise and sunset, time step, interval of used Linke turbidity and ground albedo.

Solar radiation modeling for periods longer or shorter than one day can be done using UNIX shell scripting within GRASS GIS environment.

Parameter name	Description	Mode	Units
incidout	solar incidence angle	1	decimal degrees
beam_rad	beam irradiance	1	W/m^2
diff_rad	diffuse irradiance	1	W/m^2
refl_rad	ground reflected irradiance	1	W/m^2
insol_time	duration of the beam irradiation	2	min.
beam_rad	beam irradiation	2	$Wh/m^2/day$
diff_rad	diffuse irradiation	2	$Wh/m^2/day$
refl_rad	ground reflected irradiation	2	$Wh/m^2/day$

Table A.2: *r.sun* output raster maps.

Appendix B

Monthly Solar Irradiation Levels

This appendix shows the daily levels of each month, it is also shown the daily power distribution per month.

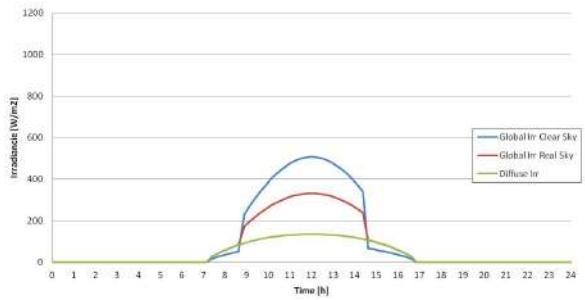

(a) January.

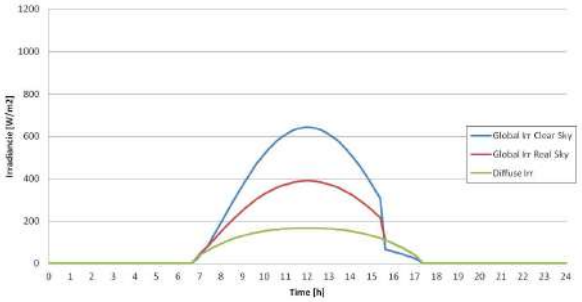

(b) February.

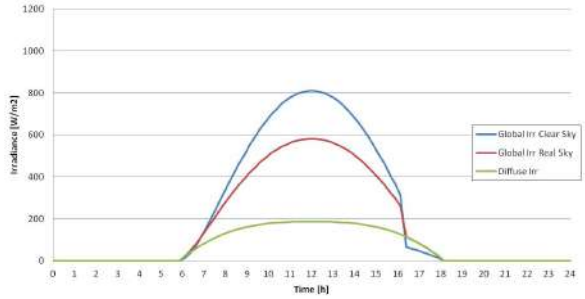

(c) March.

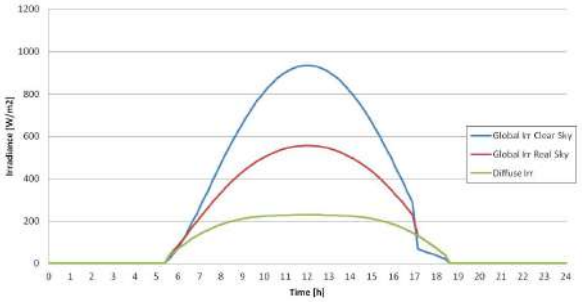

(d) April.

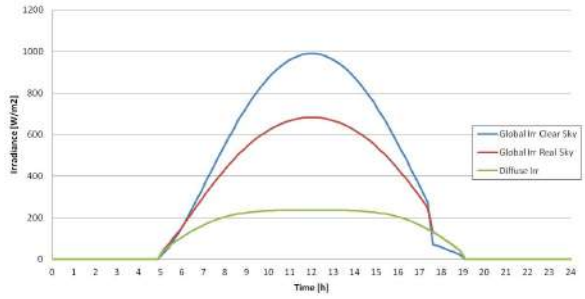

(e) May.

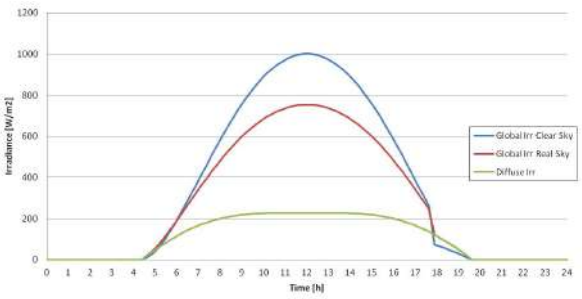

(f) June.

Figure B.1: Daily irradiation distribution: monthly averaged (Jan-June).

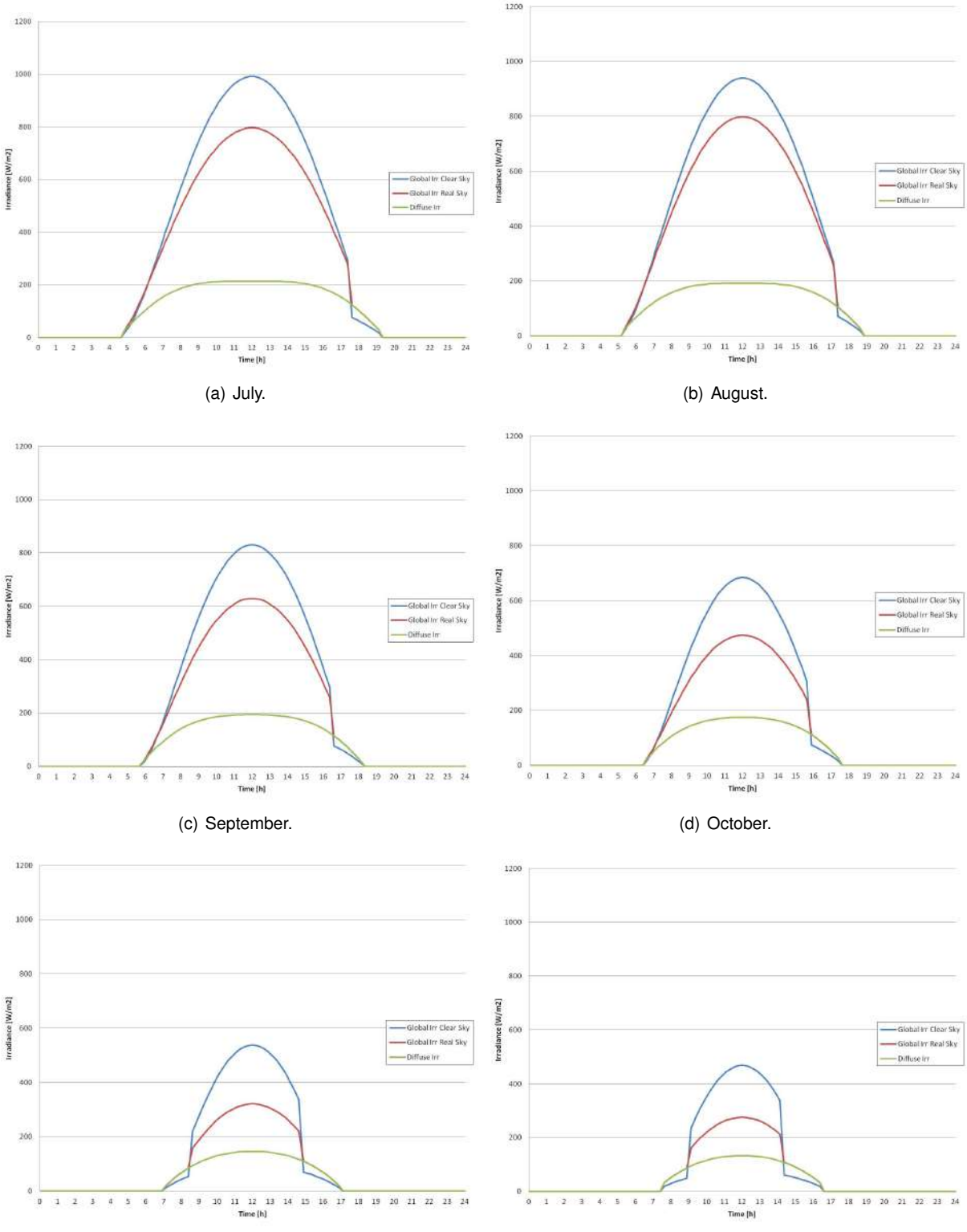

(a) July.

(b) August.

(c) September.

(d) October.

(e) November.

(f) December.

Figure B.2: Daily irradiation distribution: monthly averaged (July-Dec).

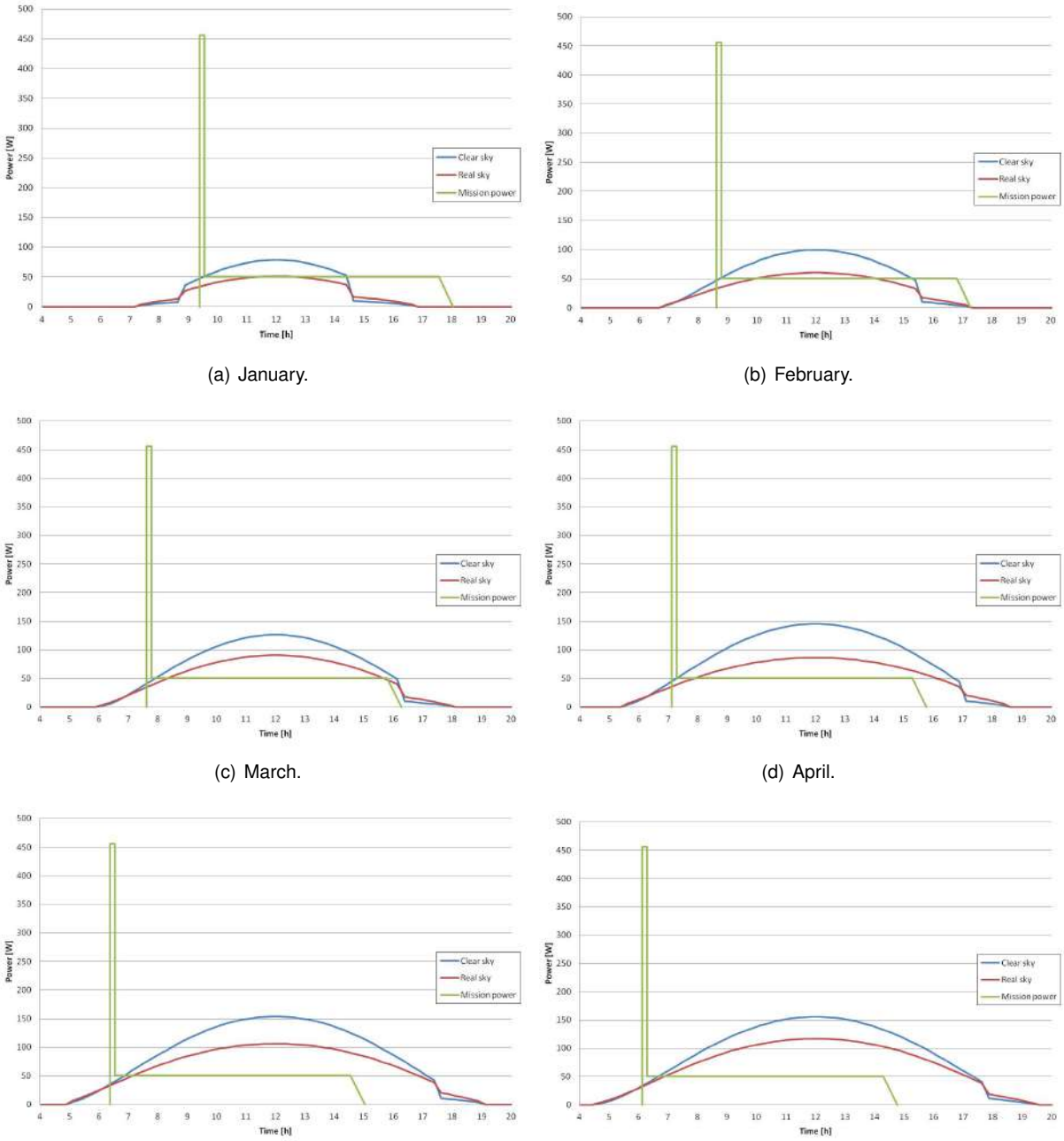

(a) January.

(b) February.

(c) March.

(d) April.

(e) May.

(f) June.

Figure B.3: Daily power distribution: monthly averaged (Jan-June).

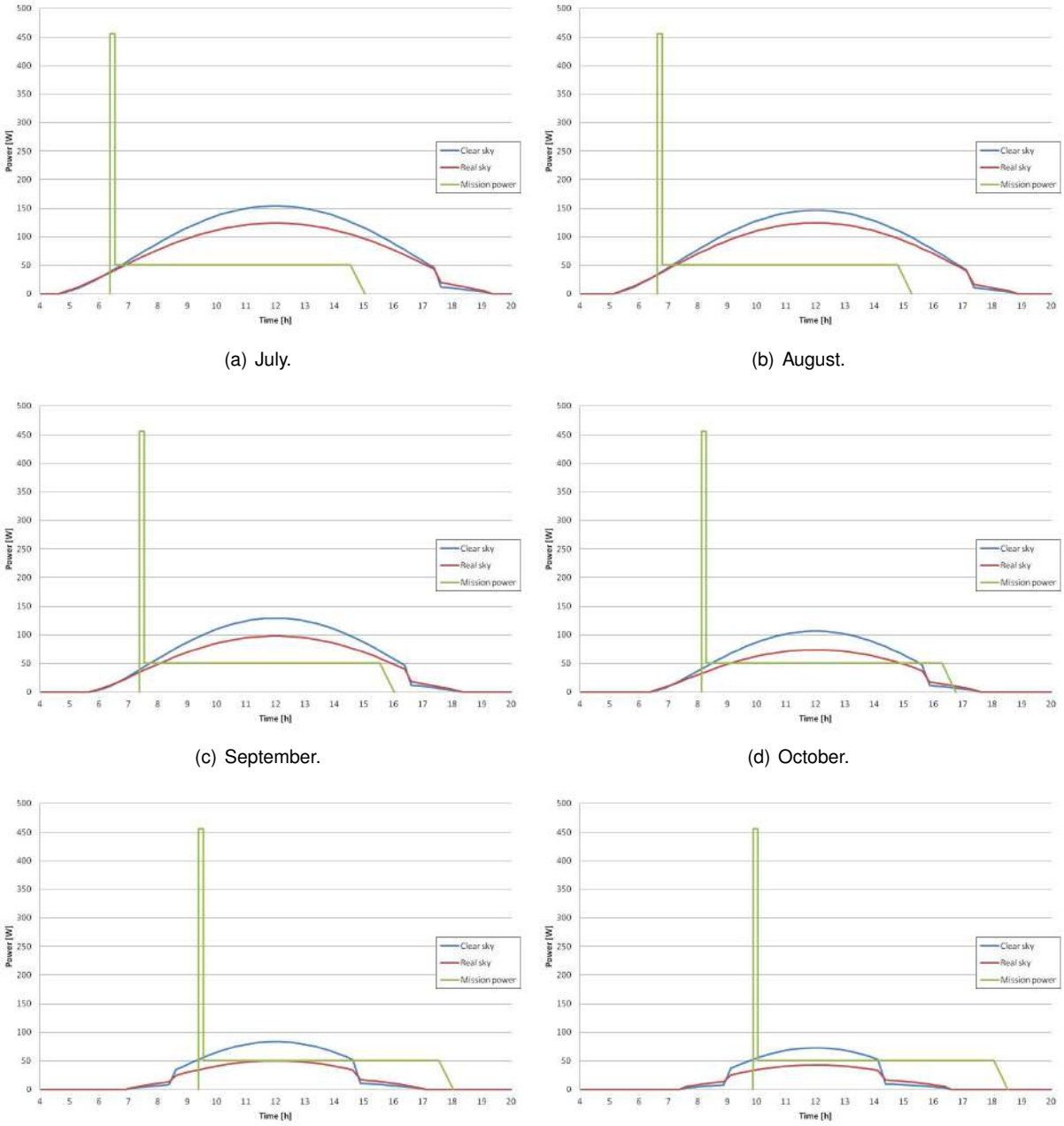

(a) July.

(b) August.

(c) September.

(d) October.

(e) November.

(f) December.

Figure B.4: Daily power distribution: monthly averaged (July-Dec).